An investigation into current challenges in solar cell technology

VU THIEN TRANG

Degree Thesis
Materials Processing Technology
2021

DEGREE THESIS	
Arcada	
Degree Programme:	Materials Processing Technology
Identification number:	18902
Author:	Vu Thien Trang
Title:	An investigation into current challenges in solar cell technology.
Supervisor (Arcada):	Stewart Makkonen-Craig
Commissioned by:	Faizan Asad

Abstract:

Photovoltaic (PV) technology has a long revolution history that today we have three different generations: crystalline silicon solar cells (mono- and multi-crystalline silicon), conventional thin-film solar cells (amorphous silicon, CdTe, CIGS), and solar cells based on exploiting novel materials (organic solar cell, dye-sensitized solar cell, perovskite solar cell, quantum dot solar cell, and multi-conjunction solar cell). Each of them has unique advantages and challenges to face that need further research for solutions. Crystalline silicon solar cells have proved their dominance in the commercial PV industry by their matured and well-established manufacturing technologies, low prices, and high efficiencies; however, they are about to meet their efficiency limit. The most essential task for them now is to continuously increase efficiency as much as possible and reduce the costs. Second-generation thin-film solar cells offer low cost of production to manufacturers as they do not use semiconductor wafer substrates and their processing equipment requires lower process temperatures. Thin-film such as amorphous solar cells needs to shift to a new configuration (e.g., tandem, multi-junction) instead of staying in a single-junction structure as there are not many opportunities for them to boost efficiency. CdTe and CIGS need to recycle in the next 10 years as they contain toxic and rare elements. Organic and dye-sensitized solar cells are well known for their environmental friendliness but poorer efficiency than other PV types. Besides how impressive and rapidly developed perovskite solar cells are, they are also raising concern about the toxicity of Pb once they are commercialized. Multi-junction solar cells have surpassed the Shockley–Queisser efficiency limit thanks to their superior performances, and they keep progressing in combining materials to achieve a new efficiency record. This thesis will go into deeper these challenges and more to find out possible solutions of them.

Keywords:	solar cells, challenges, first-generation, second-generation, third-generation, solution.
Number of pages:	113
Language:	English
Date of acceptance:	

CONTENTS

1. INTRODUCTION 11
1.1 Background of the study 11
1.2 Research aims and questions 12
1.3 Limitations 12
1.4 Materials 12
1.5 Methodology 12
2. OVERVIEWS OF SOLAR CELLS 12
2.1 The history of solar cells 12
2.2 Main types of solar cells 14
2.3 Monocrystalline and polycrystalline solar cells 17
2.3.1 Silicon – semiconductor 17
2.3.2 Silicon Manufacturing Technology 19
2.3.3 Silicon wafer 21
2.3.3.1 Czochralski silicon 22
2.3.3.2 Float-zone silicon 23
2.3.3.3 Multi-crystalline silicon 24
2.3.3.4 Ingot Wafering Process 26
2.3.4 Producing c-Si solar cell 28
2.3.5 Challenges of crystalline solar cells 30
3. Second-Generation Photovoltaics 34
3.1 Overview of thin film solar cells 34
3.2 Thin film silicon solar cell 36
3.2.1 Thin film amorphous silicon (a-Si:H) solar cell 36
3.2.2 Thin-film microcrystalline silicon solar cell 39
3.3 Cadmium Telluride (CdTe) Solar Cells 42
3.4 Copper Indium Gallium Selenide (CIGS) Solar Cells 46
4. Third-Generation Photovoltaics 50
4.1 Organic Solar Cell 50
4.2 Dye-sensitized Solar Cell 56
4.3 Perovskite Solar Cell 63
4.5 Multi-junction solar cells 69
4.6 Quantum dot solar cells 75
5. Photovoltaic solar cells and modules growth sustainability challenges 79
5.1 Materials availability 79
5.2 PV Manufacturing's Environmental Health and Safety 84

5.3 Production cost 87
5.4 PV waste treatment - recycling end-of-life PV modules 89
6. RESULTS 92
7. DISCUSSION AND CONCLUSION 98
8. REFERENCES 99

Figures

Figure 1: Change in electricity generation in 2020-2021 11
Figure 2: NREL chart of the highest confirmed conversion efficiencies for research 14
Figure 3: Global annual production percentage of PV production by technology 15
Figure 4: Classification of main types of solar cells 16
Figure 5: The theoretical efficiencies of different solar cells as a function of energy 17
Figure 6: Producing metallurgical silicon using an submerged electric arc 19
Figure 7: The Siemens technique is based on silicon's CVD. 20
Figure 8: Fluidized bed reactor 21
Figure 9: The Czochralski method for producing pure monocrystalline Si. 22
Figure 10: Schematic of Float Zone method. 24
Figure 11: The Bridgman method 25
Figure 12: The directional solidification method of mc-Si ingot growth. 25
Figure 13: Slicing up a silicon ingot into wafers 26
Figure 14: Trends for minimum as-cut wafer thickness 27
Figure 15: A monocrystalline wafer (left) and a multi-crystalline wafer (right). 28
Figure 16: World market share of different wafer types. 28
Figure 17: flowchart of producing crystalline silicon solar cells. 29
Figure 18: Crystalline silicon solar cell structures. 32
Figure 19: Thin-film panel in general compared to monocrystalline and poly-crystalline silicon panel 34
Figure 20: Thin-film photovoltaics global market share and production. 35
Figure 21: Schematic illustration of thin film solar cells 35
Figure 22: Illustrating the atomic structure of amorphous silicon with defects. 37
Figure 23: The structure of a basic single-junction (a-Si:H) solar cell 38
Figure 24: Scheme of the typical microstructure of a pencil-like conglomerates shape (μc-Si:H) layer with silicon nanocrystals embedded in (a-Si:H) tissue 39
Figure 25: Schematic of a typical a-Si:H/μc-Si:H tandem cells in the superstrate. 40
Figure 26: Measured external quantum efficiency (EQE) curves. 41
Figure 27: Schematic of a standard CdTe solar cell superstrate structure. 42
Figure 28: Schematic diagram of CdTe lab-scale vapor-transport deposition method 43
Figure 29: Comparison of measured (a) current density-voltage (JV), (b) external quantum efficiency (EQE), and (c) time-resolved photoluminescence 45
Figure 30: Schematic of a standard CIGS solar cell substrate structure. 46
Figure 31: Process schematic of CIGS deposition by co-evaporation 47
Figure 32: Efficiency (colored symbols) and $V_{OC,\,def}$ (empty symbols) as a function of ERE (calculated from V_{OC}) for CIGS. 49
Figure 33: Organic photovoltaic solar cell 50
Figure 34: Simplified energy level diagram depicting a donor-acceptor heterojunction and the OSCs working principles 52
Figure 35: Schematic illustration of a bilayer (A) and bulk heterojunction (B) OPV device architecture 53
Figure 36: A: Structures of commonly used polymer donors and fullerene acceptors. 54
Figure 37: A dye-sensitized solar cell 56
Figure 38: Schematic illustration of how a dye-sensitized solar cell works 57
Figure 39: The TiO2 film is stained with the dye solution 58
Figure 40: Different ideal type of cubic perovskite unit cell 64

Figure 41: Thin-film perovskite solar cell 66
Figure 42: Compared structures, performances, and stabilities of perovskite solar cells with FAMA (formamidinium/methylamine) and FAMA/ALD layer 67
Figure 43: SEM on Cross-Section of FAMA (pictures A-D) and FAMA/ALD (pictures E-H) to observe Iodide migration. 67
Figure 44: Best efficiencies of different types of MJSCs in 2020. 69
Figure 45: The structure of a common three-junction solar cell and solar spectrum penetration depth illustrated 70
Figure 46: The bandgap is plotted as a lattice constant function. 72
Figure 47: Illustration of the lattice mismatch at an interface of two different III-V materials. 72
Figure 48: A) The schematic structure of a wafer bonded four-junction 73
Figure 49: A) Schematic of a six-junction inverted metamorphic solar cell. 74
Figure 50: Illustration of a Molecular Beam Epitaxy system 76
Figure 51: A) UV-visible spectra curves of TiO2 film/TiO2 film filled with PbS QDs 78
Figure 52: Global PV demand-to-global supply ratio in 2030 and 2050. 84
Figure 53: The schematical two-chamber D-HVPE reactor at NREL with parallel steady-state processes for GaAs and GaInP. 88
Figure 54: Different processes to recycle c-Si PV modules 91
Figure 55: Different processes to recycle thin-film PV modules. 92

Tables

Table 1: The properties of Silicon (Petersen, 1982): 17
Table 2: Some redox mediators and dyes utilized in high performance DSCs. 59
Table 3: Material intensity estimates in 2018, 2030, 2050 for solar PV panels. 81
Table 4: Annual global solar PV material demand in 2018 in t/year (left) and relative demand of global solar PV materials in 2030 and 2050 as a ratio of current demand (right). 83
Table 5: Occupation health, public health, and environment risks of different solar cells 85

Abbreviation

ODE	1-octadecene
C_3H_7OH	2-propanol
MeCN	acetonitrile
Al	aluminum
a-Si:H	amorphous silicon
As	arsenic
SiNx	silicon nitride
ALD	atomic layer-deposited

BHJ	bulk heterojunction
CTO	cadmium stannate
CdTe	cadmium telluride
$CaTiO_3$	calcium titanium oxide
CVD	chemical vapor deposition
Cz-mono-Si	Czochralski mono-crystalline silicon
CIGS	copper indium gallium selenide
c-Si	crystalline silicon
JV	current density-voltage
CZ-Si	Czochralski silicon
CZTS	Cu_2ZnSnS_4
B_2H_6	diborane
DMSO	dimethyl sulfoxide
DMF	dimethylformamide
DNI	direct normal irradiance
D–π–A	donor pi-acceptor
D-HVPE	dynamic hydride vapor phase epitaxy
DSC	dye-sensitized solar cell
EHS	environmental health and safety risks
EVA	ethylene-vinyl acetate
EQE	external quantum efficiency
FF	fill factor
FSBR	flat scattering back reflector
FTO	fluorine-doped tin oxide
FZ-Si	float-zone silicon
FBR	fluidized bed reactor
FAMA	formamidinium/methylamine
Ga	allium
GaAs	gallium arsenide
GaInAsP	gallium indium arsenide phosphide
GaInP	gallium indium phosphide
GaP	gallium phosphide
HDS	high demand scenario
HOMO	highest occupied molecular orbital
HTL	hole transporting layer
HTM	hole transporting material
HF	hydrofluoric acid
H_2	hydrogen
HCl	hydrogen chloride
H_2Se	hydrogen selenide
In	indium
InAs	indium arsenide
GaInAs	indium gallium arsenide
InP	indium phosphide
ITO	indium tin oxide
i-TOPCon	industrial tunnel oxide passivated contacts
IBC	interdigitated back touch
IRL	intermediate reflector layer
JRC	Joint Research Centre of the European Commission
J_{sc}	short-circuit current density

Pb	lead
LEDs	light-emitting diodes
LID	light-induced degradation
LDS	low demand scenario
LUMO	lowest unoccupied molecular orbital
LPCVD	low-pressure chemical vapor deposition
MPP	maximum power point
MDS	medium demand scenario
MOCVD	metal organic chemical vapor deposition
MOVPE	metal organic vapor phase epitaxy
MG silicon	metallurgical-grade silicon
IMM	metamorphic multi-junction
MAI	methyl ammonium iodide
μc-Si	microcrystalline silicon
μc-Si:H	microcrystalline silicon
MBE	molecular beam epitaxy
Mo	molybdenum
mono-Si	mono-crystalline silicon
SiH_4	monosilane
mc-Si	multi-crystalline silicon
MJSC	multi-junction solar cell
N_2	nitrogen
NMP	N-methyl pyrrolidone
V_{OC}	open-circuit voltage
OPV	organic photovoltaics
OSC	organic solar cell
PERC	passivated emitter and rear contact
PERT	passivated emitter rear totally diffused
PH3	phosphine
P	phosphorus
P_2O_5	phosphorus pentoxide
PECVD	plasma-enhanced chemical vapor deposition
P3HT	poly(3-hexylthiophene)
PEDOT	poly-3,4-ethylenedioxythiophene
PVF	polyvinyl fluoride
PVDF	polyvinylidene fluoride
KOH	potassium hydroxide
PCE	power conversion efficiency
QDSC	quantum dot solar cell
QDs	quantum dots
RF	radio frequency
R&D	research and development
SiH_4	silane
SiO_2	silica
SHJ	silicon heterojunction
Si_3N_4	silicon nitride
$SiCl_4$	silicon tetrachloride
ss-DSC	solid-state dye-sensitized solar cell
TBP	tertiary butyl phosphine
QFLS	the splitting of quasi-fermi level

TBAs	tertiary butyl arsine
TRPL	time-resolved photoluminescence
TCO	transparent conductive oxide
$SiHCl_3$	trichlorosilane
I_3^-/I^-	triiodide/iodide
TREN·4HBr	tris(2-aminoethyl)ammonium bromide
UHV	ultrahigh vacuum
ALD	atomic layer-deposited
UAV	unmanned area vehicle
VHF-PECVD	very high-frequency plasma-enhanced chemical vapor deposition
V_{OC}	open-circuit voltage
$V_{OC,DBL}$	detailed balance limit open-circuit voltage
$V_{OC,def}$	voltage deficit
Zn-CIS	Zn-doped $CuInS_2$
GBL	γ-butyrolactone
μc-Si:F:H	fluorinated microcrystalline silicon

1. INTRODUCTION

1.1 Background of the study

The Earth – our house is in the solar system where it orbits around the Sun – the nearest star to our planet. At the center of the Sun, nuclear reactions produce 384.6 septillion watts of energy per second, which is enough to meet Earth's energy needs for centuries to come (Cain, 2015). Every second, the Sun emits an enormous amount of energy into the Solar System, but only a tiny fraction of the total radiation reaches the Earth, a large part of the solar radiation reflects the space on the surface of the clouds. However, this energy is still considered very large, at about 174 petawatts (PW) outside the Earth's atmosphere (wikipedia, n.d.). That is why, for many years, people have attempted to harness the energy of the Sun - the most plentiful source of energy available to us: clean, powerful, abundant, dependable, virtually limitless, and omnipresent everywhere. Furthermore, solar energy capture has practically no negative environmental impact, and its use does not emit harmful gases or water, pollute the environment, or cause the greenhouse effect. There are two main applications of solar energy:

- Solar heat: converting solar radiation into thermal energy, used in heating systems, or to heat water to create electric turbines.
- Solar power: converts solar radiation (in the form of light) directly into electricity (known as photovoltaics).

Solar power has proved its steady and progressive growth in recent years. Figure 1 shows that electric generation by Solar PV is at approx. 150 TW/h in the periods of 2019-20 and 2020-21, which has surpassed gas, hydro, nuclear, bioenergy, and oil energy (Laura Cozzi et al., 2021). Solar power is produced by solar cells; this thesis will focus on their technology development.

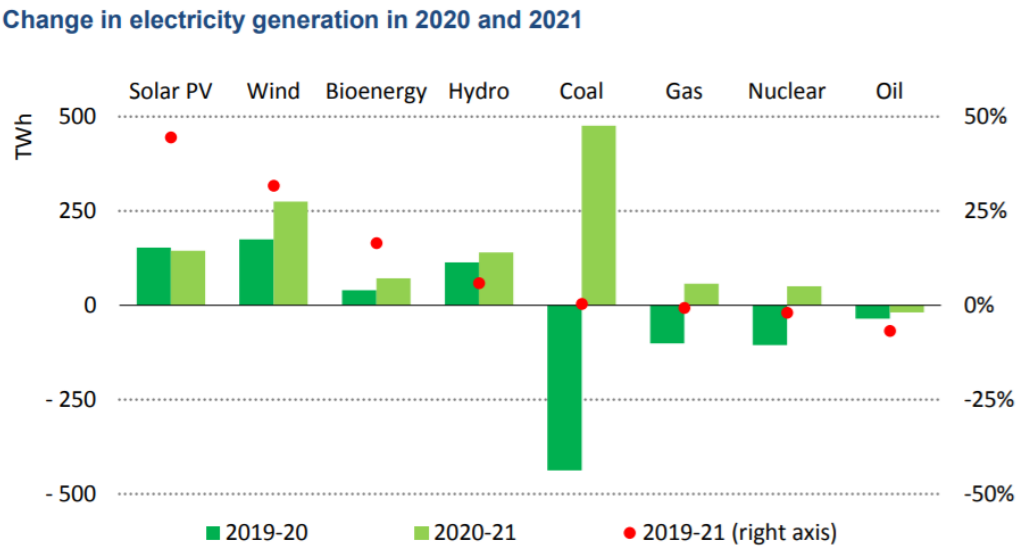

Figure 1: Change in electricity generation in 2020-2021 (Laura Cozzi et al., 2021).

1.2 Research aims and questions

This thesis aims to address the current challenges of solar cell technologies and potential solutions to improve them. In addition, the detailed solar cell characteristics, manufacturing, working principles, materials available, cost production, health and safety risks, waste treatment will be discussed for a better understanding of the thesis topic.

Therefore, the primary research questions for this thesis are:

- What/How are the solar cells in discussion?
- What are the current challenges solar cell technologies are facing?
- What are possible solutions?

1.3 Limitations

The solar cell or photovoltaic technology industry is a broad field and a promising future trend in the current scenery of exhausting fossil resources, developed countries' efforts in carbon neutrality, and increasing spacecraft application. There are endless potential techniques, novel materials under-researched to fabricate solar cell devices, attracting huge attention of researchers from all over the world to improve solar cell efficiencies, stability, and lifetimes, etc. Covering entirely the photovoltaic technologies in one thesis is unattainable, the author’s discussion of the main types of solar cells, the key challenges to overcome, noticeable methods to solve them will provide readers a panoramic view about the advancement of solar cell technology.

1.4 Materials

This thesis uses abundant materials from books, journal articles, dissertations, conferences proceeding papers, companies or organizations reports in the solar cell industry.

1.5 Methodology

The thesis uses both qualitative and quantitative research to collect, review and analyze reference materials and researched data (Streefkerk, 2019).

2. OVERVIEWS OF SOLAR CELLS

2.1 The history of solar cells

As early as human intelligence development, humanity had been using solar power in different kinds of techniques and purposes. Back to the 7th Century B.C, ancient people had used the magnifying glass to concentrate the sun's beams for setting fire and burning insects such as ants. Greek legend tells that in 2nd Century B.C, year 212,

Archimedes, a Greek scientist, utilized the reflective properties of bronze shields to aim sunlight at the Roman Empire's wooden boats to burn them down. 3rd Century B.C Romans, Greeks, and 20 A.D Chinese coincidentally used burning mirrors to light torches for religious intention. Roman people also built a kind of bathhouse that has large windows facing to the south to capture all the sun's warmth, which was popular in the first to fourth centuries A.D and the idea of living south-facing cliff dwellings had been done by the Anasazi-ancestors of Pueblo people in North America as well to survive through winter cold (Energy, n.d.).

The basic theory of photovoltaics dates at the beginning of the 18th century was the first milestone in solar technology development history. In 1839, when doing experiments with an electrolytic cell comprised of two identical metal electrodes in a weak electricity-conducting solution, Edmond Becquerel-a French physicist, saw electricity-generation increased when exposed to light, which was the photovoltaic effect. In 1873, the photoconductivity of selenium was discovered by Willoughby Smith. Continue to 1876, William Grylls Adams and Richard Evans Day discovered that selenium produces power when presented to light. Even though the experiment of using selenium solar cells to convert enough sunlight to control electrical gear failed, they demonstrated that a strong material could change light into power without heat or moving parts. Later in 1883, Charles Fritts, an American researcher, gave an official presentation of the first solar cells made from selenium wafers (Energy, n.d.).

More milestones in the historical evolution of solar technology kept continuing in the 1900s. Wilhelm Hallwachs found that the mixture of copper and cuprous oxide is photosensitive in 1904. One year later, Albert Einstein published his paper on the photoelectric effect and his theory of relativity, which led him to win the Nobel Prize in 1921. Jan Czochralski, a Polish scientist, discovered the process for making monocrystalline silicon bearing his name in 1916, when he accidentally dipped a pen in molten tin, mistaking it for ink. Czochralski immediately pulled his pen from the tin cooker and stumbled across a fine crystal metal thread hanging from the tip of the nib. The experiment was then vast, with the tip of the pen replaced with a capillary tube. Czochralski, upon re-examination, found that the metal sticking on the tube was indeed in crystalline form, which was a millimeter in diameter and up to 150 centimeters long. He published his discovery paper in 1918; indeed, at that time, Czochralski's method was only used to measure the crystallinity rate of metals such as tin, zinc, and lead[1]. It was not until 1950 that two American scientists Gordon Kidd Teal and J.B. Little of Bell Laboratories recently applied the Czochralski method to preparing monocrystalline germanium needles, a prelude to the process of using the Czochralski method in the manufacture of semiconductors. In 1932, Audobert and Stora found the photovoltaic effect in cadmium sulfide (CdS). In 1954 Photovoltaic technology was conceived in the United States when Daryl Chapin, Calvin Fuller, and Gerald Pearson built up the silicon photovoltaic (PV) cell at Bell Labs. This principle solar cell could convert enough of the sun’s energy into the capacity to run ordinary electrical gear. Bell Telephone Laboratories created a silicon solar cell with 4% to later accomplished 11% efficiency[3]. Efficient photovoltaic cells developed by Hoffman Electronics gained a lot of worldwide attention for achieving better for sequent years, 8% in 1957, 9% in 1958, 10% in 1959 when they started making solar cell commercially available, and 14% in

1960. T. Mandelkorn, U.S. Signal Corps Laboratories, fabricates n-on-p silicon photovoltaic cells (critically important for space cells; more resistant to radiation) (Energy, n.d.). Later, amorphous silicon, CdTe, CIGS (1975s), multi-junction solar cell (1980s), dye-sensitized and quantum dot cells (1990s), organic solar cells (2000s), perovskite solar cell (2010s) were introduced sequentially (N. R. E. Laboratory, 2020).

2.2 Main types of solar cells

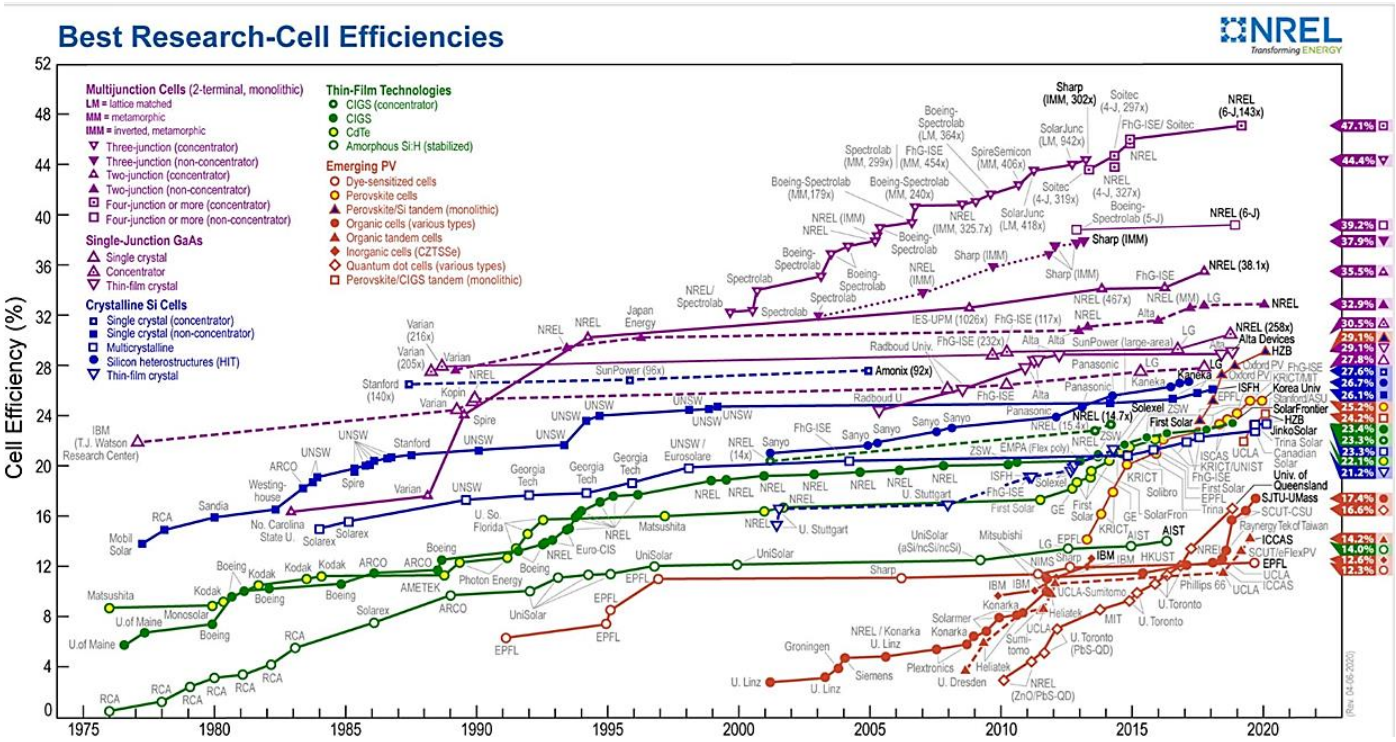

Figure 2: NREL chart of the highest confirmed conversion efficiencies for research cells for a range of photovoltaic technologies, plotted from 1976 to 2020 (N. R. E. Laboratory, 2020).

Figure 2 shows the recorded highest efficiencies of different photovoltaic technologies. Multi-junction solar cells account for the best performances (32.9% - 47.1%). Although perovskite solar cell is from the emerging PV group, its efficiency is impressive at 29.1%. Crystalline silicon solar cell recorded performance is in the range of 26.1%-27.6%. Emerging PV solar cells share the weakest efficiencies among other solar cells, but since they were just introduced in the 2000s, there are more opportunities for them to evolve.

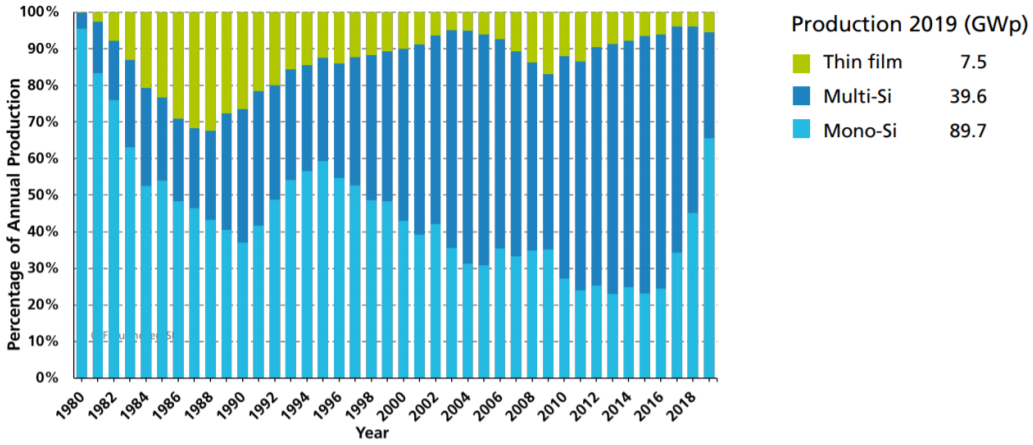

Figure 3: Global annual production percentage of PV production by technology (Simon Philipps et al., 2020).

There are three generations of solar cells in the solar technology revolution, as shown in figure 4. For quite a long time, the first-generation – crystalline silicon c-Si (mono- and multi-crystalline silicon) solar cells have been utilized to convert vitality from daylight into power. As we can see in figure 3, their technology was well established, and products made up to over 95% worldwide market share in the end of 2019, which is assumed to unchanged in 2020 and near future (Simon Philipps et al., 2020). The second generation is thin-film solar cells based on silicon (amorphous silicon a-Si:H, and microcrystalline silicon μc-Si:H), cadmium telluride (CdTe), or copper indium gallium selenide (CIGS). Their potential to be manufactured cheaper than silicon cells is promising, but their efficiencies are not high, requiring further research to improve. Finally, organic (OSC), perovskite (PSC), dye-sensitized (DSSC), multi-conjunction (MJSC), quantum dot solar (QDSC) cells are listed as the third generation to have very high efficiency and low production cost. However, each of them has different disadvantages in materials, fabrication, cost, instability, degradation, efficiency, and so on, creating many challenges for the solar industry to solve, which inspires this thesis to go into these matters.

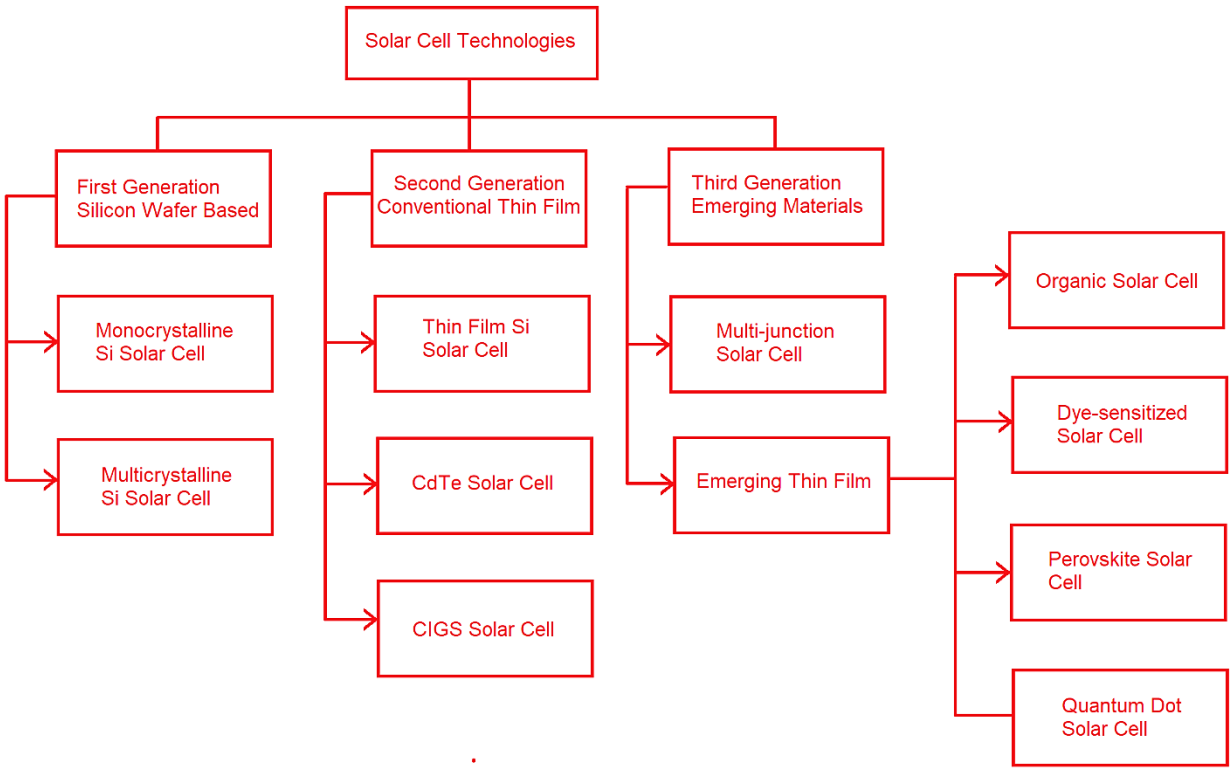

Figure 4: Classification of main types of solar cells (author's illustration).

A solar cell in its fundamental structure comprises of a semiconductor light absorber with a particular energy band gap in addition to electron-and hole-selective contacts for charge transporter partition and extraction. The photovoltaic effect occurs when photons absorbed by the semiconductor and create electron–hole (e - /h +) pairs; at a junction between n-type and p-type materials. This effect produces a potential difference or voltage across the interface. Both electrochemical and inorganic PV solar cells function in this context by creating voltage between two electrically different materials (n- and p-type) or between an n- or p-type semiconductor and a redox electrolyte. Solar energy can be harvested using organic or inorganic PV technologies, conjugated polymers, or photoelectrochemical systems based on hybrid configuration. Varying PV materials will have variable energy band gaps (figure 5) and, as a result, different light absorption capabilities (G. C. Righini et al., 2019). Figure 5 shows different materials, and they are under the Shockley–Queisser limit. Shockley–Queisser limit is a method to determine maximum theoretical efficiency of a single p-n junction solar cell by examining the quantity of electrical energy extracted per incoming photon, which was first computed by William Shockley and Hans Queisser in 1961 (W. Shockley, H. J. Queisser, 1961). The latest calculated maximum solar conversion efficiency is about 33.7%, at a band gap of 1.34 eV (Rühle, 2016).

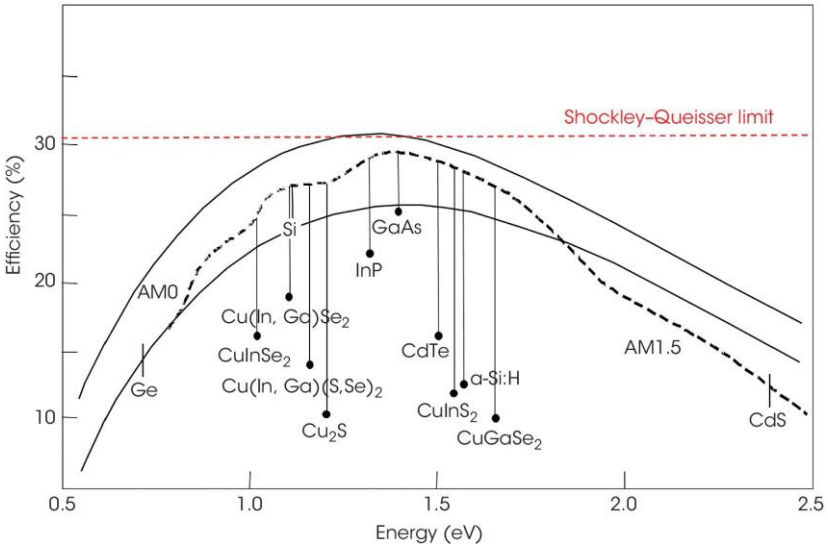

Figure 5: The theoretical efficiencies of different solar cells as a function of energy bandgap (V. M. Fthenakis et al., 2018).

2.3 Mono-crystalline and multi-crystalline solar cells

Mono-crystalline (mono-Si) and multi-crystalline (mc-Si) solar cells is the first generation of solar cells technologies. Single-junction c-Si is currently the dominant cell technology in the global PV market. In 2020, multi-crystalline silicon and mono-crystalline silicon solar cells have reached maximum efficiencies of 23.3 and 27.6%, respectively (N. R. E. Laboratory, 2020).

2.3.1 Silicon – semiconductor

No element on the Earth is more abundant than Silicon except Oxygen. Silicon can be found in rocks, sand, clay, and soils joined with either oxygen as silicon dioxide or known as silica (SiO2), or with oxygen and different components as silicates. Silicate minerals make up to more than 90% of the Earth's crust (Klein, 2020). Besides, silicon compounds also exist in water, in the environment, in numerous plants, and even in specific creatures. The properties of Silicon are shown in the box below:

Table 1: The properties of Silicon (Petersen, 1982):

Atomic number of Si	14	
Atomic mass of Si	28 (92.23%)	29 (4.67%), 30 (3.1%)
Crystal structure	Diamond	

Lattice constant	0.5431	nm
Si atoms	5×10^{22}	Atoms/cm^3
Melting point	1687	K
Specific density	2.329	g/cm^3 at 298K
Specific density (liquid)	2.57	g/cm^3
Thermal conductivity	149	W/(m K)
Coefficient of thermal expansion	2.56×10−6	m−1/K (at 298K)
Specific heat capacity	19.79	J/(mol K)
	0.705	J/(g K)
Young's modulus	150	GPa
Speed of sound	8433	m/s
Hardness	7	Mohs
Hardness	850	kg/mm^2 (Knoop hardness)
Volumetric compression coefficient	1.02×10^{-8}	kPa−1
Index of refraction (varies with temperature and λ)	~3.54~3.48	λ 1.1 μm, RTλ 2 μm, RT
Energy bandgap	1.12	eV
Intrinsic carrier concentration	1×10^{16}	m^{-3}
Relative permittivity	11.9	
Maximum electron mobility	0.143	$m^2\ V^{-1}\ s^{-1}$
Maximum hole mobility	0.047	$m^2\ V^{-1}\ s^{-1}$

In the monocrystalline silicon (mono c-Si) form, c-Si has the lattice parameters and orientation constant. Moreover, when c-Si is in the form of polycrystalline silicon (poly c-Si), it includes different sizes of monocrystalline grains divided by grain boundaries (Benda, 2018):

• Multi-crystalline silicon (mc-Si) has silicon grains of different crystallographic orientation, grain size 1 mm–10 cm.
• poly c-Si has smaller silicon grains of diverse crystallographic orientation, grain size 1 μm-1 mm.
• Microcrystalline silicon (μc-Si) has grain size < 1 μm.
• Nanocrystalline silicon is defined as a range of materials in the microcrystalline - amorphous phase transition region.

C-Si solar cells must be manufactured from multi-crystalline or mono-crystalline silicon wafer, wire-cut from ingots and cast silicon blocks. The next sections will discuss the processing technologies from planning pure silicon, silicon wafer manufacture to cell design fabrication. Here we assess the key advantages and problems associated with each and finish this section by addressing the other major challenges that impact c-Si manufacturing.

2.3.2 Silicon Manufacturing Technology

Silicon is the product of chemical reaction between silica and carbon resources like coke, coal, charcoal, or wood chips. Silicon is made in a graphite cauldron from Silica fine quality rough quartz is heated up to 2000 °C in an arc furnace (V. M. Fthenakis et al., 2018). Silicon produced in this way is called metallurgical-grade silicon (MG silicon).

$SiO2 + 2C \rightarrow Si + 2CO$

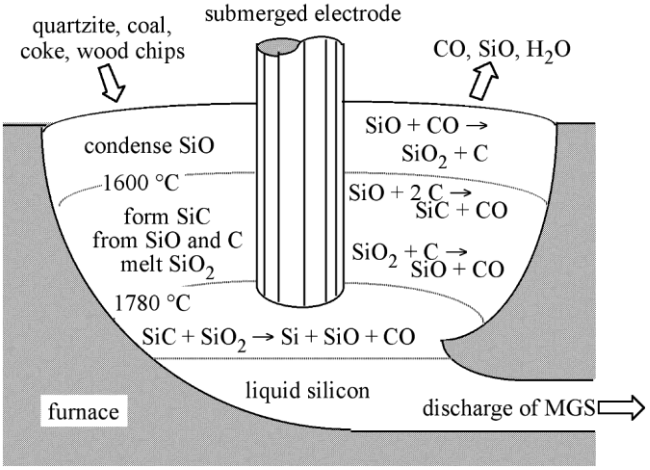

Figure 6: Producing metallurgical silicon using an submerged electric arc reduction furnace (Barron, 2014).

The fluid silicon of immaculateness of around 98% (Benda, 2018) is gathered by drawing it off at the cauldron's bottom. To transform this less pure metallurgical-grade silicon to electronic-grade polycrystalline silicon with the exceptionally purity of 99.999999%, it needs to refine all the impurities such as Cu, Ca, Al, Bo, Cr, and the others. Different kinds of processes can do this, but the two most well-known nowadays are the Siemens method (takes up to more than 90% of the products in the market research by (Bernreuter, 2020)), and fluidized bed reactor (FBR) or fluidization method (obtain 5% market share according to (Markus Fischer et al., 2021)).

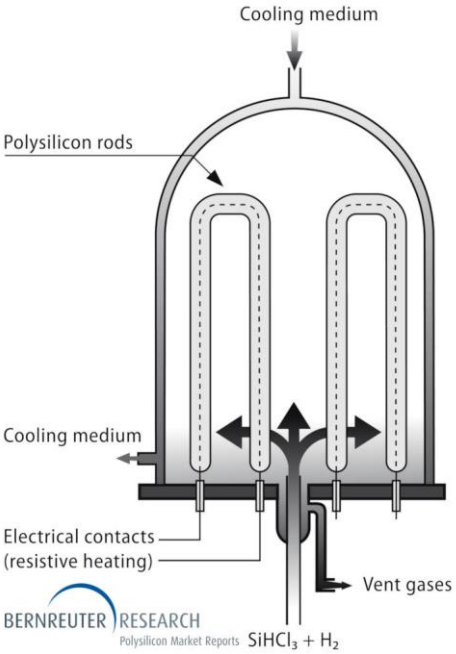

Figure 7: The Siemens technique is based on silicon's CVD - chemical vapor deposition from trichlorosilane inside a rod reactor (Bernreuter, 2020).

The Siemens method includes two stages. In the first stage, ground MG silicon is set to react with hydrogen chloride (HCl) to produce hydrogen (H_2) and trichlorosilane ($SiHCl_3$) - an intermediate and easy to evaporate liquid with a low boiling point (31.8°C). Therefore, it is not difficult to separate from other silanes and capture purified $SiHCl_3$ in distillation columns. Followed by stage two is the CVD of silicon from SiHCl3 to appear extremely pure, thin silicon fibers. Being then heated electronically at 1,150 °C in a steel reactor, these fibers start growing polysilicon bars with a diameter up to 15 - 20 cm. The remaining by-product silicon tetrachloride ($SiCl_4$) is recycled by the hydrochlorination process together with H_2 and MG silicon particles to reproduce $SiHCl_3$. This Siemens process can remove up to 0.5 - 1.5% of impurities inside MG silicon that the contamination concentrate beneath the parts per billion level satisfies the electronic-grade silicon requirements. Depending on how thorough the fraction distillation is, various degrees of polysilicon purity can be accomplished: 99.99999% (7N) - 99.999999% (8N) for multi-crystalline cells in solar grade (multi grade), 9N - 10N for monocrystalline cells in solar grade (mono grade), 10N - 11N for semiconductors in electronic grade (Bernreuter, 2020).

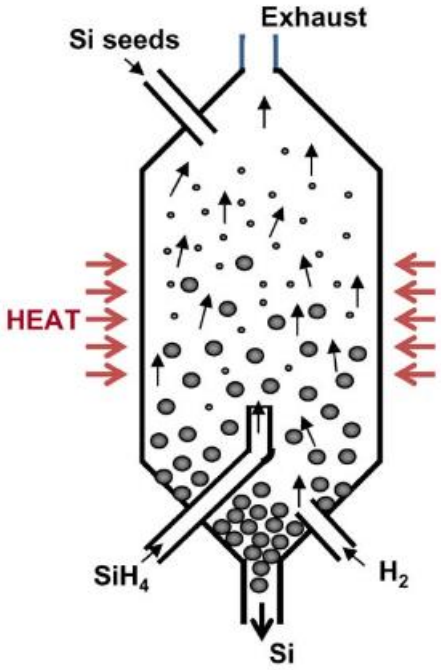

Figure 8: Fluidized bed reactor (Graham Fisher et al., 2012).

Inside a fluidized bed reactor, silicon-containing gas is infused along with hydrogen (H_2) at the bottom to shape a fluidized bed that holds small silicon seeds added from above. Usually, large FBR polysilicon plants use monosilane (SiH_4) as a feed gas as it decomposes at 650- 700°C, small facilities utilize $SiHCl_3$ with much higher decomposing temperature:
$SiH_4 \rightarrow Si + 2H_2$ (Benda, 2018)

When the exact temperature is reached, silicon deposits on the seed particles until they have developed into bigger granules that drop to the reactor's bottom (Bernreuter, 2020).

2.3.3 Silicon wafer

Silicon wafer, a thin silicone slice in crystalline form is the light absorber in c-Si solar cells. Silicon has an energy band gap of 1.12 eV which is well coordinate to the solar spectrum, close to the optimum value for solar-to-electric energy conversion utilizing a single light absorber (L. V. Mercaldo, P. D. Veneri , 2019). One disadvantage is that silicon's near band edge area (near-infrared region) has a generally low absorption coefficient caused by its indirect bandgap. Specifically, the valence band most extreme is not at the same position in momentum space as the conduction band least. Nowadays, industrial solutions such as using proper surface texture, rear mirrors, and coating antireflection have improved the light absorption even in thin wafer ∼100μm (average thickness in c-Si solar cell production lines is 180 μm[5]). Nevertheless, the indirect bandgap is also advantageous since it weakens radiative recombination, resulting in principle photogenerated electrons and holes last quite a long time. The silicon's prepotent essential recombination mechanism includes three charge transporters, one

electron recombining with a hole by moving the energy difference to a second free electron or a hole (which is afterward lost as heat) (G. C. Righini et al., 2019).

There are popular methods for the fabrication of silicon ingots in the photovoltaics industry and laboratory such as Czochralski silicon (CZ-Si), Float-zone silicon (FZ-Si), Multi-crystalline silicon (mc-Si). The following sections will discuss more details of their fundamental features.

2.3.3.1 Czochralski silicon

The most widely used method for growing mono-Si ingots for the photovoltaics (PV) industry is the Czochralski (CZ) process, thus they can be called also Czochralski monocrystalline silicon (Cz-mono-Si). In 2020, Cz-mono-Si wafer has a dominating market share of 80% and is expected to achieve 95% in the next 10 years (Markus Fischer et al., 2021). The method comprises of gradually pulling upwards, while at the same time pivoting, a situated seed out of liquid silicon contained in a pure quartz pot.

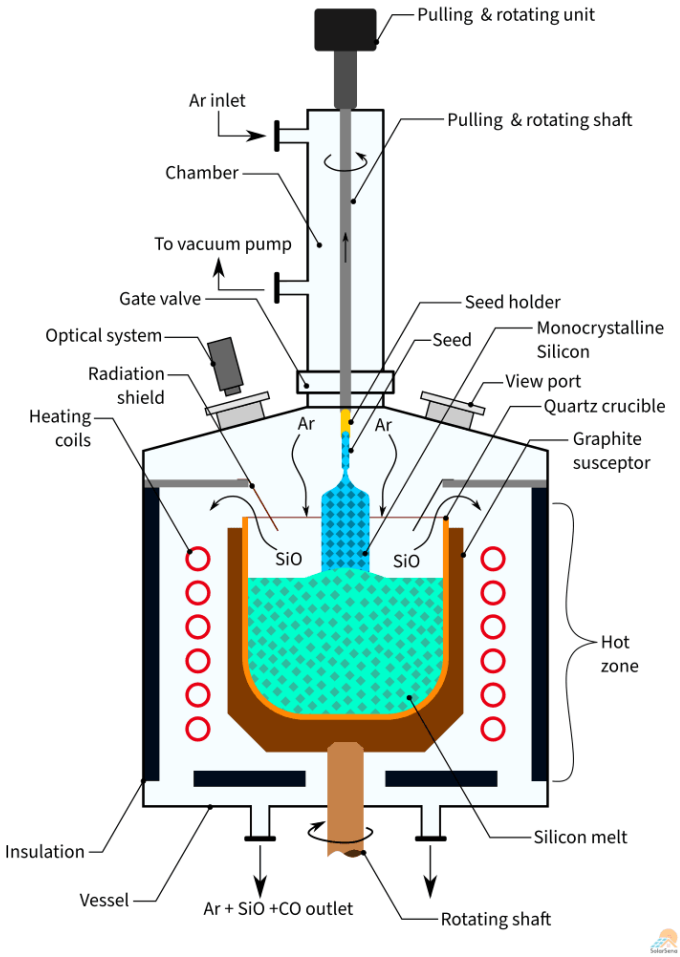

Figure 9: The Czochralski method for producing pure monocrystalline Si (Bosan, 2021).

Inside a furnace, polysilicon chunks are heap up in a graphite crucible lined with a layer of high purified quartz and heated up to 1450 ° C until they are melted down (V. M. Fthenakis et al., 2018). A specific amount of dopant known as acceptors or donors is doped with the molten fluid to prepare either p-type or n-type silicon. The doping element used p-type crystals is a boron precursor. A right amount of B_2O_3 is added to the raw silicon before melting to modify the boron concentration. Boron doping only changes a small resistivity in the whole silicon ingot since the segregation coefficient – the ratio of its concentrations in the melt and that in the crystal is 0,8. For preparing n-type crystals, doping elements can be phosphorus or arsenic. The phosphorus concentration is modified by the addition of P_2O_5 into the solid silicon with the segregation coefficient of phosphorus of 0,35, making the distribution of resistivity throughout the silicon ingot inhomogeneous (Benda, 2018).

In the next stage, a single crystal particle with a definite crystal orientation is embedded in the molten silicon. The particle is then gradually pulled up vertically onto the molten surface, whereby the liquid crystallizes on the molten surface of the seed. The tensile velocity is then raised to the specific value at which the crystal grows to the required diameter. As a result of particle rotation, the growth of crystals is cylindrical. Due to molten silicon's high reactivity, the withdraw is carried out under a stream of inert argon gas. Liquid Si reacts with the quartz crucible providing a significant amount of oxygen to the fusing process. The degree of purity increases during growth because most impurities tend to separate towards the liquid phase. The CZ method's growth rate is about 5cm / h, and the cylindrical bars are usually 1 m long, 15–30 cm in diameter (V. M. Fthenakis et al., 2018). After that, the crystal is placed to cool down before being cut off the seed end (the top) and the tapered end (the bottom) into rectangular cylinder ingots and undergone other proceedings. The cut parts can be melted again to reproduce another one. However, this method also has some challenging drawbacks. Crystal growth is sluggish and energy consuming, leading to a high cost of production. Impurities can infiltrate during the interaction between the crucible and the melt (V. M. Fthenakis et al., 2018).

2.3.3.2 Float-zone silicon

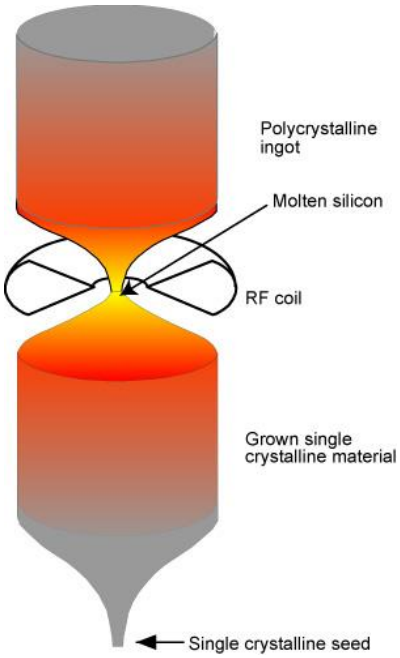

Figure 10: Schematic of Float Zone method (C. B. Honsberg, S. G. Bowden, 2019).

Float-zone silicon (FZ-Si) is another exceptionally effective option in refining impurities like carbon and oxygen to obtain mono-crystalline silicon in highly pure form but more costly. In this method, an induction coil operating, which is at radio frequency (RF), is utilized to heat the end of a polycrystalline rod and melt it. The molten part then contacts the single crystalline seeds, solidifying once more and following their orientation. The single-crystal ingot starts to grow when the polysilicon rod moves along the molten region. The impurities tend to stay in the molten region rather than be comprised into the solidified zone, thus allowing a very pure single crystal region to be left after the molten zone has passed. Recently, to make improvements in controlling micro defects and the wafers' mechanical strength, nitrogen is added during the operation purposely. The float zone technique has an advantage: the molten silicon is not in contact with other substances, such as quartz in the Czochralski method, but only in contact with the inert gas such as argon. The adding doping gasses like diborane (B2H6) and phosphine (PH3) respectively can be added to the inert gas to get p-doped and n-doped silicon. In general, the diameter of float-zone processed ingots is hard to grow larger than 15cm since surface tensions restrict the size (A. HM Smets et al., 2016).

2.3.3.3 Multi-crystalline silicon

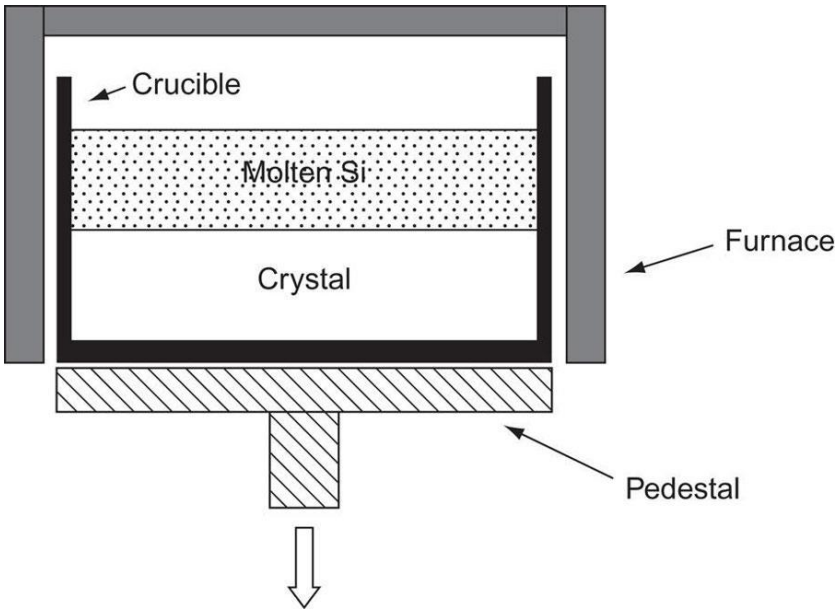

Figure 11: The Bridgman method (Ferrazza, 2017).

There are two common techniques to grow multi-crystalline silicon (mc-Si): the Bridgman and the block-casting processes. In the Bridgman method, poly c-Si is doped with B_2O_3 and melted in a rectangular shaped quartz crucible lined with anti-sticking agent silicon nitride Si_3N_4. After that, the crucible containing silicon molten is slowly taken out of the inductive heating zone, leading to crystallization. Starting from the bottom of the crucible where the temperature drops below 1410°C - silicon melting point, then the fluid-solid interphase moves a vertical upward way through the crystallization cauldron. The block-casting process consists of melting silicon feedstock in a slip-cast silica crucible with silicon nitride (Si_3N_4) coating base as same in Bridgman method, casting into molds, cooling down with strict temperature control until set into blocks (Benda, 2018).

The mc-Si block mass in 2020 can be up to 1100 kg (Markus Fischer et al., 2020). They are then cut into smaller rectangular square base ingots for wafer slicing preparation later.

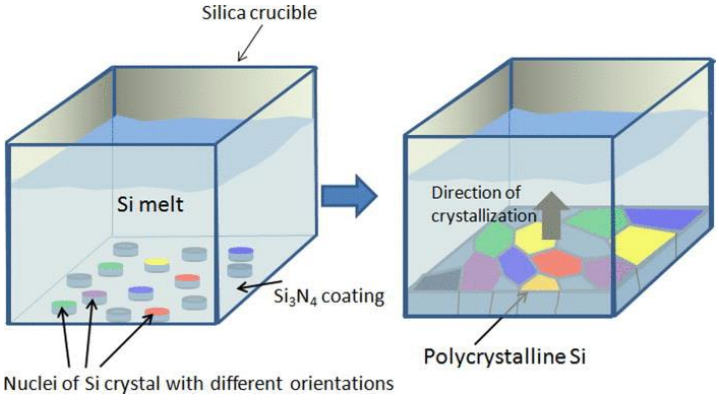

Figure 12: The directional solidification method of mc-Si ingot growth (K. Fujiwara et al., 2012).

Mc-Si block has multiple-grained structure, it can be explained as the silicon atoms' nucleation begin in many areas at the same time, resulting in a multitude of crystal grains of arbitrary crystal shape and orientation. Each grain is a few millimeters to centimeters over, and inside it has a similar structure as single-crystalline silicon. Although mc-Si is more cost saving than mono-Si, it has some drawbacks. The most evident blemish of it is the grain boundaries. Grain boundaries make high localized recombination regions due to the extra defect energy levels introduced into the band gap, thus shorten the module material's minority carrier lifetime. Furthermore, grain boundaries decrease the performance of a solar cell by hindering carrier flows and giving shunting ways to current flow across the p-n junction. Besides, mc-Si also contains brittle fracture, a higher measure of crystal imperfection and impurities, micro defects, and the possibility of cross-contamination for the crucible. Because of these reasons, mc-Si normal has lower electronic quality than the product made by the CZ process, causing a regular efficiency loss of 1% absolute or more in mass manufacture; however, this distinction is narrowing quickly. The typical crystallization rate is 3.5 kg/h; the complete 160 kg ingot's growth cycle takes 46 h (V. M. Fthenakis et al., 2018).

2.3.3.4 Ingot Wafering Process

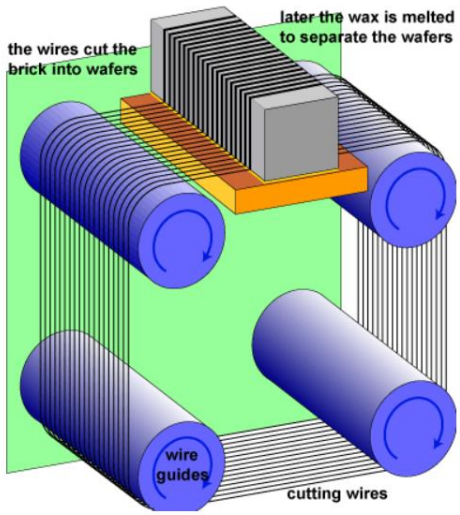

Figure 13: Slicing up a silicon ingot into wafers (C. B. Honsberg, S. G. Bowden, 2019)

Wafering is the process of slicing a cylindrical or rectangular shape monocrystalline or multi-crystalline ingot. The ingot referred to here has its end, and the bottom part cut after the crystal growth, adequate standard dimensional specifications, and passes qualify testing. The cylindrical CZ ingots are normally decreased to a quasi-square shape, leading to a loss of about 25% of the material; however, this is important if a high pressing component of the module's cells is required. The vast cast silicon

parallelepipeds are sawn into more modest blocks. Mc-Si ingots are shaped to dispose of the fringe locales that are generally intensely contaminated by the pot, accounting for around 15% of the ingot. The silicon ingot is attached to a substrate holder (generally a glass plate stuck to a steel plate). Afterward, it is pushed against the moving wire and cut into several wafers simultaneously. Cutting is accomplished by an abrasive slurry (such as silicon nitride), which is provided over the wire web and conveyed by the wire into the sawing channel suspension of hard grinding particles (such as SiC). The cutting is exceptionally moderate, commonly 8 hours. The remaining cut parts are one of the most expensive and inefficient strides of the entire silicon solar cell creation. Regardless of whether exceptionally meager wires are utilized, around 30%-40% of the silicon is squandered as observed dust, called "kerf loss" (V. M. Fthenakis et al., 2018) (Benda, 2018). However, the solar cell industry begins using diamond plated wire, providing flatter section, more environment friendly, decreasing kerf loss, and speeding the cutting process up to 3 times (Benda, 2018). The standard kerf width in diamond wire sawing currently is 65µm and predicted to drop to 50µm by 2030. The total thickness variation distance through a wafer between corresponding points on the front and back surface now is about 19µm, forecasted to decline 9µm in the next 10 years (Markus Fischer et al., 2021).

The wafer thickness required for solar cells is ≥ 100 µm, as it is a must for effective absorption of photons by an indirect semiconductor. The p-type mono-Si wafer standard thickness today is 165µm with dimension of 158.75 x 158.75mm^2(G1), p-type mc-Si is 170µm with same dimensions, all formats of n-type wafers are 160µm. Nowadays, the reduction in the wafer thickness has become a goal to achieve in the upcoming years for cost-saving and more efficient silicon use. A prediction of a quick improvement in the final cell manufacturing yield and cell performance technology in 2031 is expected to decrease the thickness to 150µm of p-type mono-Si wafers at 166.0 x 166.0mm^2 and G1, 140µm of n-type mono-Si wafers at 182 x 182mm^2 and G1 (Markus Fischer et al., 2021)(figure 14).

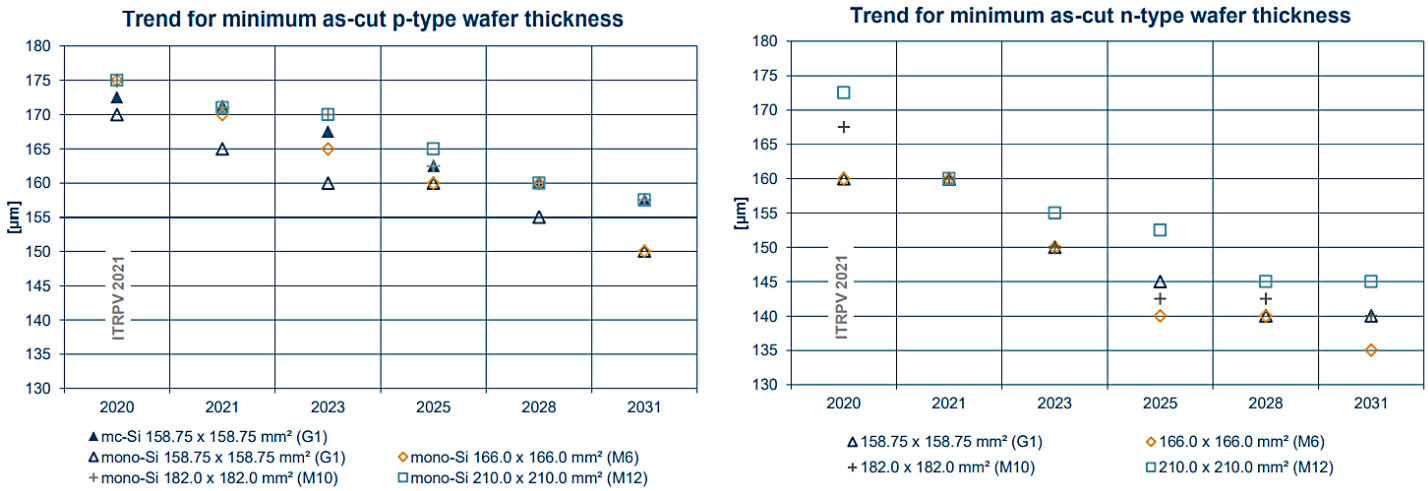

Figure 14: Trends for minimum as-cut wafer thickness (Markus Fischer et al., 2021).

To avoid vacant space between the silicon wafers, manufacturer usually trim them into square or nearly square shape instead of circular. Likewise, the sawing causes much damage to the surface, so the wafers are going under chemical etching to eliminate any

remaining slurry and reestablish the surface. Continue, the sharp, delicate edges are profiled or rounded to prevent chipping or breakage in resulting handling (figure 15). Next, every wafer is laser-marked with alphanumeric or barcode characters. This ID gives full detectability to the date, machine, and office where the wafers were made. The wafers are then stacked into an accuracy lapping machine that utilizations pressure from pivoting plates and an abrasive slurry to guarantee a more uniform synchronous expulsion of saw harm present on both front and rear surfaces and ensures the flatness uniformity (V. M. Fthenakis et al., 2018).

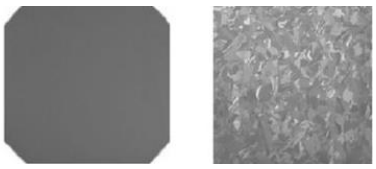

Figure 15: A monocrystalline wafer (left) and a multi-crystalline wafer (right) (Benda, 2018).

In term of listing different types of wafers, Cz-mono-Si is till dominating in the world with approximately 80% market share and predicted to rise 95% in 2031. P-type cast-mono-Si is believed to join the market around 2020 and account for 5% in 2031 (figure 16).

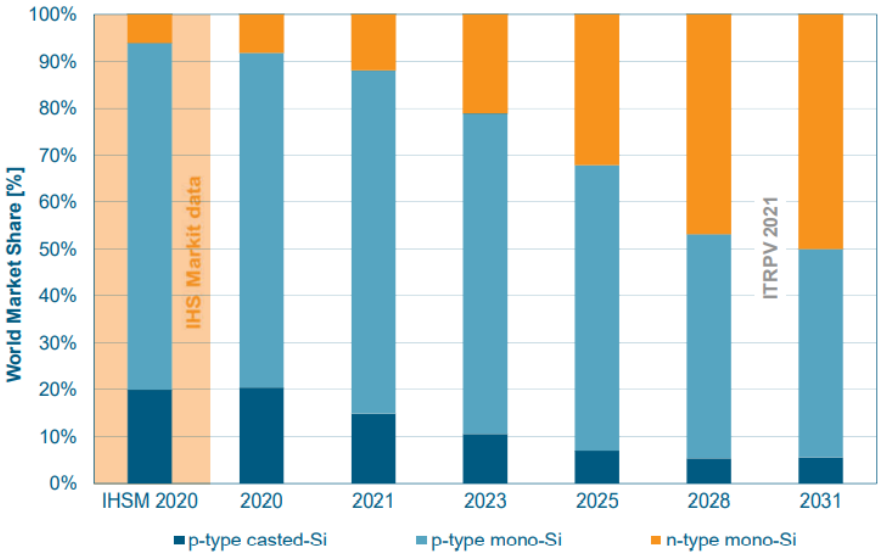

Figure 16: World market share of different wafer types (Markus Fischer et al., 2021).

2.3.4 Producing c-Si solar cell

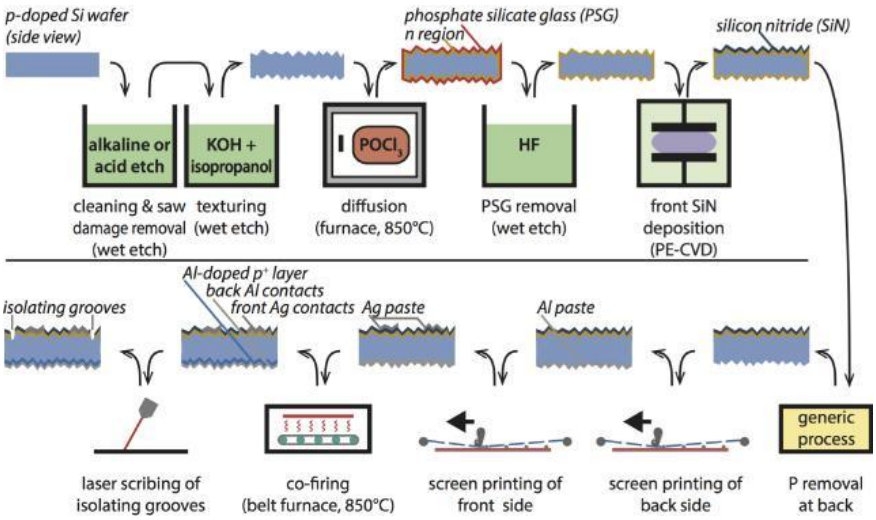

Figure 17: flowchart of producing crystalline silicon solar cells (A. HM Smets et al., 2016).

The beginning step in making a solar cell is chemical etching - the evacuation of surface damage leftover by sawing and lapping. Wafers progress down another arrangement of acidic or alkaline baths and mixture of potassium hydroxide (KOH) and 2-propanol (C3H7OH) tanks respectively with exact fluid dynamics during this corrosion cycle. These chemical solutions create a flatter, firmer wafer with a glossy completion, and increase the incident light absorption and avoid reflection losses. The wafers are then examined for mechanical parameters and process feedback (A. HM Smets et al., 2016).

After that, the emitter layer is created by a solid-state diffusion process. In this process, the wafers (up to 300 plates) are heated in a quartz tube furnace at temperature 850 °C in 50 minutes (A. Lennon, E.R. Rhett, 2017). Inside, a phosphorus-containing chemical (normally phosphoryl chloride-POCl3) is delivered by bubbling nitrogen to acts as a source for the P atoms, n-type dopant. At these high temperatures, POCl3 reacts with O2 producing phosphorus pentoxide (P2O5) that stays on the wafer surface, facilitating P atoms to mobile in the silicon crystal, diffuse into the wafer and form an n-type layer on the wafer surface (V. M. Fthenakis et al., 2018).

After the diffusion, it is necessary to clean the wafer surfaces once more to forestall the formation of a shunting pathway between the junction and the back surface not to make electron loss. Moreover, there is another byproduct made from the reaction of P2O5 and SiO2; it is phosphosilicate glass (PSG). The cleaning technique is wet etching using hydrofluoric acid (HF) (A. HM Smets et al., 2016).

Next, an anti-reflective coating and passivating layer need to be deposited, such as silicon nitride (SiNx). Varied techniques can be operated to deposition the silicon nitride layer; one of them is plasma-enhanced chemical vapor deposition (PECVD). In this process, a mixture of two different gases, silane (SiH_4) and nitrogen (N_2), is introduced in an ultrahigh vacuum (UHV) reaction chamber between parallel electrodes - a grounded electrode and an RF-energized electrode with standard frequency of 13.56 MHz. The capacitive coupling between the electrodes converted the gases into a plasma, which induces a chemical reaction and results in the silicon nitride deposited on the substrate. The substrate, placed on the grounded electrode, is typically heated at 350°C,

ensuring the wafers from damage. Afterwards, the chemical etching can be done again to remove the remaining n-doped layer in the wafer back surface (or else an n-p-n wafer is created that cannot work as a solar cell), then the p-n junction is basically completed (A. HM Smets et al., 2016).

The electric circuit or other solar cells in a PV module can be glued to the cells utilizing screen printing (SP) with a metal-based (aluminum Ag or silver Al) paste and then firing. In the front contact, Ag paste is generally imprinted on top of the anti-reflective layer. The front metal network needs cautious streamlining between resistive and shading losses. The backside is completely covered with Al. The firing process consists of placing the cell in a belt furnace with a temperature of 850 °C to make genuine contacts out of the screen printing glues. This will be co-firing if both the top and rear contacts are fired simultaneously, and the front side Ag paste carves away the SiN layer below, creating a connection direct to the emitter. Meanwhile, at the wafer backside, the Al atoms diffuse into the wafer and act as a p-type dopant; a p+ layer appears at this side. As an effect, this makes a back-surface field (BSF), which traps impurities, and intensifies the solar cell performance (A. HM Smets et al., 2016).

Finally, edge isolation is essential to keep currents from leaking at the edges of solar cells. This can be done with plasma etching, laser cutting, or masking the border. In addition, the solar cells in quantities above 36 are generally interconnected in the arrangement and encapsulated to shape a module. Commonly tempered glass can be installed in the front side, ethylene-vinyl acetate (EVA) acts as a join, and Tedlar is a back cover. These layers are overlaid by applying heat at a temperature of 150°C and pressure that is under vacuum. A neoprene gasket is sealed at the edges and an Al frame is set up for protection. The capsulated materials and processes should guarantee the module’s lifetime of 30 years. An alternation, First Solar's thin-film module applies a second glass sheet as a back cover and a sealing substance without a metal frame (A. HM Smets et al., 2016).

2.3.5 Challenges of crystalline solar cells

Multi-crystalline silicon mc-Si has held a commanding market share attributable to lower prices for a long time, mainly due to lower energy consumption and higher efficiency per crystallization devices. Material quality plays a more vital role than in the past with the improvement of cell structure factors (for ex. surface passivation) and the adaptation of new technologies. For example, when changing from a conventional Al-BSF structure to a passivated emitter and rear contact (PERC) structure for the same additional cost, the obtained performance was higher with mono-Si wafers than with mc-Si wafers. Moreover, mono-Si wafers' slicing cost is remarkably lower than that of mc-Si wafers (faster-slicing speed, less kerf loss, and more silicon wafers per kg). Fortunately, there have been currently many brilliant technical options to raise the efficiency of mono-Si, such as growing cast monocrystalline material utilizing a seed crystal to achieve better crystallographic consistency (also called quasi-mono). Exceptional efficiencies have been acquired for cast monocrystalline material opening new horizons for cast silicon. The lifetime of crystalline silicon can be expanded from 30 years to 40 years by using a glass-glass module or new encapsulating materials.

Moreover, employing bifaciality technology could contribute to the additional energy yield. Predicting module output and energy yield more precisely is an urgent task with an increasing fraction of PV in the global market. (G. M Wilson et al., 2020). Again, increasing the cell performance is crucial to diminish the need for energy-intensive materials such as crystalline silicon and module glass, thereby reducing energy payback time (A. Louwen et al., 2016). Direct energy-use avoidance, i.e., CO2 emissions, should be considered by using alternate silicon content methods, such as epitaxial wafer growth (N. Milenkovic et al., 2017). Rare or expensive materials such as silver for metal contacts or indium for transparent conductive oxide (TCO) layers in SHJ cells should be lessened or even avoided (G. M Wilson et al., 2020).

The silicon PV industry has made a continuous effort to boost performance and raise module power from 250 W to 500 W in the last ten years (G. M Wilson et al., 2020). This improvement resulted in a decline in the module cost to the PV modules system's overall cost, where land and construction costs are increasing. One of the main challenges is to continue making such progress. When manufacturers are in an increasingly competitive environment, the challenge is to make high-profile choices on the right technical pathways forward. In general, the silicon solar cells growth roadmap calls for incorporating passivating contacts in the conventional high-volume manufacturing of PV modules, then a potential transition to n-type material, and eventually the employment of tandem cells (G. M Wilson et al., 2020). Here are the discussions of the main challenges for each type of c-Si PV cell.

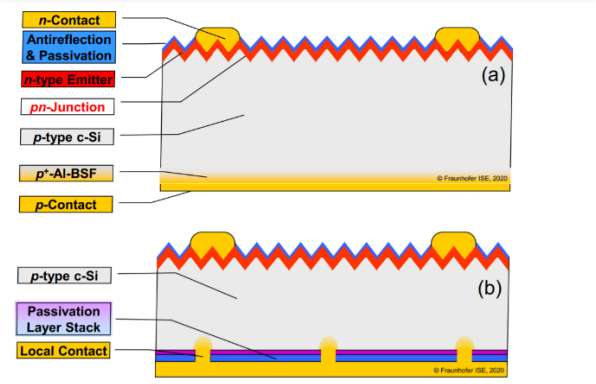

Typical crystalline silicon solar cell structures (a) Al-BSF, (b) PERC (G. M Wilson et al., 2020).

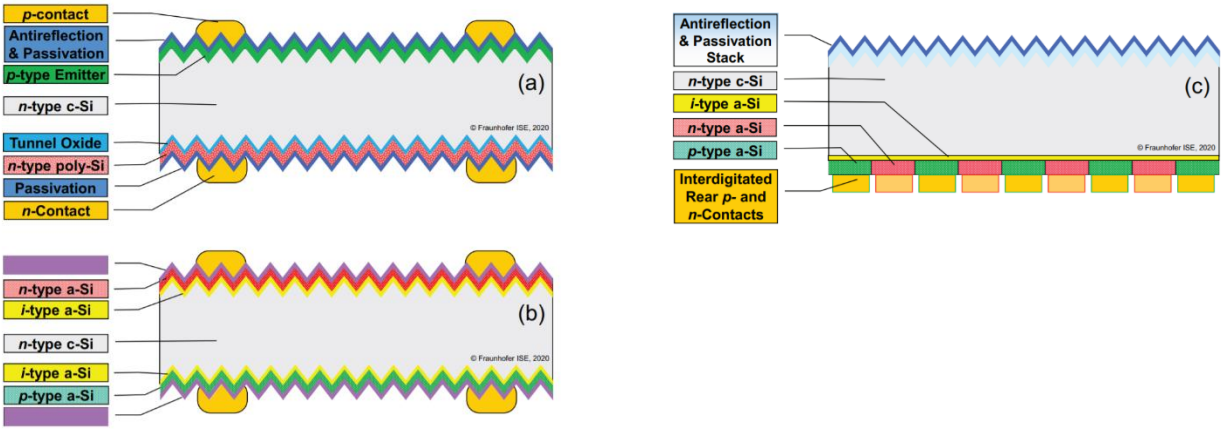

Figure 18: Crystalline silicon solar cell structures of (a) industrial tunnel oxide passivated contacts (i-TOPCon), (b) silicon heterojunction (SHJ) in the rear junction configuration, and (c) interdigitated back touch (IBC) with the heterojunction contacts (G. M Wilson et al., 2020).

The PERC cell is the 'workhorse' of the PV industry, and the critical challenge is to sustain its mainstream position by continuous enhancement of efficiency and cost lowering. In the aspect of cost savings, PERC cell fabrication is advantageous since the whole supply chain is integrated and standardized to this technology. Growing the tools throughput and automation are the key avenue for lower production costs. One of the new methods is to raise the wafer size to 210 mm, which presents tremendous difficulties in cell manufacture and module design and assembly, and likely module durability. In terms of quality enhancement, the challenges are beginning to be very complicated, as output efficiency has hit 23.3% and the functional efficiency limit of this structure is about 24.5% (G. M Wilson et al., 2020). Those challenges can be listed below:

- To achieve and sustain a high ratio of minority carrier lifetime and wafer resistivity, passing 1000 μs Ω cm^{-1}, for example, the case of current best n-type wafers, long carrier lifetime, and resistivity ratio (>2000 μs Ω cm^{-1}) have been acquired.
- To continuously minimize metal coverage by diminishing the finger diameter to less than 30μm and eliminating the busbars (no-busbar cells' calculation and sorting is a big challenge).
- To improve PERC rear contacts by reducing the voids amounts produced by silicon dissolution into the aluminum layer.
- To enhance contact tolerance for light-doped phosphorus emitters.
- To grow materials other than SiNx and Al2O3 for surface passivation and develop SHJ or tunnel oxide passivating contact technology.
- To boost bifaciality, which is the ratio between the rear and the front efficiency, without compromising front-side efficiency (G. M Wilson et al., 2020).

Bifacial modules, which were commercially launched over three decades ago, did not receive the anticipated consideration due to cost until 2018. Bifacial modules are also considered standard technology for ground-mounted systems, with a fixed tilt arrangement, a tracker, or even a North-South vertical orientation. By decreasing metal

covering on the rear side, n-doped Passivated Emitter Rear Totally diffused (PERT) or TOPCon solar cells can be 80%-95% bifacial. In contrast, PERC solar cells made from p-typed substrates usually have 65–75% bifaciality, lower than n-type due to more extensive metal coverage to form local Al-BSF and shorter carrier lifetime. The bifacial modules' additional annual energy is highly dependent on the albedo ground reflectivity, a measure of the diffuse reflection of solar radiation, and bifaciality. It ranges from 6% for PERC and 9% for TOPCon or SHJ cells to around 25% in the highest reflectivity cases (like ground with snow). Overall system structure plays a crucial role in performance (height from the ground, array-to-ground area or coverage fraction, rack design, module orientation, tracking or not). It is especially essential to prevent any module backside shading (J. S. Stein, 2019). Modeling the energy yield of bifacial PV modules is still under experimentation and improving PERC solar cells' bifaciality (G. M Wilson et al., 2020).

Interdigitated back touch (IBC) solar cells have long been considered the cell design with the most outstanding performance potential by minimizing shading losses (Swanson, 1985). Compared to a standard cell structure, the greatest challenge for this cell structure is the higher process complexity, with contacts and doping of all polarities on one side, necessitating a good pattern of at least three accurately aligned levels. Therefore, in terms of price competition, its performance should be considerably higher than that of PERC-type cells (G. M Wilson et al., 2020). By applying passivating contacts, SunPower obtained a significant improvement in performance above 25%. The new 26.7% (K. Yoshikawa et al., 2017) silicon solar cell performance record blends an IBC architecture with passivating heterojunction contacts (Figure (c)). IBC cells with polysilicon-based passivating contacts have reached outstanding efficiencies (26.1%) (F. Haase, 2018). New rear patterning process techniques, for ex. using tunnel systems, have recently been proposed to minimize process complexity (A. Tomasi, 2017).

Silicon heterojunction (SHJ) cells or heterojunction with the intrinsic thin film layer (HIT) cells use passivating contacts based on an intrinsic layer stack and doped amorphous silicon (figure (b)). Due to their outstanding surface passivation quality, recorded open-circuit voltage of 750 mV at one sun have been achieved in SHJ cells. The fill factor was significantly enhanced in recent years, thanks to a deeper comprehension of interface carrier recombination and carrier transport (J. Haschke et al., 2018). The main issue of amorphous silicon passivating contacts is that the front layer stack can absorb parasite, leading to a relatively lower short-circuit current than cells with a diffused emitter. This can be solved by employing IBC cell structures or utilizing SHJ structures as the parasite absorption of blue light in the silicon tandem cell’s bottom is no concern. The most critical technological challenge of SHJ cell structure is that after the deposition of the amorphous silicon substrate, no processes with temperatures above 200 is allowed, except fired screen-printed metal contacts, thus entailing substitute routes using plated contacts or low temperature pastes. For SHJ technology to become familiar, it is essential to address the difficulties of the expensive cost of cell processing equipment, reduce silver use or use copper as alternative by improving Cu-plating technology, and reduce indium use in the TCO layer (G. M Wilson et al., 2020).

Tunnel oxide passivated contacts (TOPCon) is a much newer substitution to SHJ for passivating contacts in industrial process. It requires the application of a thin tunneling silicon dioxide (around 1.5 nm) and a polysilicon doped layer between the rear metal contact and the silicon substrate. A phosphorus-doped polysilicon coating is employed as a rear contact structure with an n-type substrate. This structure and n-type substrates have proved their worth by laboratory efficiencies of 25.8% and 24.6% (total area) but needs to follow a well-accepted industry-standard procedure sequence for cost-cutting direction (D. Chen, 2020), (S. W. Glunz, 2018), (G. M Wilson et al., 2020).

3. Second-Generation Photovoltaics

3.1 Overview of thin film solar cells

Figure 19: Thin-film panel in general compared to monocrystalline and poly-crystalline silicon panel. A thin-film panel can be referred as having a solid black appearance. They might or may not have a frame, whether the panel does not have a frame that is a thin film panel. However, thin-film panel requires more space than monocrystalline and poly-crystalline (Solar Market, n.d.).

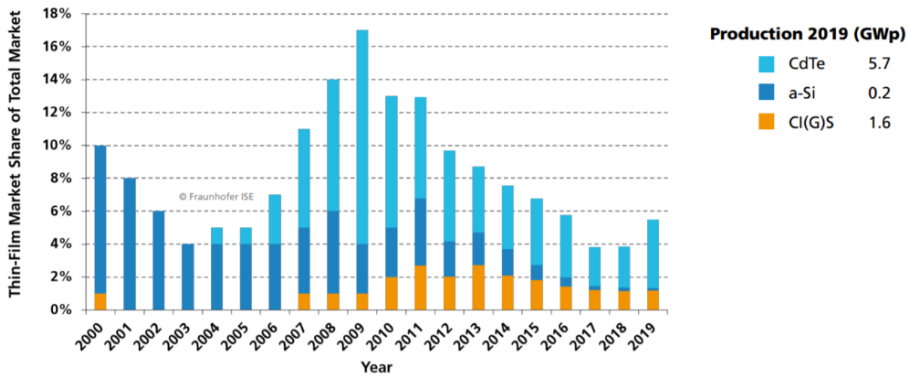

Figure 20: Thin-film photovoltaics global market share and production (Simon Philipps et al., 2020).

Thin-film photovoltaics are the world's second most popular photovoltaic (PV) technologies after crystalline silicon, and their 2019 global market share is about 5% (Simon Philipps et al., 2020). As mentioned in the introduction, conventional thin-film solar cells are commonly considered second-generation photovoltaics, and some novel thin-film materials are referred to as the third generation. Current worldwide thin-film market shares are led by CdTe with production of 5.7 GWp, followed by CiGS and a-Si with 1.6 GWp and 0.2 GWp, respectively (figure 20) (Simon Philipps et al., 2020). The rest of market shares are insignificant or just only in the laboratory scale. Their low cost of production appeals to manufacturers as they do not need semiconductor wafer substrates and their processing equipment requires lower process temperatures. Different types of thin-film PV technologies share many similar features: the ability to grown on foreign substrates (glass, flexible polymers, metal), the use of transparent conducting oxide (TCO) layer as front contact, fabrication in a “superstrate” / “substrate” configuration depended on the application (figure 21). A reflective touch material (silver, often in conjunction with a TCO interlayer for improved refractive-index matching) is used on the back surface to intensify light trapping between the absorber layers. The optical efficiency of both TCO and the reflective contact material is crucial in deciding the appropriate thickness of the absorber layers to ensure that an optimal amount of light is absorbed. In the "superstrate" configuration, the a-Si cell grows to a translucent substrate in the p-i-n series (V. Avrutin et al., 2014). On contrary, the "substrate" configuration can be developed on any substrate materials (rigid glass, flexible metal, or polymer foil). It has a reverse, n-i-p configuration, and the light enters via the last p-layer (S. Sundaram et al., 2018).

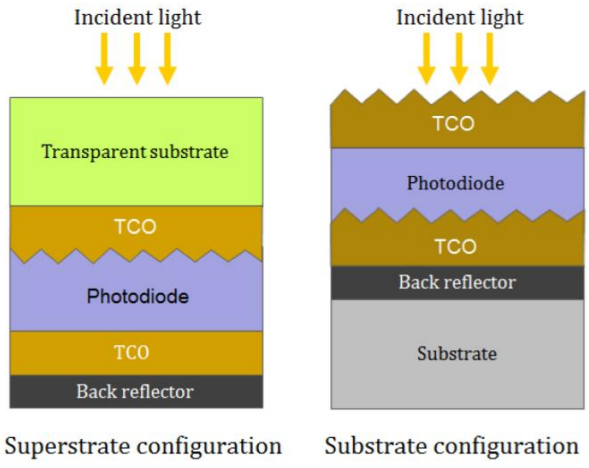

Figure 21: Schematic illustration of thin film solar cells in “superstrate” (p-i-n) configuration (in the left) and “substrate” (n-i-p) configuration (in the right) (V. Avrutin et al., 2014).

3.2 Thin film silicon solar cell

Thin-film silicon applications are based on amorphous silicon (a-Si:H) or microcrystalline (or nanocrystalline) silicon (μc-Si:H). Contrary to crystalline silicon wafers, thin-film silicon production does not need crystal traction and sawing. It also prevents kerf loss (about 100 μm/cut wafer), the factor that adds up to the cost of c-Si wafers. The thin-film technique can be described as very thin silicon layers deposited on glass or other inexpensive substrates at temperatures below the c-Si melting point. In general, thin-film silicon technology offers many advantages:

- The raw materials are abundant and non-toxic (A. Feltrin, A. Freundlich, 2008).
- Relatively simple fabrication at low temperatures with inexpensive, rigid, flexible, or lightweight substrates, for example, maximum process temperatures for general plastic substrates is only about 150 ◦ C (Jeffrey Yang et al., 2003) (V. Avrutin et al., 2014).
- Monolithic design removes the need to cut and mount individual wafers (V. M. Fthenakis et al., 2018).
- Better light absorber than crystalline silicon, super thin silicon layers can be utilized—of the order 1 μm (V. M. Fthenakis et al., 2018).
- It can also be easily patterned by laser, allowing various degrees of transparency (F. Meillaud et al., 2015).
- Its uniform appearance is suitable for building integration (Chin-Yi Tsai et al., 2014).

Though other deposition methods are also available, thin film silicon is mainly plasma-deposited from precursor gases containing Si- and H- (such as hydrogen H_2 and silane SiH_4), of which mechanism was discussed more details in the c-Si solar cells section. The most applied process is plasma-enhanced chemical vapor deposition (PECVD). Very high-frequency PECVD (VHF-PECVD) technique with higher discharge frequencies is also common. Besides, there is also a so-called “roll to roll” process including various layers being deposited on an extremely long thin sheet of stainless steel or plastic as they are fed continuously bewteen rollers (V. M. Fthenakis et al., 2018).

3.2.1 Thin film amorphous silicon (a-Si:H) solar cell

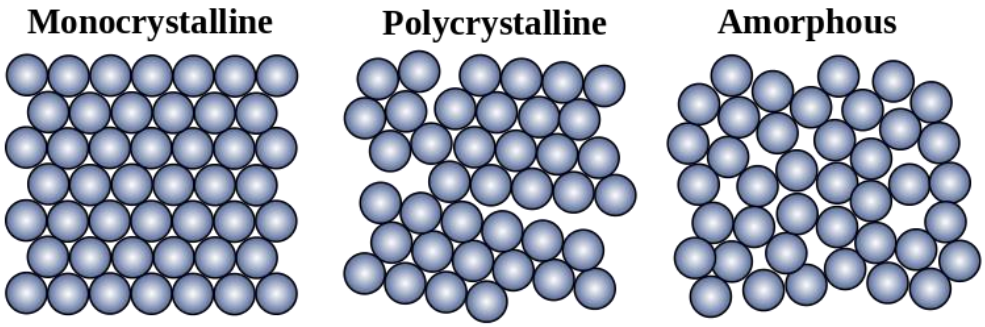

Figure 22: Illustrating the atomic structure of amorphous silicon with defects compared with monocrystalline and polycrystalline structure (Cdang et al., 2015).

The bandgap of (a-Si:H) cells is at the range of 1.6-1.8 eV can be tuned easily (Arno Smets et al., 2016). For example, alloying of amorphous Si with increasing Germanium (Ge) content allows narrower band gaps down to appx. 1.4–1.5 eV (lower values are impracticable because of the material's poor electronic quality), while band gaps above 1.7 eV are possible with the introduction of carbon or oxygen (L. V. Mercaldo, P. D. Veneri , 2019). Having such higher open-circuit voltages, but their photocurrent is restricted by the absorption of a smaller solar spectrum portion. Unlike crystalline silicon with a well-arranged diamond cubic lattice, amorphous silicon has a network of silicon atoms distributed in random distances and angles (V. M. Fthenakis et al., 2018). This structure indicates disorder on medium and long-range, which is caused by dangling bonds and bond angle distortions as illustrated in figure 22 (Pure amorphous silicon have an extremely high defect density of above 1019 cm^{-3} (Zeman, 2006)). This is the reason why hydrogen always presents and plays an essential role in passivating the dangling bonds and other defects associated with silicon atoms' random arrangement in (a-Si:H) cells. In another hand, these dangling bond defects can limit the minority carrier lifetime, hence in the doped varieties, an electric field to assist efficient collection of photogenerated carriers are essential. Moreover, due to high defect density, the charge carrier's diffusion length in hydrogenated amorphous silicon is just around 100-300nm (Arno Smets et al., 2016), also contributing to poor carrier transport. Therefore, (a-Si: H) solar cells are not based on p-n junction like c-Si SCs but the p-i-n junction structure as illustrated in figure 23: p-doped, n-doped layers, and an intrinsic layer (normally lightly n-doped) in the middle acting as a light absorber. Where there is a built-in electric field, this i-layer increases the depletion region's width and the associated electric field that sweeps minority carriers across the junction. This cell design makes the highest electrical field exist at the p-i interface so that light enters the thin, highly doped p-type layer via a transparent front contact. As a result, most charge carriers are generated near the top of the cell and retrieved successfully (V. M. Fthenakis et al., 2018).

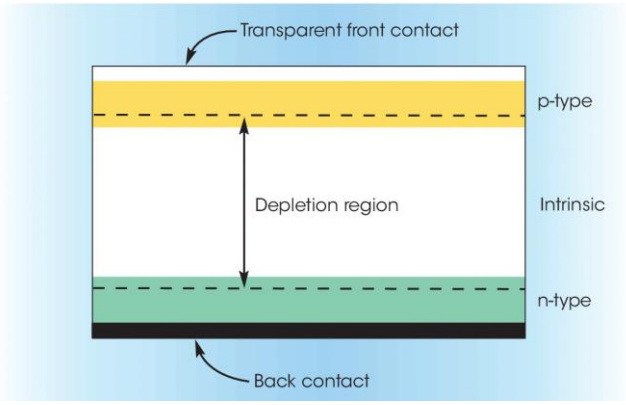

Figure 23: The structure of a basic single-junction (a-Si:H) solar cell (V. M. Fthenakis et al., 2018).

Since the structural homogeneity is found only on small volumes in (a-Si:H), strong spatial positioning of the charged particles makes its momentum mostly undetermined, and the conservation of momentum inquiry is loosened. Its commercial modules' performance under sunlight exposure suffers a significant fall of about 10-30% after six months (Nelson, 2003). This light-induced degradation (LID) effect, also called Staebler-Wronski, is the electronic degradation caused by prolonged illumination. Therefore, maintaining the original performance is still the biggest challenge that the a-Si technology is facing after two decades. One option to avoid light-induced degradation can be reducing the amorphous layer thickness. This shortens the distance traveled by photogenerated carriers until they enter the electrodes and minimize recombination losses. Nevertheless, it comes at the cost of weakening light absorption in the cell. By using optical confinement methods to exert front and back reflectors, a sufficient layer thickness and absorption could be improved (V. Avrutin et al., 2014). To date, the recorded efficiency of 14% for single-junction a-Si solar cells has been reported (N. R. E. Laboratory, 2020). In recent years, the design, material quality, processing methods, and single-junction (a-Si:H) have progressed to a mature stage where very little room is left to increase their efficiency further. The absence of a crystal structure in amorphous silicon prohibits it from matching the performance of crystalline silicon, and its commercial production has been gradually phased out (V. M. Fthenakis et al., 2018).

A more future promising approach that most manufacturers have adopted to eliminate the efficiency loss is using a two or more than two-cell stack (tandem or multi-junction structure). Amorphous silicon cells have also been combined with nanocrystalline silicon junctions (F. Meillaud et al., 2015) and the cells of other materials. The most critical advantage of this assemble is that the solar spectrum's absorption can be more effective by stacking cells with several bandgaps. This method also allows thinner layers to occupy the same or a greater number of photons, thereby preventing the efficiency degradation caused by sunlight and enhancing the cell's stability, especially in diffuse or weak sunlight. Photogenerated carriers' collection is also enhanced due to larger electric fields created by the thinner absorbing layers. The processing cost of a-Si

based tandem or multijunction SCs is higher due to many stages of depositing multilayer stacks (V. Avrutin et al., 2014). A special tandem structure of this approach is heterojunction with the intrinsic thin film layer (HIT). This hetero-structures consisting of the (a-Si:H) layer and the c-Si wafer referred to as the HIT cells (which have been discussed in the challenges of crystalline silicon section) have been developed and obtain high efficiency (S. Sundaram et al., 2018).

3.2.2 Thin-film microcrystalline silicon solar cell

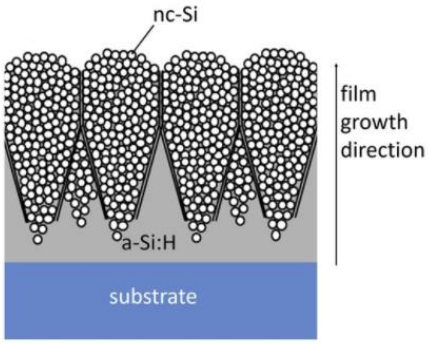

Figure 24: Scheme of the typical microstructure of a pencil-like conglomerates shape (μc-Si:H) layer with silicon nanocrystals embedded in (a-Si:H) tissue (L. V. Mercaldo, P. D. Veneri , 2019).

Microcrystalline silicon (μc-Si:H) has received lots of attention from R&D in recent years. It can be deposited in extremely thin layers of about 1μm on different substrates, consisting of glass. It is expected that microcrystalline silicon will compete with wafer manufacturing for robustness and electrical durability while at the same time limit the used amount of inexpensive and plentiful raw materials, improve performance over (a-Si:H), and reduce costs (V. Avrutin et al., 2014). (μc-Si:H) have alloys made by germanium or carbon, and compounds with nitrogen and oxygen. The crystallites size is in the range of 3–10 nm, and for this reason the material is also called nanocrystalline silicone (nc-Si:H) (L. V. Mercaldo, P. D. Veneri , 2019). The bandgap of microcrystalline silicon is about 1.12eV close to that of crystalline silicon, and easy to tune because of its crystalline network in the grains (Arno Smets et al., 2016). This bandgap can combine perfectly with (a-Si:H) higher bandgap integration into full thin-film Si tandem solar cells, figure 25 shows an example. The LID effect in (μc-Si:H) is much less severe than that in (a-Si:H), since microcrystalline silicon is a mixed-phase material composed of interconnected microcrystalline grains embedded in an amorphous matrix (F. Meillaud et al., 2015). It is not a single material, to be exact, but a class of mixed-phase materials with various microstructures, which are based on both the underlying layer or substrate and the deposition conditions.

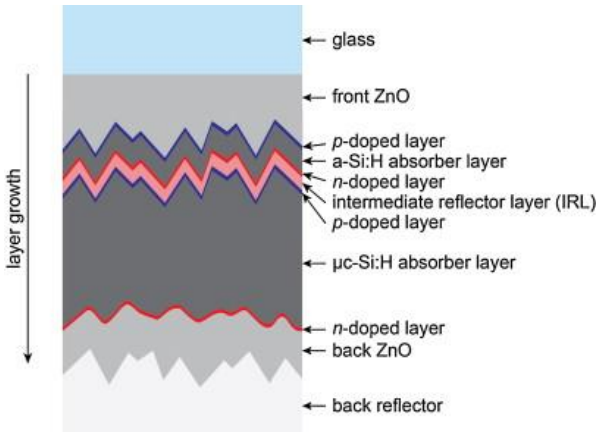

Figure 25: Schematic of a typical a-Si:H/μc-Si:H tandem cells in the superstrate configuration (F. Meillaud et al., 2015).

Like other thin-film material, (μc-Si:H) are typically plasma-deposited by PECVD techniques but with higher power density than (a-Si:H), very high hydrogen concentration, or silane high-pressured depletion regimes (HPD) at substrate temperatures of appx. 200 ̊C (V. Avrutin et al., 2014) (L. V. Mercaldo, P. D. Veneri , 2019) to faster the μc-Si:H deposition rate known to be very slow before (below 0.5 nm/s) (F. Meillaud et al., 2015). Nowadays, highly efficient (μc-Si:H) solar cells can be grown by HPD regime with a rate of more than 3 nm/s (Jason A.Peck et al., 2017), lowering the production cost. Deposition begins with an amorphous phase with a required minimum thickness. Then the localized phase transition occurs (nucleation), the crystals start growing around the seeds (L. V. Mercaldo, P. D. Veneri , 2019). Another aspect to focus on improvement is that μc-Si:H is susceptible to growth conditions, and more exactly, it relies on substrate surface chemistry and morphology (J. Bailat et al., 2002). If it is deposited on an improper surface texture, unwanted 2-D defective (nanoporous) zones would appear (Simon Hänni et al., 2013). Nanoporous zones can affect the initial electrical performance of μc-Si:H-based solar cells and their stability over time because of post-oxidation mechanisms. Even one of the best electrode materials for thin-film silicon solar cells on glass - ZnO may present an insufficient surface for (μc-Si:H) growth due to its roughness and V-shaped morphology. Therefore, to smoothen these V-shaped valleys, ZnO (usually grown by low-pressure chemical vapor deposition LPCVD) can be processed by plasma-based surface treatment of as-grown LPCVD, at the expense of reduced J_{SC} due to weaker light trapping. Furthermore, the conditions of the PECVD method and substrate temperature can can also strongly impact the development of these nanoporous zones and decrease their density (J. Bailat et al., 2006). In 2016, Louens. V. Dijk et al. developed a high-quality nc-Si:H layer on a flat superstrate called flat scattering back reflector (FSBR), comprising of an array of silica nanocylinders overcoated by silver. The FSBR not only prevents the growth silicon from defect but also avoids the associated reduction of the open-circuit voltage while the scattering intensifies the short circuit current (Lourens v. Dijk et al., 2016).
The major drawback of μc-Si is that its absorption coefficient is smaller than that of amorphous material, so that effective light absorption requires thicker layers of μc-Si

(1-2 μm) (V. Avrutin et al., 2014). It was demonstrated that RF-the excitation frequencies in PECVD process at a moderate growth rate can help the μc-Si:H material denser with rough substrates, and scatter the incoming light thus increase the solar cell efficiency. In addition, the utilization of fluorinated gas precursors for example SiF4 turning μc-Si:H to μc-Si:F:H (fluorinated microcrystalline silicon) also confirmed the extraordinarily high crystallinity and large grain size in the layers, thus increasing absorption in the near-infrared region (F. Meillaud et al., 2015). Figure 26 shows the external quantum efficiency comparison of two a-Si:H/μc-Si:H tandem cells in identical thicknesses with the SiH4/SiF4 based bottom-cell absorber layer deposited from plasma. Thanks to the use of an intermediate reflector layer (IRL) with thickness of 70nm, a J_{SC} value above 15 mA/cm^2 is achieved in the top cell, while a J_{SC} gain of 1.1 mA/cm2 obtained in the bottom cell, resulting in improved absorption in the near-infrared (F. Meillaud et al., 2015). In the best result, with a total silicon thickness thinner than 3.5μm, a total J_{SC} of 31.9 mA/cm^2 was acquired successfully in this μc-Si:F:H tandem (Simon, 2014).

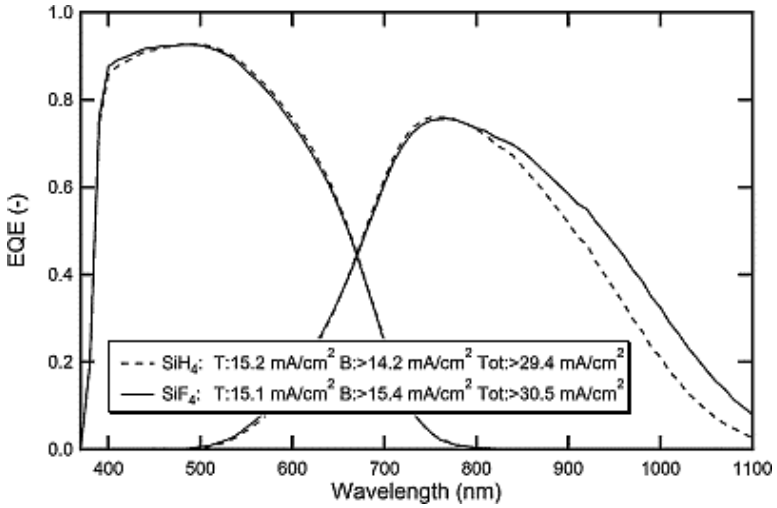

Figure 26: Measured external quantum efficiency (EQE) curves, and corresponding top (T), bottom (B), and total (T_{OT}) current densities of two a-Si:H/μc-Si:H tandem devices with top cell thickness of 250nm, IRL thickness of a 70nm, and a highly crystallized bottom cell absorber layer deposited from SiH4- or SiF4-based plasmas in 3.1μm thickness. Increased absorption in the near-infrared can be observed for the μc-Si:F:H absorber layer, making a gain of 1.1 mA/cm2. EQEs were measured at 0 V with an antireflective foil material applied to the glass (F. Meillaud et al., 2015).

3.3 Cadmium Telluride (CdTe) Solar Cells

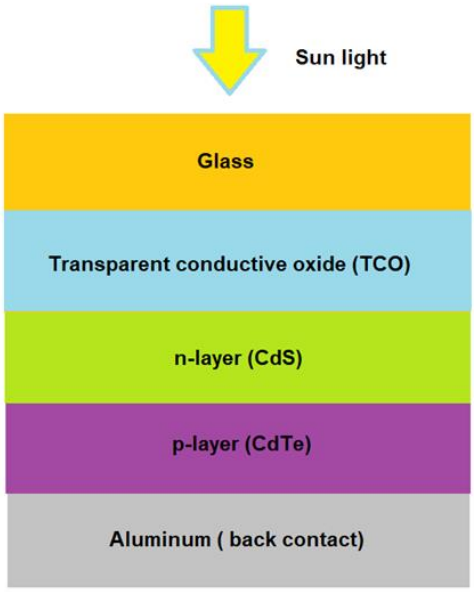

Figure 27: Schematic of a standard CdTe solar cell superstrate structure (author's illustration).

CdTe solar cells are the most productive PV among thin-film solar cell technologies (figure 2). CdTe solar cells can be fabricated faster because of fewer processing stages, and more cost-saving than standard silicon-based technologies. However, the deposition in thin film requires huge area uniformity for high productivity. Laboratory CdTe solar cell has been achieved a record efficiency of 22.1% by First Solar, and commercial CdTe modules can reach 19% provided by the same manufacturer (C. A. Miller et al., 2020). CdTe demand increased dramatically to almost 6 GW/year of CdTe PV modules in 2019, more than double its previous peak production capacity from 2016 and is expected to continue increasing steadily in the coming years (C. A. Miller et al., 2020). The structure of CdTe thin-film solar cell consists of a p-type CdTe absorber layer and n-type CdS based window layer, forming a p-n heterojunction having an intermixed interface region. CdTe thin-film absorbers have excellent electronic properties with good optical absorption $\sim 1 \times 10^3$ cm^{-1} (Madelung, 2004), and an ideal direct band gap energy of 1.5 eV, well matching with the solar spectrum, offering almost optimal theoretical efficiency approximately 30% limit (S. Sundaram et al., 2018). Its thickness of layers is typically between 1 to 8μm (T. Baines et al., 2018). Cells with layers thickness less than 1μm experience diminished efficiency due to insufficient optical absorption (N. R. Paudel et al., 2011) and pinhole shunting (J.D.Major et al., 2017). Layers much thicker than this also exhibit loss of performance due to the excessively thick absorber's additional resistivity, for example, Si with more than 100μm thick (T. Baines et al., 2018). Therefore, with a comparatively low thickness of 8μm, efficiency loss of CdTe is insignificant. However, the cells suffer from low carrier lifetimes at

<10ns (Ana Kanevce et al., 2014). Chemical simplicity and powerful stability are the most appealing highlights of the CdTe compound. CdTe is not only steady for applications on the ground, but it has also been proved to have superb stability under high energy-photon and electron irradiation for applications in the space, better than CIGS, Si, GaAs, and so forth (D.L.Batzner et al., 2004). Conventional CdTe-based devices use a superstrate configuration: output starts with a glass substrate as rear moisture barrier followed by sequential transparent conducting oxide (TCO) deposition, the n-type layer (CdS), the p-type CdTe absorbing layer, and finally the back contact (Te/ZnTe/Cu/C/Al) (figure 27). There is possible to have a buffer (nanometers of MgZnO, CdS or other materials) sandwiched between TCO and n-type layer (W. K. Metzger et al., 2019). Part of the success of First Solar has been attributed to their combination of these multiple stages into an in-line production process (V. M. Fthenakis et al., 2018).

Generally, CdTe thin-film deposition methods comprise close-spaced sublimation, vapor-transport deposition, physical-vapor deposition, sputter deposition, electrodeposition, metal-organic chemical-vapor deposition, spray deposition, and screen-print deposition (Office of Energy Efficiency & Renewable Energy, n.d.). One of the most common process is the vapor-transport deposition, a feeder creates a powder stream into a gas flow, which then brings the powder into the hot region. The powder vaporizes very rapidly and then is directed to a substrate in the form of a vapor flow using suitable geometries. The inert gas carries the powder into the hot zone. The heated permeable membrane produces the hot zone, and the ceramic shroud is set to regulate the vapor movement into the substrate. To vaporize the CdTe powder quicker, temperatures need to be higher than in laboratory devices. Close-space sublimation exerts diffusion as the transport mechanism, usually used laboratory sizes as figure 28, whereas very high rates (>20 μm/m) is achieved using convective vapor transport deposition in industrial scales (V. M. Fthenakis et al., 2018).

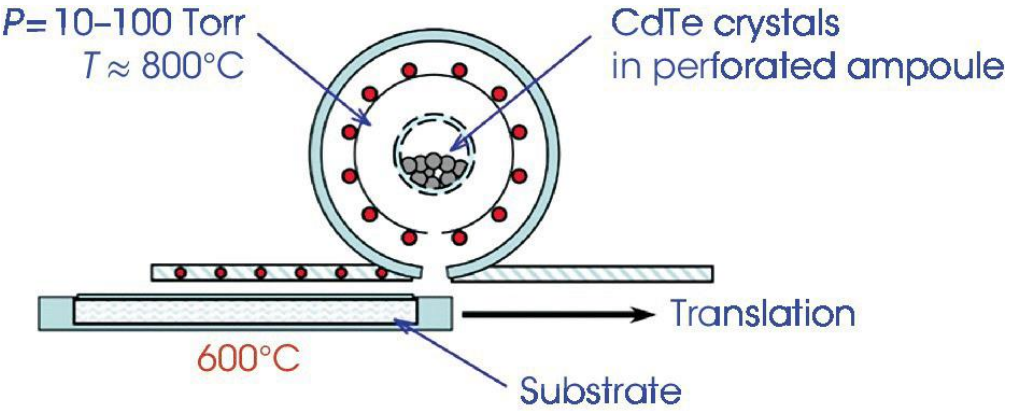

Figure 28: Schematic diagram of CdTe lab-scale vapor-transport deposition method (First Solar, 2018).

With its low fabrication costs established (below USD $0.46/watt), CdTe solar technology is scalable; its power conversion efficiency recently is 17-18.2% for commercial modules (First Solar, 2020). First Solar is projecting 7.6 GW of annual

capacity by the end of 2020, and modules are being installed worldwide for various applications. Besides, CdTe technology has moderately been used in building-integrated photovoltaics and roofing systems (G. M Wilson et al., 2020). With this expansion momentum, a continuous performance boost is desirable. Since photocurrent has reached 92% of their fundamental limit (R. M. Geisthardt, 2015) and fill factor is almost optimal for new technologies, the biggest challenge is to increase photovoltage, which includes solving the core content problems such as recombination, low carrier density and poor open-circuit voltage (G. M Wilson et al., 2020). As to be seen, the open-circuit voltage (V_{OC}) of CdTe solar cells is limited to 800–900 mV, while in GaAs with an equivalent bandgap of 1.4 eV, V_{OC} has achieved greater than 1.1 V (J. M. Burst et al., 2016).

Improving TCO and CdS layers are properly the most direct ways as they in the front contact and absorb much of the solar spectrum's blue region. In previously recorded laboratory cells, fluorine-doped tin oxide (FTO)- a typical TCO, could have been replaced by advanced materials such as Indium tin oxide (ITO) and cadmium stannate (CTO). However, it is not going to be a minor impact since ITO is costly and CTO is a complex compound (V. M. Fthenakis et al., 2018). Recently, an emerging generation of CdTe device has been developed (holding the best efficiency of 22.1% up to now), where instead of parasitically absorbing CdS, they incorporate the alloy of $CdSe_xTe_{1-x}$ (CdSeTe) in graded structure with CdTe. The $CdSe_xTe_{1-x}$ grades the absorber bandgap from appx. 1.4eV to 1.5 eV, resulting in an intensified carrier lifetime, grain boundaries passivated by Se, greater short-circuit current density, and a remarkable rise from efficiency (X. Zheng et al., 2019), e.g., figure 29. In addition, the adoption of ZnTe in the back contact can also enhances ohmic contact, hence improves performance (G. M Wilson et al., 2020). CdTe device without Se had a power conversion efficiency (PCE) of 12.5% with a relatively high Voc of 871 mV as indicated in the (JV) plot in figure 29(a). By integrating Se into the absorber, the short-circuit current density J_{SC} gains from 25.2 mA/cm^2 to 28.5 mA/cm^2, compensating for V_{OC} losses from 871 mV to 815 mV and raises performance to more than 15%. Figure 29(b) shows how CdSeTe enhances photocurrent by gathering more lights in the red spectral field. The EQE spectra from the range of 300 - 900 nm offers J_{SC} an estimate at 25.7 mA/cm^2 for CdTe and 28.6 mA/cm^2 for CdSeTe/CdTe, which is fit with the JV data. To calculate the average carrier lifetimes, TRPL with a wavelength of 640 nm of excitation was measured via glass at a repetitive laser beam (1.1 MHz rate) with unfocused excitation (0.3 mm excitation spot diameter, 1mW average power) and emission detection at 800 - 920 nm range. Fast τ_1 and slow τ_2 decay components do not dependent on wavelength detection and have been calculated by a biexponential data fit over the area of 50 – 0.5% of the optimal count. Simulations suggest that under such conditions of excitation, the space-charge field is primarily screened by photogenerated carriers. The slower TRPL decay component is the same as the life of the bulk carrier (W. K. Metzger, 2005). Data from TRPL (c) demonstrates that Se integration improved τ_1 from 0.8 ns to 1.7 ns and τ_2 from 3.2 ns to 14 ns respectively in the CdTe and CdSeTe/CdTe devices (X. Zheng et al., 2019).

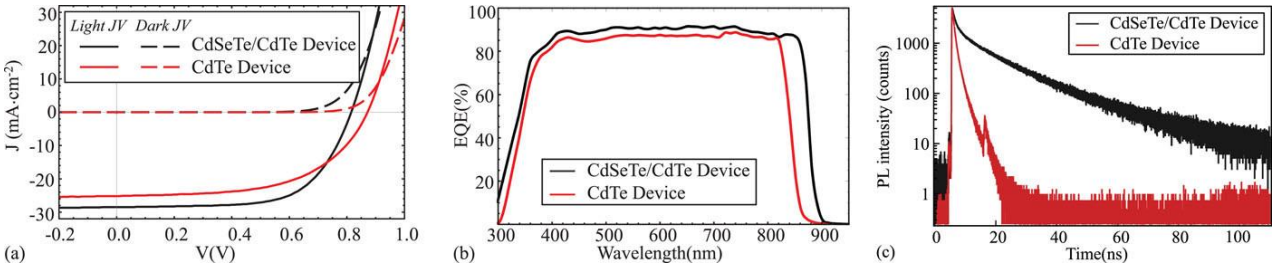

Figure 29: Comparison of measured (a) current density-voltage (JV), (b) external quantum efficiency (EQE), and (c) time-resolved photoluminescence (TRPL) results for CdTe and graded CdSeTe/CdTe solar cells (X. Zheng et al., 2019).

For a long time, $CdCl_2$ anneal, and copper (Cu) doping were combined in quick CdTe deposition by mainstream technology. It was not until the employment of Cu as a controlled and active p-dopant in bandgap engineered CdSeTe/CdTe devices that efficiencies were obtained up to 21% (M. A. Green et al., 2014), and long-term degradation less than 0.5% yr^{-1} (G. M Wilson et al., 2020). However, at the same time, there were also undesirable effects such as highly compensated defect chemistry and limitation in the useful hole density to $10^{14}cm^{-3}$, giving little headroom for improving photovoltage, efficiency, and fill factor (W. K. Metzger et al., 2019). Moreover, Cu rapidly changes and diffuses energy states spatially, making a risk of volatility thus long-term stability that need to be controlled strictly. Therefore, researchers have attempted to remove Cu entirely from the cells and doped polycrystalline CdSeTe/CdTe films with group-V dopants such as As, gaining a rise of absorber majority-carrier density by orders of magnitude to $10^{16} – 10^{17}cm^{-3}$ without compromising the carrier lifetime, a higher photocurrent >30 mA/cm^{-2}, superior stability, lower dopant diffusivity and 20.8% efficiency (W. K. Metzger et al., 2019). Other group-V dopants (for ex. P, Sb) also achieved the same effects and made V_{OC} exceeding 1 V not only in polycrystalline CdTe but also single-crystal CdTe. Morover, they are much more stable than Cu under light/electric bias or heat treatment. All these key factors have improved energy yield and opened pathways for CdTe to achieve 25% n performance (G. M Wilson et al., 2020).

The back contact is the final region that needs attention. It is nearly impossible to contact CdTe because it has low conductivity. Besides, back interaction was involved as a possible contributor to degradation. This problem would take significant experiments and fundamental analysis to be resolved. Advances in novel materials, two-dimensional architectures, nanolayers, or bilayer designs can increase minority carrier lifetime and passivate the front and back contacts. Study about Al_2O_3 and other materials have shown a remarkable increase in voltage, and reduction in velocity of interfacial recombination, unfortunately these materials are not suitable for low-resistance contacts (J. M. Kephart et al., 2018). Besides, the development of emerging CdTe-based bifacial and tandem configurations require compatible transparent back contacts on their own (V. M. Fthenakis et al., 2018). Coupling transparent back contact with long absorber lifetimes and better back-to-surface passivation could lead to successful bifacial/tandem CdTe solar technologies (G. M Wilson et al., 2020).

3.4 Copper Indium Gallium Selenide (CIGS) Solar Cells

CIGS is Group-I-III-VI2 chalcopyrite Cu(In, Ga, Al)(Se, S)$_2$ alloy system (G. M Wilson et al., 2020). Being one of the best absorber materials available, CIGS-a direct bandgap semiconductors offers its large absorption coefficient as high as that of the crystalline silicon solar cells which are indirect bandgap materials (J. Ramanujam et al., 2017). It has a comprehensive spectral response that it can absorb most of solar spectrum within 1mm with a thin layer of about 2-2.5 mm (A. K. Choudhary et al., 2020). The CIGS band gap can be adjusted from $CuInSe_2$ (1.1 eV) to $CuGaSe_2$ (1.68 eV) to $CuAlS_2$ (3.5 eV) by changing the In and Ga proportion (S. Sundaram et al., 2018) (A. K. Choudhary et al., 2020). The CIGS substrate configuration gives the highest efficiency due to advantageous process conditions. It allows using various substrates to deposition thin films from soda lime glass, metal foils, polyimide (PI) (plastic). In the other hand, if deposited on flexible substrates, it is essential to coordinate the coefficient of thermal expansion, with most noteworthy efficiencies acquired on titanium and stainless-steel foils. The insulating property of PI is advantageous for monolithic integration, but temperatures in the process are limited to ≤ 450°C, which restricts efficiency (V. M. Fthenakis et al., 2018).

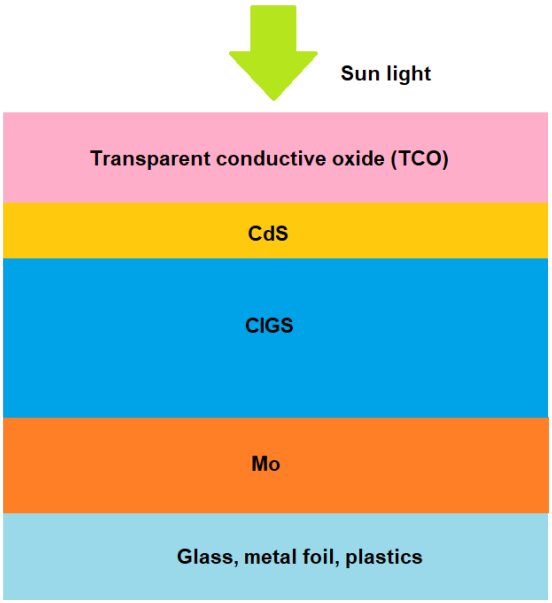

Figure 30: Schematic of a standard CIGS solar cell substrate structure (author's illustration).

The structure of heterojunction in CIGS cells is like CdTe solar cells, including a p-doped CIGS layer matched with an n-doped (CdS) window layer. The films in CIGS are deposited from the bottom up, called "substrate" as in figure 30. The process starts with molybdenum (Mo) (1.5-2 μm) deposited as a back contact followed by the CIGS p-type absorber (1–3 μm), a thin CdS buffer layer (40–80 nm), with the i-ZnO/ZnO:Al acting

as a transparent front contact (300nm) (K. H. Ong et al., 2018). This architecture is very similar among manufacturers due to its simplicity. However, each company tends to have a different technique to grow CIGS absorbers because the absorber layer's quality influences the module performance. Nowadays, commercial modules' capacity takes up to 60–70% of the champion cells' efficiency (V. M. Fthenakis et al., 2018).

Among various methods to fabricate CIGS, co-evaporation, metal selenization/sulfurization are two of the most used methods to produce recent world records and the most commercially successful CIGS solar cells (C. Huang, 2018). Metal selenization/sulfurization is a two-step technique that selenize and sulphidize the alloy of pre-deposited constituent metal films on the substrate on a predetermined stoichiometry. Frontier Solar is known for employing this method. Fundamentally, this is a two-step process in which the metals (such as In, Ga, Cu) are sputtered onto the substrate and then shifted to CIGS by annealing in a condition containing selenium and sulfur (H_2Se and H_2S or elemental Se and S gases are introduced). H_2Se and H_2S are more reactive and speed up the process but highly toxic. Co-evaporation, or co-deposition, shown in figure 31, is the most common fabrication method that produces the best efficient CIGS devices. This process alternates between copper-poor and copper-rich conditions to generate the large grains and graded Ga/In profile for high-efficient material. However, this technique entails a variety of practical challenges in in-line configuration. Evaporation sources usually distribute cosine flux, but under diffuse conditions of high vacuum, it is challenging to implement sharp differences in composition or preserve uniformity over broad regions. Furthermore, sources must be mounted in a top-down configuration to support and heat large glass substrates to 600°C, leading an increase in the production cost. Another problem with co-evaporation is that the unreactive Se supply must always be residual, causing condensation and material handling problems (V. M. Fthenakis et al., 2018).

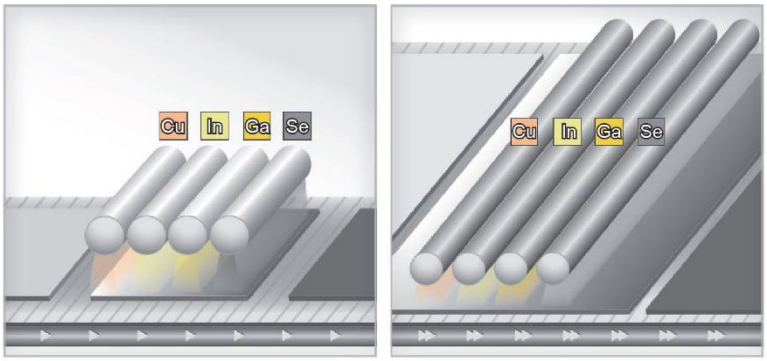

Figure 31: Process schematic of CIGS deposition by co-evaporation in in-line configuration (left) and industrial configuration (right) which coat large substrates (1 m^2), with a very fast cycle time (≤ 2 min). (M. Powalla et al., 2017).

Nowadays, CIGS cell efficiency in the laboratory has reached a record of 23,4% (N. R. E. Laboratory, 2020). Best commercial module efficiencies are 19.2% (on a small module of 0.841 m^2) (C. A. Miller et al., 2020). Since CIGS cell efficiencies in the laboratory reached a record of 21% in 2007-2009, several companies began manufacture with 10–30 MW/year capacities. However, as of 2016, only Solar Frontier, a Japanese company, started commercial production and became the world-leading

large-scale manufacturer of CIGS modules with an annual production capacity of over 1 GW (Solar Frontier, n.d.). The challenges of cost-effectively scaling both module size and production volume using the fabrication techniques above have limited CIGS. Measuring the electricity payback compared to the cost incurred per unit of power generation, CIGS industry is still attempting to minimize its cost of production to below EUR 1/Wp compared to EUR 0.75/Wp in the case of amorphous silicon solar cells. However, considering CIGS with respect to the efficient power generation which continues progressing, this is understandable price that we need to pay for a decreased power generation efficiency of a-Si (K. H. Ong et al., 2018). In another perspective, CGIS large-area device uniformity is a key challenge in closing the efficiency gap between laboratory-scale cells and commercial modules compared to that in more mature technologies but still cost-saving, in which monolithic integration may be a solution. Unlike silicon solar cell technology, where cells can be fabricated in one location and modules in another, monolithic integration enables patterning films deposited on a single insulating/insulated metal substrate with multiple cells in a sequence. Besides, improving the design of production tools and in situ metrology of control, cadmium-free buffer deposition, accelerating diffusion-limited metal selenization/sulfurization processes, and increasing the utilization of the materials of high-rate co-evaporation tools will be auxiliary to monolithic integration (G. M Wilson et al., 2020).

The theoretical performance limit for the CIGS with a bandgap of 1.14 eV is about 33.5%, which can shift up to 25% on a realistic scale by enhancing the properties of the CIGS absorber, minimizing the defect density by surface passivation, and using a reflector on the rear side to redirect the unabsorbed light (A. K. Choudhary et al., 2020). Reducing the voltage deficit $V_{OC,def}$ to the solar cell parameter detailed balance limit of AM 1.5 G is also a main challenge to improve performance (G. M Wilson et al., 2020). $V_{OC,def}$ is calculated by this equation:

$V_{OC,def} = V_{OC,DBL} - V_{OC}$ (Rühle, 2016)

$V_{OC,DBL}$ is the detailed balance limit open-circuit voltage, a function of the cell's bandgap.

Reducing $V_{OC,def}$ includes lessening non-radiative recombination rates, increasing the re-absorption of radiative recombination emissions and the splitting of quasi-fermi level (QFLS) (G. M Wilson et al., 2020). Below is the plot of compilation of CIGS efficiencies and voltage deficit by (M. Ochoa et al., 2020):

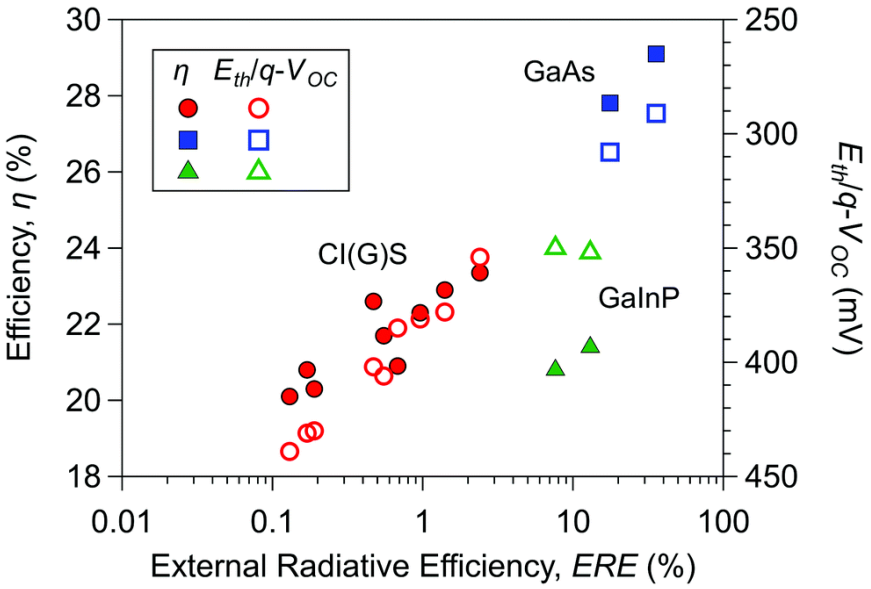

Figure 32: Efficiency (colored symbols) and $V_{OC,def}$ (empty symbols) as a function of ERE (calculated from V_{OC}) for CIGS. III–V devices with a strong photon recycling impact are also indicated for comparison. The ERE is defined as the ratio of the radiative recombination current to the dark recombination current. It is a strong merit statistic since it calculates how far VOC is from its radiative limit (Uwe Rau et al., 2017). $V_{OC,def}$ is V_{th} due to different materials' convention (M. Ochoa et al., 2020).

Figure 32 has demonstrated that performance is closely associated with ERE and $V_{OC,def}$ measured in various solar cells. The remarkable low $V_{OC,def}$ has been calculated for state-of-the-art CIGS materials with values ranging from 350-400 mV, while for the strongest GaAs and GaInP materials, these values are 300-350mV, respectively. This proves that the lower $V_{OC,def}$ is, the more efficient of the CIGS cells, even though the new CIGS structure does not have the similar advantages of recycling photons as GaInP and GaAs that uses highly reflective back touch. In terms of carrier lifetimes, effective values at 400 ns (T. Feurer et al., 2019) for CIGS have been reported and appx. 350 ns for non-radiative components (J. Werner et al., 2005). About GaAs and GaInP, the maximum reported non-radiative minority carrier lifetimes are between 1- 4 µs (n-type absorber) and 450 ns (p-type absorber), respectively (G. Lush, 2009), (R. Dagan et al., 2016). For III–V materials, the greatest change recorded due to photon recycling (at $\Delta V_{OC} \sim \Delta$ 70 mV) was obtained with n-type absorbers, appropriate with the higher measured lifetimes (M. Lumb, 2015). Although the determination of carrier lifetime in CIGS absorbers depends on several factors, the small VOC deficit and rising ERE reinforce the material's high quality (M. Ochoa et al., 2020).

Recent advancements in alkali post-deposition such as K have minimized both grain boundary recombination and sub-bandgap defects, avoiding potential fluctuations, thus decreased QFLS and increased power conversion efficiencies. However, future thermodynamic investigations are necessary to disclose the effects of metastability, kinetics, and solubility on GI K formation (Muzzillo, 2017). The best efficient CIGS now has indicated that the replacement of conventional CdS buffer layers with Cd-free $Cu(In,Ga)(Se,S)_2$ double buffer layer decreases significantly the open-circuit voltage

deficit $V_{OC,def}$ of the devices, reduceds recombination rate in the space-charge region, improves V_{OC}, short circuit current, minority carrier lifetime (M. Nakamura et al., 2019).

Many commercial CIGS devices undergo a rise in open-circuit voltage due to light-soaking metastability, causing problems with reliable and affordable testing products that are required for labeling and system scaling. Designs that predict, calculate, or remove metastability would diminish the costs associated with this ambiguity. Decreasing the recombination of the CIGS/$MoSe_2$/Mo contact by using passivated back contacts could also both activate thinner absorbers and allow reduction of bandgap gradients within the absorber, improve QFLS, and reduce costs (G. Birant et al. , 2019). Advances in manufacturing technology for the versatile integration of Group I silver alloys, which have only been successfully applied using co-evaporation, and Group VI alloys, using only metal selenization/sulfurization, can also be effective. Besides, back contact architecture can be engineered to implement light control features that improve the reabsorption of radiative recombination efflux (G. Birant et al. , 2019).

4. Third-Generation Photovoltaics

4.1 Organic Solar Cell

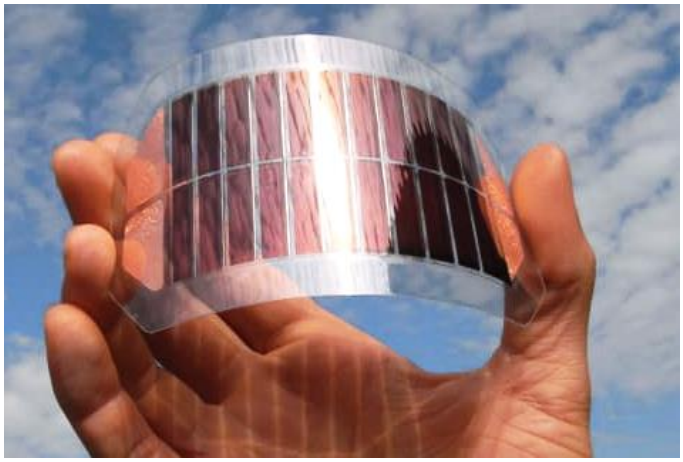

Figure 33: Organic photovoltaic solar cell (Montemayor, n.d.).

Organic solar cells (OSCs) or organic photovoltaics (OPV) or polymer solar cells are based on solution-processed semiconducting polymers which have many significant benefits: cost-saving and low temperature preparation processes, mechanical flexibility, the prospect of deposition on flexible substrates, and color adjusting. The organic semiconductor compounds are polymers or oligomers formed by carbon and hydrogen atoms, or added nitrogen, sulfur, and oxygen. Like silicon, they are typically insulators but after being doped, or photoexcited, they become semiconducting. Organic semiconductors used in superior OPVs (for example porphyrin derivatives - heme and

chlorophyll) are not harmful like other PVs' essential elements such as toxic metals (lead, cadmium), rare metals (ruthenium) (A. Babayigit et al., 2016). OPV solar cell has a semiconductor thickness smaller than 1 μm, less than 1% of the thickness used in normal inorganic PVs. Additionally, OPV cells are processed at low temperatures of 150°C, which makes them compatible with low-cost flexible plastic substrates, such as polyethylene terephthalate (Yun, 2017), and low-cost solution processes like spin coating, roll-to-roll processing, printing methods or vacuum evaporation (Taylor, 2015). The energy needed to manufacture an OSC module could record for only 5% of an mc-Si module's fabrication energy. Moreover, astonishingly less than 1g of organic semiconductor is adequate to produce one m^2 of organic solar cells, resulting in OSC having a low carbon footprint in aspects of the fabrication process and materials in use. They can return the production energy in few months after installed (M. J. Griffith et al., 2016).

In 2020, the laboratory maximum efficiency percentage of OPV solar cell is 17.4% with a surface of $1cm^2$ area (N. R. E. Laboratory, 2020). Two critical issues in producing polymer-based thin-film OSCs is weak optical absorption coefficient and low transport mobility. Techniques of using metallic nanostructures to scatter incident sunlight and plasmonic nanostructures with various shapes in the absorbing layer can improve the cell's optical absorption efficiency. The power conversion efficiency (PCE) of OSCs can be intensified by exploiting light trapping methods and anti-reflection methods (J. Ajayan et al., 2020). In 2019, I. Ghosekar et al. researched that the incorporation of a 3-hexyl thiophene buffer layer between the blended polymer and the hole transporting layer (HTL) using solution processing can remarkably improves the organic photovoltaics' PCE (I. Ghosekar, G. C. Patil, 2019).

OSC working principles.

An organic photovoltaic cell's working principles sequentially are absorption of photon, creation of exciton, exciton diffusion, charge splitting, and charge transport. OSCs use polymer as electron-donor material (such as Poly(3-hexylthiophene) or P3HT), along with fullerenes as the electron-acceptor material (such as C60PCBM). Firstly, the absorber is used in conjunction with an electron acceptor, such as fullerene, with molecular orbital energy states facilitating electron transfer. Photon absorption in OPV does not lead directly to an electron and a hole because the attraction's coulombic energy of between them is large: 0.2–1 eV (Forrest, 2005), but it initially generates an exciton, a state where the two charges are bound together. The exciton then diffuses to the interface (heterojunction) between the absorber material and the electron acceptor material. At the interface, the molecular orbitals' energetic mismatch provides sufficient driving force to dissociate the exciton and create free-charge transporter (an electron and a hole).

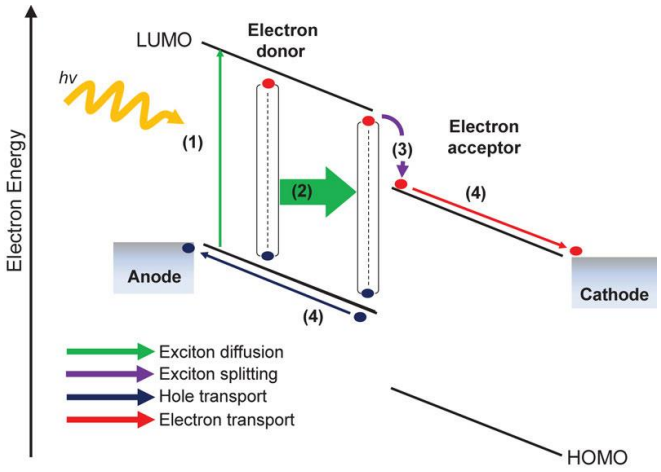

Figure 34: Simplified energy level diagram depicting a donor-acceptor heterojunction and the OSCs working principles: (1) photon absorption to form an exciton; (2) exciton diffusion to the heterojunction; (3) exciton splitting; and (4) charge transport. An exciton emerges from the excitation of an electron from the highest occupied molecular orbital (HOMO) to lowest unoccupied molecular orbital (LUMO) (Hatton, 2018).

OSC Device structures

OSCs' most common device structures are based on planar (bilayer) and bulk heterojunction (BHJ). In a bilayer OSC, the layers of donor and acceptor are deposited sequentially by vacuum deposition, spin coating from orthogonal solvents, or deposition of one layer onto the other by lamination or stamp transfer (C. D. Smith et al., 2017). The bilayer can maximize charge splitting by tuning both the donor and the acceptor properties and match the solar spectrum to allow absorption in both layers. It also offers good charge transport from the heterojunction to the contacts and allows us to examine and research device behavior. Despite those benefits, the architecture of a conventional bilayer device has some drawbacks. Because the exciton diffusion length in most organic semiconductors is restricted to under 40 nm, the donor and acceptor materials thickness on either side of the heterojunction is not thick enough to absorb all the photons at any wavelength. Excitons formed at further distances than the exciton diffusion length from the heterojunction relax to the ground state before arriving at the interface, thus would not generate photocurrent. This problem has been solved effectively by applying a bulk-heterojunction (BHJ) structure in OSCs (C. D. Smith et al., 2017). In a BHJ architecture, the donor and acceptor phases are mixed and deposited together, and unforcedly phase separate into a complex merged network in one layer. With this BHJ technique, it is possible to form the heterojunction thickness greater than 300nm (Hatton, 2018), ensuring the layer including donor and acceptor phases is twice the exciton diffusion length (A. K. K. Kyaw et al., 2013). Moreover, some studies have demonstrated that the absorbed photon for many BHJ materials can be remarkably converted 100% to excitons in the outer circuit (T. Kirchartz et al., 2012).

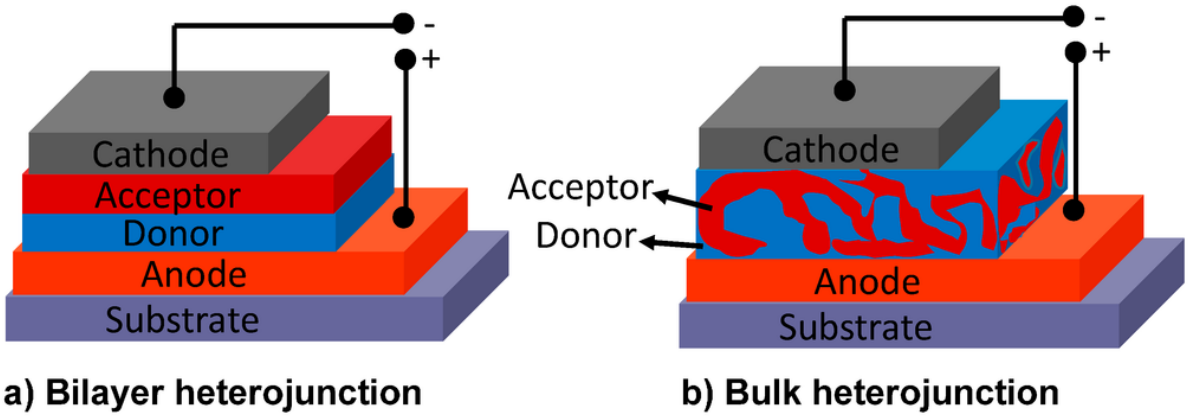

Figure 35: Schematic illustration of a bilayer (A) and bulk heterojunction (B) OPV device architecture (P. Kumaresan et al., 2014). The thickness of the organic heterojunction in a bilayer device architecture is constrained to <80 nm. The thickness of the bulk-heterojunction (BHJ) can be >300 nm (Hatton, 2018).

In the early studies, fullerene derivatives such as PC61BM ([6,6]-phenyl-C61-butyric acid methyl ester) or PC71BM has been dominate electron acceptors in ternary OSCs due to their high electron portability and isotropic charge transport. However, fullerene derivatives have some downsides, such as low absorption in the visible area, restricted tunable energy level, and weak stability. Recently, valuable non-fullerene acceptor materials with strong absorptivity in particular region and energy levels tunability have gained remarkable attention from researchers in the photovoltaic field. Device based in PBDB-TF as donor and BTP-4Cl as acceptor has achieved 16.5% efficient in 2019 (Y. Cui et al., 2019). Poly[(2,6-(4,8-bis(5-(2-ethylhexyl)thiophen-2-yl)-benzo[1,2-b:4,5-b']dithiophene))-alt-(5,5-(1',3'-di-2-thienyl-5',7'-bis(2-ethylhexyl)benzo[1',2'-c:4',5'-c']dithiophene-4,8-dione))]) as the donor and 3,9-bis(2-methylene-(3-(1,1-dicyanomethylene)-indanone))-5,5,11,11-tetrakis(4-hexylphenyl)-dithieno[2,3-d:2',3'-d']-s-indaceno[1,2-b:5,6-b']dithiophene) (ITIC) as the acceptor in an inverted PSC configuration shows an efficiency of 11.21% with good fill factor of 74% (W. Zhao et al., 2016). In 2019, the study of Wael Sayed Abdelaziz, Ahmed Shaker, M. Abouelatta-Ebrahim, Abdelhalim Zekry has shown that non-fullerene acceptor bulk heterojunction organic solar cells (NFA-BHJ-OSCs) with the structure with 3,9-bis (2-methylene-(3-(1,1-dicyanomethylene)-indanone)-5,5,11,11-tetraki(4-hexylphenyl)-dithieno[2,3-d:2′,3′-d′]-s-indaceno[1,2-b:5,6-b']dithiophene) (or ITIC) as NFA (non-fullerene acceptor) and poly[(2,6-(4,8-bis(5-(2-ethylhexyl)thiophen-2-yl)benzo[1,2-b:4,5-b′]dithiophene)-co-(1,3-di(5-thiophene-2-yl)-5,7-bis(2-ethylhexyl)benz[1,2-c:4,5-c′]dithiophene-4,8-dione)] (or PBDB-T) as the donor can obtain possible fill factor (FF) of 82.95% and efficiency of 14,25%, using device simulation (W. Abdelaziz et al., 2019).

Besides there are also all polymer, and double-cable polymer solar cells that have been investigated for their potential. All-polymer solar cells' architecture is the same as conventional PSCs. Nevertheless, they have the unique property that both donor and acceptor materials absorb light and carry the charge transport in their semiconducting structure, promising a potential and inexpensive alternation to the fullerene BHJ solar cells (A. Ramar and F. M. Wang, 2018). The recorded efficiency that all-polymer solar

cells obtaining until today is 14,4%, which uses PBDB-T: PJ1 as active layer (T. Jia et al., 2020). Double-cable polymer solar cell or single-component organic solar cells (SCOSCs) that has one double-cable conjugated polymer in the photoactive layer, has achieved record efficiency of 8.40 % recently (X. Jiang et al., 2020).

Figure 36: A: Structures of commonly used polymer donors and fullerene acceptors.

B: Non-fullerene acceptors ITIC and PMI-F-PMI structures.

C: Non-fullerene all-polymer electron acceptor structures.

D: Charm-bracelet type double-cable polymers COP2, D3, and PPV-C60 structures (A. Ramar and F. M. Wang, 2018).

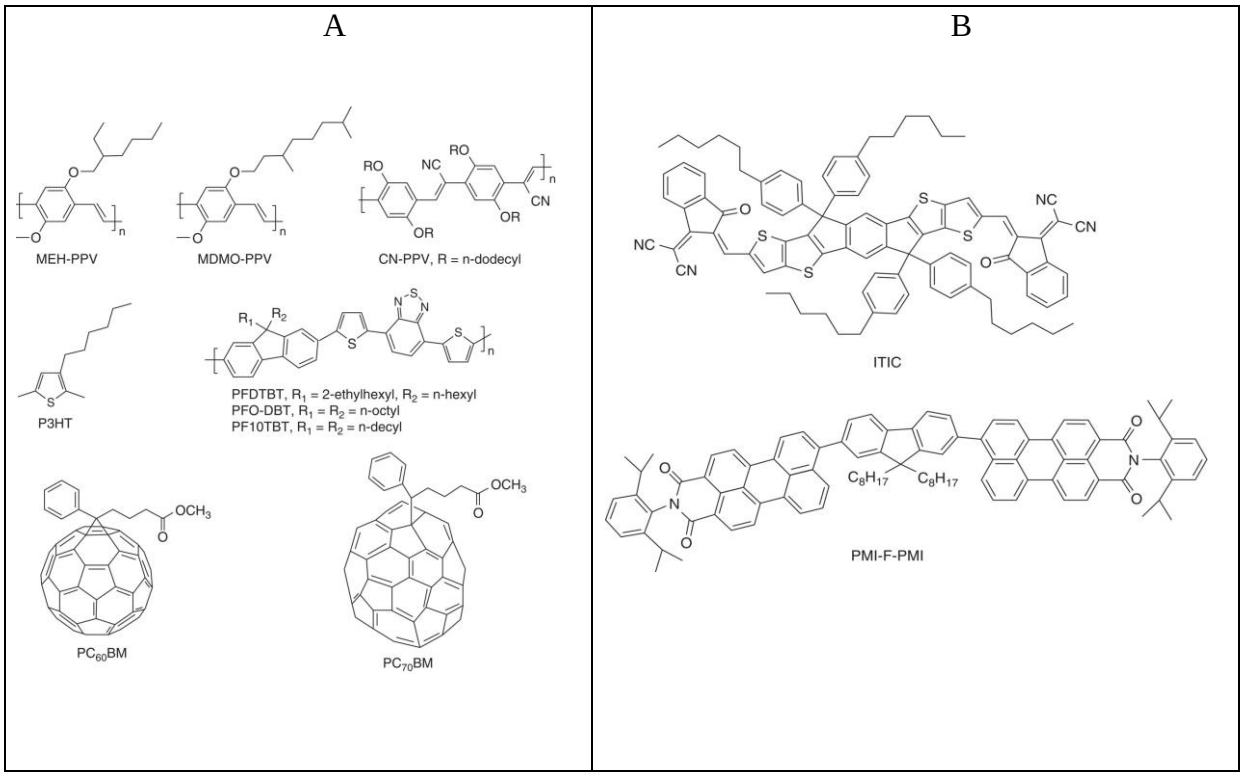

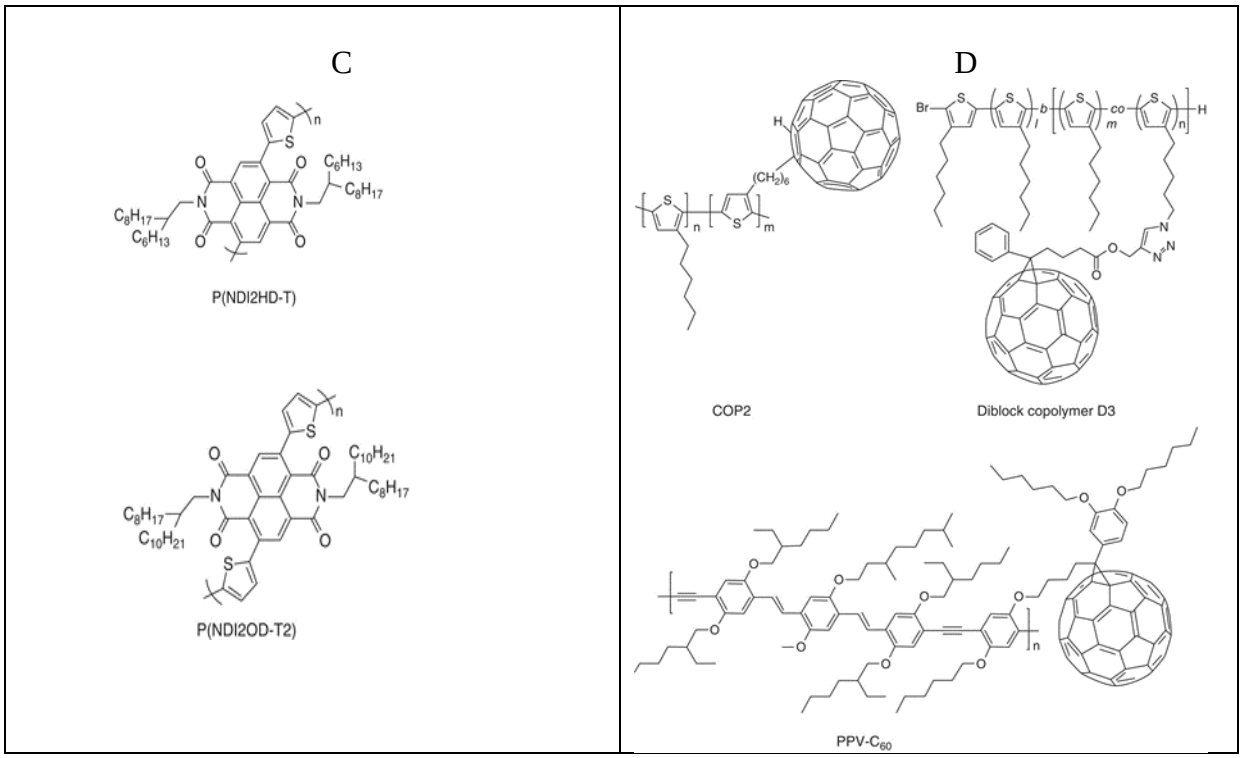

There are often mismatch in the optimum conditions for various phases in OSCs such as (light absorption, exciton splitting, charge carrier transport, and charge collection). For example, the broad polymers absorption spectrum may favor light harvesting due to their intrinsic structural disorder in solid films, and the distribution of the lowest-energy electronic transition may also increase the rate of non-radiative exciton decay, causing substantial loss in open-circuit voltage (Tuladhar et al., 2016). Meanwhile, specific small-molecule donor molecules with more ordered packing than polymers can effectively reduce the energy disorder, decrease non-radiative exciton decay, and avoid driving force loss. A better understanding of molecular loss management can regulate materials design for better functioning OSCs (Chen, 2019).

4.2 Dye-sensitized Solar Cell

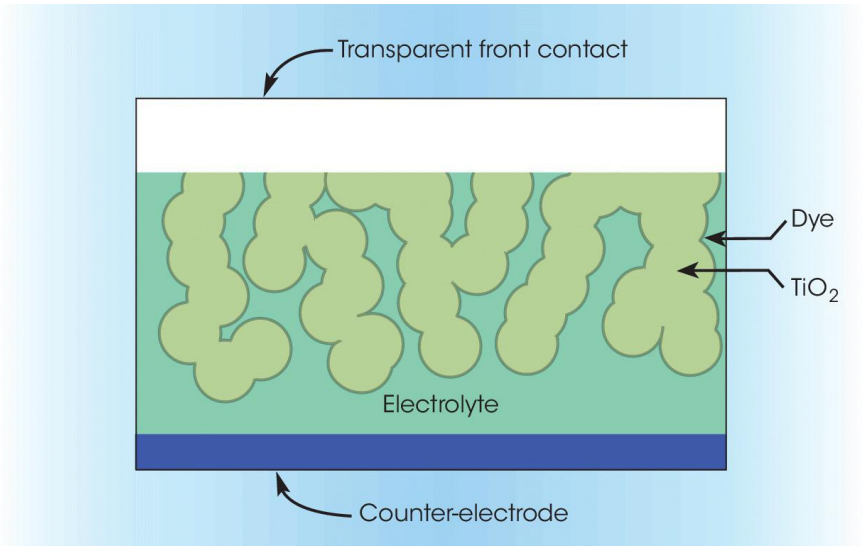

Figure 37: A dye-sensitized solar cell (Annick Anctil, Vasilis Fthenakis, 2012)

Dye-sensitized Solar Cell (DSSC or Graetzel cells) are a hybrid organic-inorganic technology utilizing organic dyes (typically ruthenium (Ru) based) coating on an electron-accepting material, such as titanium dioxide (TiO2) or less common ZnO, SnO_2, Nb_2O_5, inside an organic electrolyte to regenerate the dye. In the form of a nanoporous "sponge" of minute particles just 10nm (nanometers) across (V. M. Fthenakis et al., 2018), a thin-film TiO2 could work as an effective solar cell if coated with an organic dye, submerged in an electrolyte solution consisting a redox couple (usually triiodide/iodide (I_3^-/I^-)) which acts as donor electron to oxidized dye molecules and supplied with electrical contacts. Unlike the conventional p–n junction PV devices in which light absorption and light-generated charge transport occur within the same semiconductor, these functions are segregated in a DSC. TiO_2 on its own cannot work effectively because of its large bandgap but needs the organic dye as an absorber of light or functionally a TiO_2 "sensitizer", producing electrons that it injects into this inorganic semiconductor's conduction band. The dyes have the advantage of absorbing a wide solar spectrum, and the TiO_2 nanoparticles significantly improve the surface area of the adsorbed dye coating and thus the light absorption efficiency. Together their incorporation offers DSSC an emerging solar cell that does its job, affordable cost, and environment friendly. Even though DSSC's current recorded efficiency is just 14.3% (K. Kakiage et al., 2015), solar cell technology development will improve it further in the future.

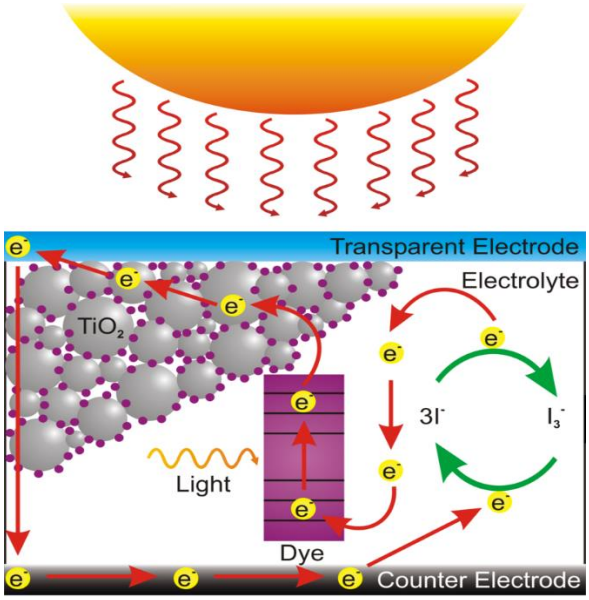

Figure 38: Schematic illustration of how a dye-sensitized solar cell works. (Jones, 2009)

The operating principle of a DSSC is when the sunlight enters the cell through a transparent front contact, the dye absorbs it and excites e^- from its highest occupied molecular orbital (HOMO) to its lowest unoccupied molecular orbital (LUMO). The excited electrons are dispersed into the conduction band of the semiconductor from where they diffuse to be gathered to a transparent conductive oxide (indium tin oxide (ITO) or fluorine-doped tin oxide (FTO)) and then re-enter the cell at the counter electrode (usually a Pt-sputtered/TCO glass) by passing through the external circuit to minimize the ‘’hole transport media’’ ($I_3^- \rightarrow I^-$). Eventually, the reduction agent (for ex. I^- ions) that diffuses from the counter electrode into the semiconductor film regenerates the oxidized dye in µs time range to its original state and completes the period of oxidation/reduction. The cell deriving electrical energy from light in this way does not undergo any chemical transformation (Antonino Bartolotta, and Giuseppe Calogero, 2019). The sequential events are below:

Activation: $TiO_2/Dye \rightarrow TiO_2/Dye^*$

Electron injection: $TiO_2/Dye^* \rightarrow TiO_2/Dye^+ + e^-$ (TiO2)

e^- (TiO_2) $\rightarrow e^-$ (FTO)

Electron reception: $I_3^- + 2e^-$ (Catalyst) $\rightarrow 3I^-$

Interception reaction: $1.5I^- + TiO_2/Dye^+ \rightarrow 0.5I_3^- + TiO_2/Dye$

(C. P. Lee et al., 2017)

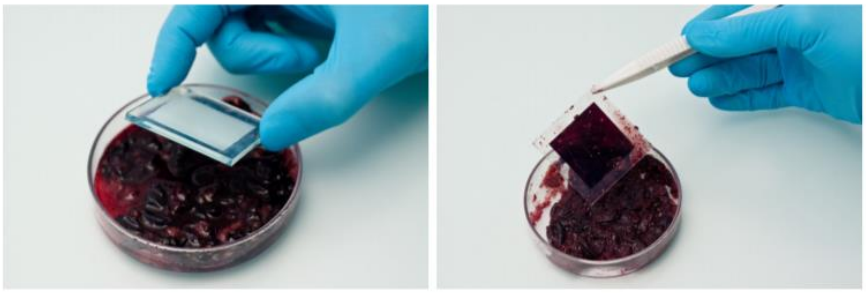

Figure 39: The TiO2 film is stained with the dye solution (Martineau, 2012).

The fabrication of DSSC can be done in school laboratory with the DIY-Kits. Firstly, TiO_2 powder/paste is applied on the TCO substrate by 'Doctor blading' method or screen-printing with a thickness of 5 - 15µm and porosity of 60 - 70% (Kretzer, 2013). Next, the TiO_2 film is immersed into the dye solution (for ex. pomegranate or raspberry juice) for about 12 - 18 hours (Kretzer, 2013) in room temperature, resulting in an intense film coloration (see figure 39). It is then rinse carefully with ethanol to eliminate non-absorbed remaining. The counter electrode is normally generated on a TCO substratum by sputtering Platinum. Finally, the two electrodes are sandwiched and filled with the electrolyte solution (such as Iodolyte AN-50 or Iodolyte Z-50) and sealed together with glass caps and sealing pads (Martineau, 2012).

Unlike amorphous silicon or other thin-film technologies, efficiency under radiant sunshine is perhaps not the most vital criterion for DSSCs. DSSCs performance in low light conditions and high temperatures, outdoor and indoor, has proved to be surprisingly effective. They use non-toxic and varied materials (TiO2 is a commercial product used in paints and toothpaste, for ex.), and their flexible modules can be grown in plastic substrates. DSCs offer tremendous potential for building-integrated photovoltaics (BIPV) because of their versatility, transparency, lightness, various sizes, shapes, and aesthetic specifications suitable for architectural design. These range from transparent and colored energy-producing walls, windows or skylights, lightweight membranes or curtains, roofing materials, partitions to decorative elements.

Challenges

The most used redox couple in DSCs (I_3^-/I^-) has some serious obstacles that they may not the pathway for DSC to achieve higher efficiency. Compared to the formal reduction potential ($E^{0'}$) (D+/D) of standard dyes (located at ca. 1 V vs. NHE), the ($E^{0'}$) (I_3^-/I^-) is comparatively negative (+0.35 V vs. NHE), resulting in a significant loss of approx. 0.65 V (Boschloo, 2019). The cause lies in the multi-step regeneration process involving the production of the reaction intermediate, I_2^- radical. In addition, I_3^- is very heavily colored and there is concern about its long-term particles' stability. Cobalt-based redox mediators may be a promising alternation that works well with suitable selective dyes. Cobalt complexes can show various redox potential, depending on their ligands chemical structure, which is contrary to the (I_3^-/I^-) system. The transformation of these complexes' counter ions is also an advantage since it emphatically affects different solvents' solubility. It enables these redox mediators to be used in water-based electrolytes, which has shown good stability in current research (H. Ellis et al., 2016). However, cobalt redox mediators also have one problem that needs to be improved

further: their electron transfer kinetics are relatively slow. Slow regeneration of oxidized dye molecules by Co_2^+ limits DSSC's performance even though slow kinetics for electron recombination with Co_3^+ caused by slow reduction of Co_3^+ species is beneficial (Y. Hao et al., December 2016). Another more promising redox mediators are copper (Cu) complexes, which exhibit faster dye regeneration kinetics than cobalt complexes and have long electron lifetimes. (M. Freitag et al., 2016). Moreover, a study has demonstrated that Cu complex with 4-tert butylpyridine which is more chemically stable than Cu_2^+ species, showing better performance with slow electron transfer kinetics (Y. Wang, T. W. Hamann, Oct 2018).

There are still several things to be explored to optimize DSSC efficiency further, one of them is the conductivity of the glass sheet. TCO glass's layer resistance has been seen to reduce when mixing extremely conductive but chemically unstable indium-doped tin oxide (ITO) with chemically stable but low conductive fluorine-doped tin oxide (FTO) together (K. Sharma et al., 2018).

It is possible to make almost unlimited forms of dye molecule modifications, where steric groups can be added to decelerate electron transfer of TiO2 and hole conductor or oxidized redox mediator. To improve light absorption and to enhance a better blocking effect, there is a need for more optimal dye packing on the TiO2 surface, co-sensitization is a good option, in which selecting proper dyes can achieve strong and panchromatic spectrum absorption. Via this process, the increase in light-harvesting further raises the density of the processed solar cell's short circuit current, J_{sc} (S. Ananthakumar et al., 2019). In many cases, co-sensitization also has the beneficial effect of preventing dye aggregation (Y. Hao et al., 2016). Dyes with relatively long excited-state lifetime and high fluorescence yield are another prerequisite for optimized efficiency. Any fast deactivation mechanisms should be avoided as they would harm the results. The injection efficiency will improve if the excitation lifetime is longer; several highly fluorescent organic dyes can achieve this. The R6 dye, used for adsorbing on mesoporous Al2O3 film, has been seen to obtain a good fluorescent lifetime of 260 picoseconds (Y. Ren et al., 2018). Currently, organic dyes with higher extinction coefficients are preferred than the conventional Ru-complex based dyes as they are shown in the figure below; many effective organic dyes have a prototypical structure of the donor pi-acceptor (D–π–A), which contributes to the movement of electron density towards the acceptor portion upon photoexcitation:

Table 2: Some redox mediators and dyes utilized in high performance DSCs.

Redox couple (R^+/R)	$E^{0'}$/V vs. NHE	Dye (type)	Recorded solar cell efficiencies. (V_{OC}, $J_{SC,}$ FF)	References

$[Co(bpy)_3]^{2+/3+}$ (bpy = 2,2′-bipyridine) 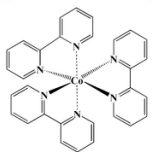 PF_6^- PF_6^-	+0.56	**SM315 (porphyrin-base D–π–A)** λ_{abs} = 668 nm (53 000 M^{-1} cm^{-1}) or 668 (53) abbr. E_{0-0} = 1.79 eV 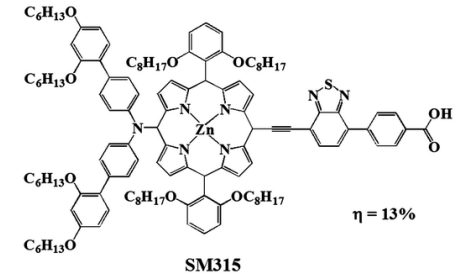 SM315 **R6 (D–π–A)** E_{0X} (THF) = 0.46 eV vs NHE λ_{abs} (THF) = 631 nm (8.18*10^4 M^{-1} cm^{-1}) M_W = 1803.53 g/mol $E_{0.0}$ = 1.77 eV 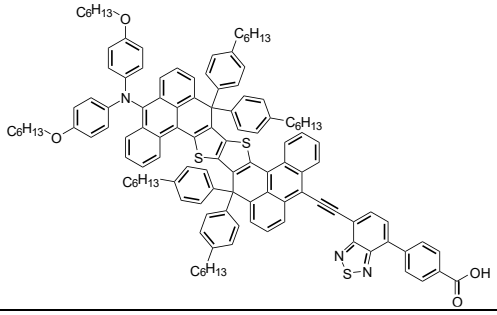	13% (0.91V, 18.1 mA cm^{-2}, 0.78) 12.6% (0.85V, 19.7 mA cm^{-2}, 0.754)	(Mathew S. et al., 2014) (Y. Ren et al., 2018) (Dyenamo, n.d.)
$[Co(phen)_3]^{3+/2+}$ 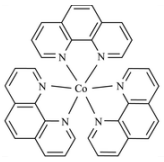 PF_6^- PF_6^-	+0.62	**Adeka-1+ LEG4 (D–π–A)** **Adeka-1** λmax = 507 (44), E_{0-0} = 1.85 eV 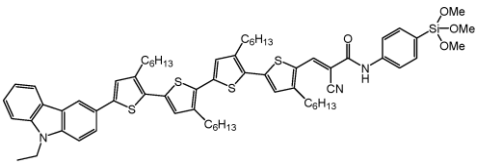 **LEG4 (or DN-F05)** E^0 = 0.88 V vs NHE λ max = 541 nm (49 000 M^{-1} cm^{-1}) E_{0-0} = 2.0 eV λ em = 717 nm (dichloromethane) M_W = 1125.58 g/mol	14.3% (1.01V, 18.3 mA cm^{-2}, 0.771)	(K. Kakiage et al., 2015) (Dyenamo, n.d.)

		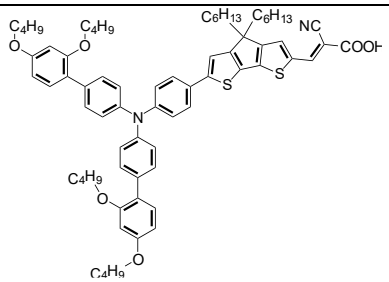		
$Cu(tmp)_2^{2+/+}$ 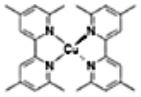 (TFSI) 	+0.91	**Y123** E^0 = 1.07 V vs NHE (dye adsorbed on TiO2, in acetonitrile) λ max = 530 nm (48 000 M^{-1} cm^{-1}) M_W = 1237.80 g/mol 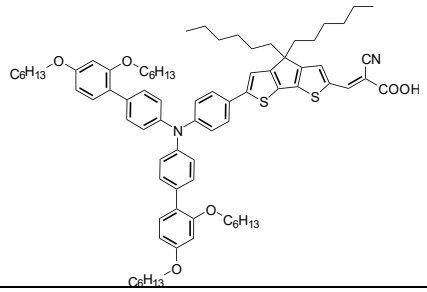	13.1% (1.05V, 15.7 mA cm^{-2}, 0.79)	(Yiming C. et al., 2018) (Dyenamo, n.d.)
$Cu(tmp)_2^{2+/+}$ (HTM)	+0.91	**WS-72 (D–π–A):** E_{0X} (on TiO_2 in MeCN) = 1.15 V vs NHE $\lambda_{abs,\ max}$ (DCM) = 545 nm (5.88*10^4 M^{-1} cm^{-1}) M_W = 1718.45 g/mol 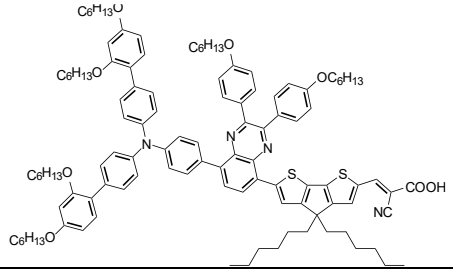	13.8% (1.07V, 11.7 mA cm^{-2}, 0.79)	(Weiwei Z. et al, 2018) (Dyenamo, n.d.)
$[Co(bpy)_3]^{2+/3+}$ 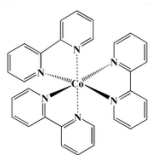 PF_6^- PF_6^-		**SGT-021 (porphyrin-base D–π–A)** λmax = 455 nm 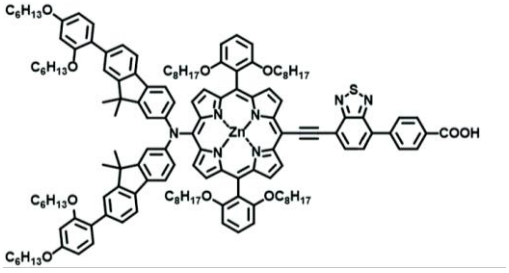	14.2 % (0.915V, 21.16 mA cm^{-2} , 0.734)	(Jung-Min Ji et al., 2020) (Haoran Zhou et al., 2019)

$E^{0'}$: formal reduction potential.

$E_{0\text{-}0}$: lowest transition energies (approx. HOMO-LUMO gaps).

V_{OC}: open-circuit voltage.

J_{sc}: short-circuit current density.

FF: fill factor.

Liquid redox electrolyte used in efficient DSSCs is another massive issue of concern. The electrolyte will freeze at low temperatures, stop power output and likely be damaged. In reverse, higher temperatures will expand the liquid, making it a risk to seal the panels. Moreover, in this kind of electrolyte, the iodide and triiodide reduction-oxidation couples are very reactive and corrosive to the other components, especially the sealant material. Because of the unavoidable chemical reaction between the sealant and the electrolyte, the liquid electrolyte leakage to cells usually happens in the DSSCs. This leakage is correlated to the module's long-term stability and energy conversion performance (active cell area can be dropped by 32% (M. Späth et al., 2003)). It causes encapsulation problems like liquid leakage or evaporation, which is hazardous to the living environment, dye desorption, instability issues, and less compatible ability (J. Zhang et al., 2017). Currently, sealant materials have gained some breakthroughs in durability. ThreeBond Inc. has patently developed acrylate-based (for primary sealing and end sealing) and epoxy-based (for main sealing) sealants. They consist of low polarity compounds and repel electrolytes with high polarities such as oil and water, making them resistant in the liquid electrolytes and slow moisture permeable. These sealants also have higher viscosities than almost other sealants (51-86 Pa-s, respectively (ThreeBond Inc., n.d.)). By adding a photopolymerizable functional group into the sealant’s compounds, they can be visible-light cured quickly at room temperature, ensuring the dye is not thermally damaged; thus, high productivity can be achieved.

Proposals on making entirely solid-state DSSC (ss-DSSC) have been around for a long time, in which a hole transporting material (HTM) is used to replace the liquid redox electrolyte. They have recently achieved promising results. HTMs based on conductive solid-state polymerized (SSP) polymers such as poly-3,4-ethylenedioxythiophene (PEDOT) polymerized on amphiphilic ruthenium Z907 dye-coated nanocrystalline TiO_2 layer have obtained a highly efficient and long-term stable ss-DSSC. This ss-DSC demonstrated excellent stability and dramatically improved photovoltaic efficiency over 1000 h, which is considerably better than liquid-DSSC. (Y. J. Jang et al., 2019). The same expected effects of high efficiency and long electron lifetimes can also be found at the Cu-complex redox electrolyte (M. Freitag et al., 2015). Besides, molecular organic hole conductor for example 2,2′,7,7′-tetrakis(N,N-di-p-methoxyphenyl-amine)9,9′-spirobifluorene (spiro-MeOTAD) to alter liquid redox electrolyte is also a promising option in fastening dye regeneration in the regime of picosecond. However, this typically results at the expense of faster recombination between electrons in TiO2 and holes in the HTM, reduction of the output voltage leading to poorer overall efficiency. It could be beneficial to add an intermediate redox level so that formed holes can be eliminated easily from the interface of dye-loaded TiO_2 (Boschloo, 2019). Synthetic

modifications of dyes and HTMs can also decrease the recombination and enhance V_{OC} (I. Benesperi et al., 2018).

4.3 Perovskite Solar Cell

According to National Renewable Energy Laboratory, USA, the record efficiency of Perovskites in 2020 is 25,2% by Solar Frontier and monolithic Perovskites/Si tandem is 29,1% by HZB, and monolithic Perovskites/CIGS tandem is 24,2% by HZB (N. R. E. Laboratory, 2020). Perovskites solar cell (PSC) is the fastest-growing high technology ever in photovoltaic history. Within 10 years, this exceeds the best efficiencies of thin-film crystal silicon, CIGS and CdTe solar cell technology that have been studied for so many decades. However, Perovskite cells are not yet commercially available because its remarkably high efficiencies were only obtained in the laboratory with observations at a tiny amount ($\leq$1 cm^2), which become unstable after minutes (V. M. Fthenakis et al., 2018).

Perovskite is a name of a compound class that is any material with a crystal structure like the perovskite mineral, calcium titanium oxide ($CaTiO_3$). A perovskite solar cell contains a perovskite structured compound, which is frequently a hybrid organic-inorganic lead or tin halide-based material (N. Y. Nia et al., 2019). Perovskite structure written in general is ABX_3. A, B are two different-size cations. Typically, A is smaller atom (Ca+, $CH_3 NH_3^+$, $C_3 N_3 H_6^+$), and B is usually lead (Pb). X is anion, X can be halogen or a halogen mixture (Br-, I- or Cl-). A proper formulation of A, B, X is the one that follows the Goldschmidt's tolerance factor (H. Kronmüller et al., 2007):

$$t = \frac{r_A + r_X}{\sqrt{2}(r_B + r_X)}$$

With r_A is the ion radius of the A cation, r_B is the ion radius of the B cation, r_X is the ion radius of the X anion. $0.8 \leq t \leq 1.15$ is the condition for a semiconducting metal-organic perovskite crystal to grow, an ideal fit between octahedrons of BX_6 and A cation (G. Kieslich et al., 2015). Indeed, if $t < 0.8$, there is no crystal growth among A, B, X ions or even if t is close to 0.8, BX_6 tilting will increase, which results in lower symmetry crystals. If $t > 1.15$, a more complex structure is created with intermolecular deformity (N. Y. Nia et al., 2019). However, metal-organic halide perovskites in fact have non-spherical organic cation symmetry, meaning it is difficult to correctly measure the organic cation radius and determine the tolerance factor of cation-anion interaction properly (N. Y. Nia et al., 2019). Thus, to determine the PSCs crystal structures' stability in a more comprehensive and objective evaluation, a so-called geometric octahedral factor, μ is also set to assess the tilting between B cation and X anion along with the Goldschmidt tolerance factor (M. R. Filip, F. Giustino, 2018):

$$\mu = \frac{r_B}{r_X}$$

Perovskite's ideal band gap for terrestrial single-junction solar cells is generally between 1.2 and 1.62 eV, as seen for the best-performing modules (A. M. Ganose et al., 2017). Especially, the 1.34 eV band gap can attain possibly highest efficiency of 33.4 % based

on the traditional Shockley-Queisser limit calculation, and organometallic halide perovskite is expected to match this value with a suitable chemical composition. High coefficients of absorption ($1.5 \times 104cm^{-1}$ at 550nm for $CH_3NH_3PbI_3$) (N. K. Kumawat, 2015), less-sensitive to structure defects, a range of tunable bandgaps for single-junction gadgets and Si-based tandem cells, and long diffusion lengths (3D perosvkites with tertbutylammonium cation show up to 1.8μm in electron and hole diffusion lengths) (C. Liang et al., 2019), low excitonic binding energy (14–25 meV) (V. D'Innocenzo, 2014), long-lasting carrier transport, facile solution process are all the outstanding advantages of PSCs thanks to researchers' effort to understand the compound, improve the composition, microstructure, and layers of complementary charge transport in PSCs structure (N. Y. Nia et al., 2019).

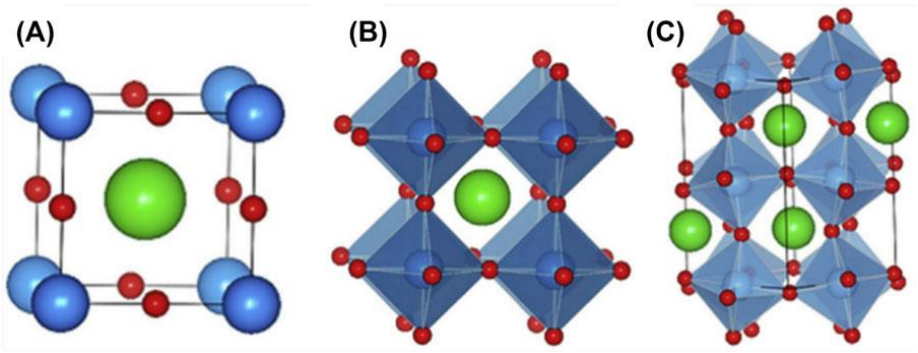

Figure 40: Different ideal type of cubic perovskite unit cell. cations A are blue, cations B are green, anions X are red (Qi Chen et al., 2015).

In figure (a), cations A (blue) occupy the lattice corners, cations B (green) occupy the interstitial site, and anions X (red) occupy faces of lattice. Figure (b) indicates an alternate view showing cations B assembled around anions X to form BX6 octahedra, since B-X bonds are responsible for deciding electrical properties. In figure (c) BX6 octahedra tilting due to non-ideal size effects and other influent factors causing strain on B-X bond (Qi Chen et al., 2015).

Crystallization

A perovskite has low nucleation and crystallization activate energy at 56.6–97.3 kJ mol^{-1}, allowing its films to be quickly processed by different kinds of low-temperature mass manufacturing techniques such as ink-jet printing, blade coating, and roll-to-roll printing (F. Huang et al., 2019). Its crystallization growth mechanism has three stages: supersaturation, nucleation, and forming into a large crystal, which may also undergo stable or metastable intermediate phases based on the deposition system (N. Y. Nia et al., 2019). First, on the substrate, a precursor solution is dropped down, and the solvent is immediately evaporated on the surface, the solute content gains up, and the solution soon reaches saturation (Cs). At this point, the solution becomes supersaturated only if the solvent keeps evaporating, with a Gibbs free energy more significant than the newly formed nuclei's surface energy. Next stage, ions, atoms in the solution transform into nuclei, called the nucleation phase. The nucleation rate raises with increased supersaturation, resulting in higher density (more nuclei) with a greater number of smaller crystals. When the solution concentration is lower than supersaturated solution concentration, nuclei formation finishes, and the crystal starts to grow subsequently.

The crystallization continues happening until the concentration of growth species drops below Cs (N. Y. Nia et al., 2019).

Nowadays, there are two main techniques to grow perovskite thin films: the one-step method and the two-step method (N. Y. Nia et al., 2019).. The one-step method only needs one stage of deposition for the perovskite crystal to form. Instantaneous nucleation happens from the precursor solution in this process, without any stable intermediate phase being formed or with a rapid going through a metastable intermediate. Solvents in use are dimethylformamide (DMF), acetonitrile (MeCN), γ-butyrolactone (GBL), N-methyl pyrrolidone (NMP), dimethyl sulfoxide (DMSO), etc. (B. Jo Kim et al., 2016). The downside of these solvents is that their slow evaporation limits the rate of nucleation, causing rapid crystallization but low nucleation density. Antisolvent-induced one-step method can be an alternative option to obtain dense and uniform perovskite films. It includes the precursor solution's spin coating then instant exposure to antisolvent (chlorobenzene or diethyl). The anti-solvent rapidly removed the original solvent, resulting in a high degree of supersaturation, prompting other crystal nuclei to be produced (Manda Xiao et al., 2014).

In the two-step process, first is the deposition of the PbX_2 layer, followed by conversion to perovskite in organic cation/halide solution (H.-S. Kim et al., 2012). Since the PbX_2 layer's deposition processes and control technique are scalable and flexible, uniform, and maximum coverage could be easily achieved, improving the perovskite film's consistency. Most notably, great progress on reaction/growth mechanism resulted in updated two-step processes that improved perovskite efficiency and improved system performance (N. Y. Nia et al., 2019). Accordingly, two $MAPbI_3$ perovskite forming mechanisms were proposed: one is a simple solid-liquid interfacial reaction at low concentration of methyl ammonium iodide (MAI) and the other is a high concentration of MAI dissolution-crystallization (Z. Song et al., 2015), (T. Wang et al., 2019). If the MAI concentration is less than 8 mg mL −1, in situ transformation (interfacial reaction) takes 2 min. Likewise, if the MAI concentration is more than 10 mg mL −1, $MAPbI_3$ perovskite crystals form instantly through a solid-liquid interfacial reaction. Another MAI reaction with underlying PbI_2 is discontinued, resulting in incomplete reaction (Y. Fu et al., 2015).

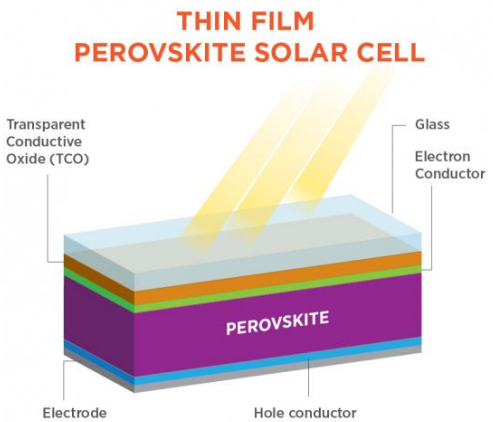

Figure 41: Thin-film perovskite solar cell (U.S. Department of Energy's Office of Energy Efficiency and Renewable Energy, n.d.).

Challenges:

The commercialization of perovskite PV technology, amid considerable optimism, involves addressing three main challenges: exhibiting long haul working stability of PV modules (a solar cell is supposed to remain operational for more than 25 years) (D. H. Kim et al., 2018), scaling up to wide areas, and preventing or mitigating actual and potential risks related to the utilization of toxic lead.

Instability is a major obstacle for PSC to be commercialized. Extrinsic factors (e.g., moisture, temperature, illumination) and intrinsic factors (e.g., bond strength between cations and anions, ion migration) that cause chemical and structural degradation are primarily responsible for this instability (O'Kane, n.d.). These degradation processes contribute to organic cation decomposition of the ABX3 crystal, anion gaseous forms, BX2 salts, and pure restored element B. In this case, a study about double or triple cationic preparations for balancing the molecular packing density can provide the functional trends for perovskite molecular stabilization. Attempts to enhance PSCs' stability by depositing extreme crystalline perovskites with big crystal size may not be sufficient as the crystalline grain size decreases gradually over time due to the dynamic procedure of formation and decomposition.

The most researched perovskite component for PSC prototypes is $MAPbI_3$, due to its crystallization at low temperature (100 ° C) and high solar cell efficiency (more than 24%). However, the low temperature conversion to the photoactive process (about 320 K) occurs due to the weak interaction between the MA and PbI_6 positions ($t_{factor} = 0.83$) and induces some instability (B. Conings et al., 2015). Several $MAPbI_3$ film studies have shown significant changes in phase and composition at temperatures > 50°C. Three degradation mechanisms induced by illumination of sunlight and thermal stress at 40-80°C: reversible organic cation decomposition: $CH_3NH_2 + HI$, irreversible or detrimental formation of gaseous products: $NH_3 + CH_3I$, and reversible cation-anion decomposition: $Pb(0) + I_2(g)$. If only reversible organic cation decomposition and reversible cation-anion decomposition happen and avoid the second reaction, then encapsulated $MAPbI_3$ can be restored during the off-illumination period (N. Y. Nia et al., 2019). First, it is important to encapsulate the system to prevent the perovskite from exposing with atmospheric air and avoid the leakage of volatile compounds emitted from the perovskite at the same time. Second is preventing irreversible reactions by circumspect selection of the organic cations in the perovskite compositional formula. Third, the selective interactions in the volatile released materials must be as chemically inert as possible (T. Liu et al., 2017,).

Chittaranjan Das et al. have indicated that room temperature ultrathin atomic layer-deposited (ALD) Al_2O_3 on the perovskite surface hinders the iodide migration very effectively without causing any drastic changes to the perovskite absorber properties, thus prevent degradation in perovskite solar cells. It also helps to maintain the perovskite film's original properties during exposure to light and air under actual

working conditions, thereby enhancing solar cell stability (described in figure). This is believed to be one step closer to perovskite PV mass-manufacture (C. Das et al., 2020).

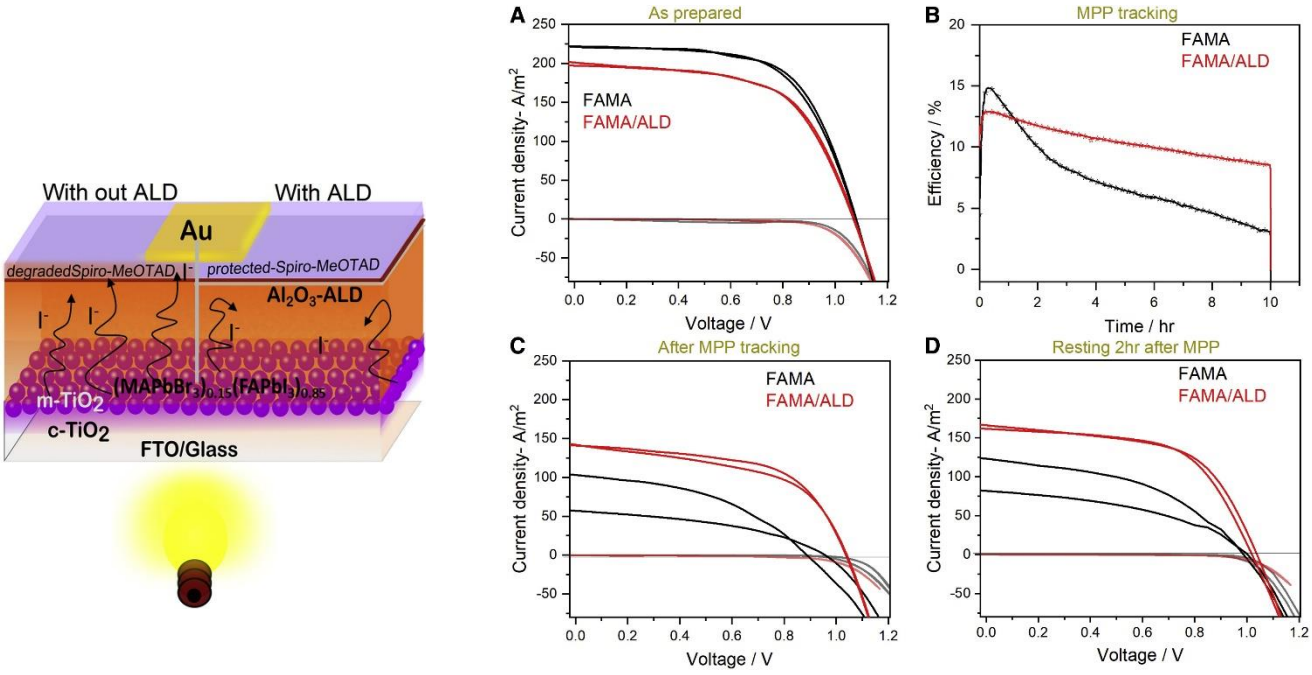

Figure 42: Compared structures, performances, and stabilities of perovskite solar cells with FAMA (formamidinium/methylamine) and FAMA/ALD layer. From (A) to (D) is the power conversion efficiency of the devices in ambient operating conditions. The current-voltage curves (A), the maximum power point tracked for 10 hours (B), the direct measured current-voltage curve after 10 h of maximum power point (MPP) (C), and the recovery examination after resting for 2 hours in the dark (D) of the two perovskite cells (C. Das et al., 2020).

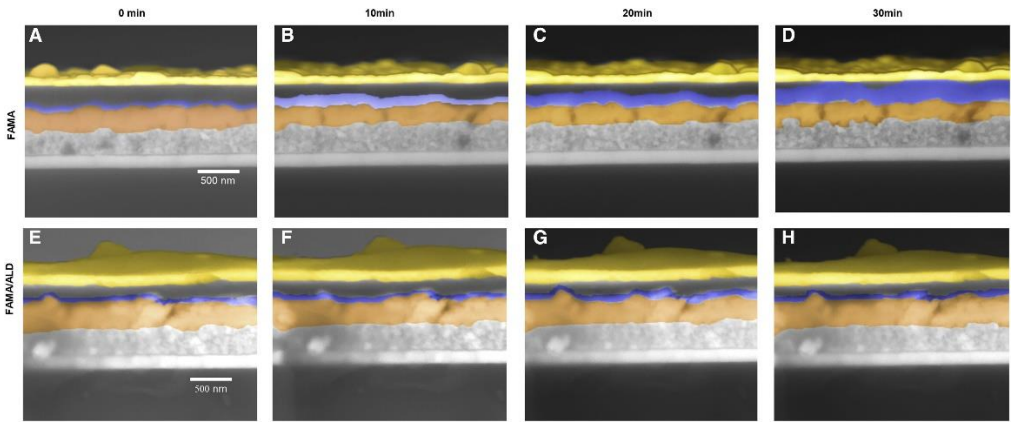

Figure 43: SEM on Cross-Section of FAMA (pictures A-D) and FAMA/ALD (pictures E-H) to observe Iodide migration. FAMA is in orange, Au in yellow, and iodine migration

in light blue. Evolving morphology and elementary combination was studied over time, at intervals of 0 (A-E), 10 (B-F), 20 (C -G) and 30 (D-H) minutes. (C. Das et al., 2020).

The samples in experiment of Chittaranjan Das's study are $(FAPbBr_3)_{0.15}(MAPbI_3)_{0.85}$ perovskite SCs with FAMA/SpiroMeOTAD (FAME) or FAMA/(Al_2O_3-)ALD/SpiroMeOTAD (FAMA/ALD) layer. Figure (A) show that these FAMA and FAMA/ALD devices have an efficiency of –15.5% and 13.9%, respectively. It can be seen in figure (B) that after a continuous 10 hours, the MPP sharply drops from 15% to 2.9% for FAMA (efficiency decreases by 80%) and from 13.9% to 8.5% for FAMA/ALD devices (efficiency decrease by 39%). J-V curve in figure 43 (C) indicates that FAMA and FAMA/ALD-base cells are 2% and 8.9%, respectively. In conclusion, it is clear after 10 h of MPP monitoring, the same FAMA-based solar cell displays major hysteresis, while the FAMA/ALD-based solar cell shows negligible J-V hysteresis. We can see in figure 43 that the iodine migration in FAMA/ALD-based stay unchanged after a prolonged exposure, meanwhile iodine migration in FAMA/ALD continue to grow thicker over times.

Besides, proper encapsulation will address some of the stability issues related to moisture exposure but work in modifying the device layers themselves has also shown promise. It was demonstrated that encapsulation of halide perovskite CsPbBr3 nanocrystals by a tripodal tertiary ammonium bromide ion pair ligand [tris(2-aminoethyl)ammonium bromide (TREN·4HBr)] could markedly enhances photoluminescence, and stability concomitantly via anion defect elimination (J. Pradhan et al., 2020).

Another major challenge preventing perovskite solar cell from commercialization is using lead as the pollution of the natural environment by toxic metals is especially well recognized as a major global concern. The threats of lead in perovskite solar cells are controversial. Some sources suggested that any amount of lead is unacceptable. In contrast, others reported that lead theoretically used in PV would be negligibly limited relative to lead consumption in other industries such as aviation fuel, coal-fired electricity, and aviation fuel (V. M. Fthenakis et al., 2018). Indeed, in Europe and the USA, lead regulations already prohibit the shipment of lead perovskite PVs in these regions (A. Babayigit et al., 2018). Solutions that absolutely eliminate lead appear the most suitable option. Pb-free alternatives such as Sn-, Ge-, Bi-, Sb-based perovskites, however, have demonstrated much poorer efficiencies and worse stability than Pb-based cell (Sn still has toxic properties). Therefore, it is necessary to understand better the structure-properties as well as the crystallization of these lead-free perovskites, particularly in many cases, this process is very different from that of lead halide perovskites. It is also crucial to comprehend the excited state dynamics of perovskites for further optimization of PSCs, as charging and recombination processes play essential roles in optoelectronic efficiency dictation (Qi Zhang et al., 2018). A recent study about less-toxic solvents for PSC has suggested that dimethyl sulfoxide (DMSO) can be a potential main solvent due to its high donor number benefiting the formation of a stable intermediate. However, so far, DMSO has been only used as a kind of additive in the perovskite precursor solution, thus requiring further research (Rosario Vidal et al., 2020).

4.5 Multi-junction solar cells

Multi-junction solar cells (MJSCs) are the most efficient photovoltaics at present that surpass the Shockley–Queisser limit for single-junction cells. Six-junction solar cell developed by USA National Renewable Energy Laboratory (NREL) has obtained 47.1% of the world best efficiency under concentrated illumination; and best performing concentrator three-junction solar cells achieved 44.4% (N. R. E. Laboratory, 2020). Other MJSCs' types of best performances are shown in figure below:

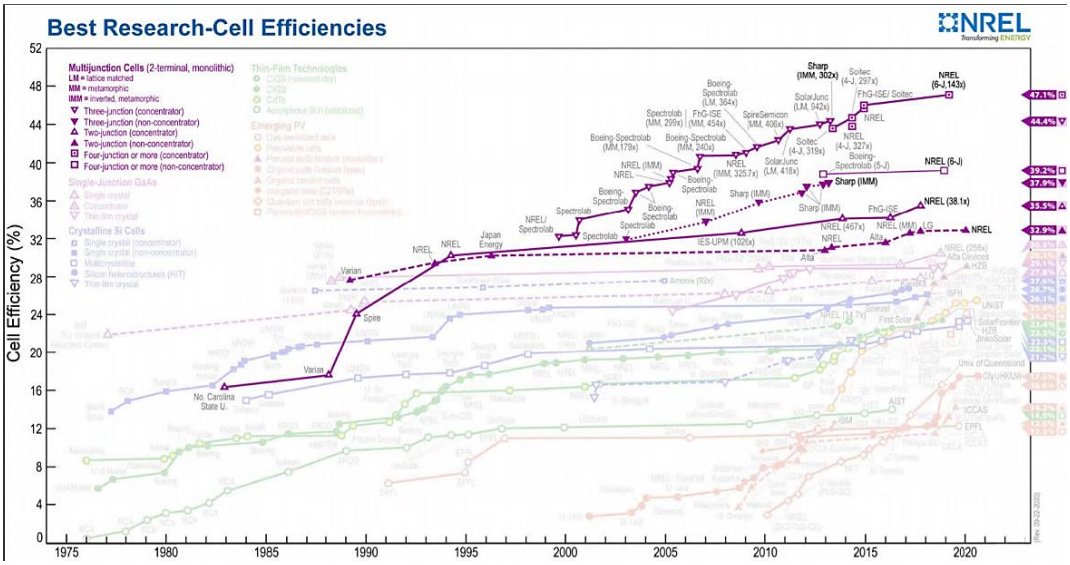

Figure 44: Best efficiencies of different types of MJSCs in 2020 (N. R. E. Laboratory, 2020).

MJSCs are made by a so-called III-V semiconductor materials. They may not be considered as an accurate thin-film PV technology in comparison to thin-film silicon, CdTe, CIGS, or organic PV as some of their concepts utilize GaAs wafer as a substrate. Nevertheless, compared to the crystalline silicon wafers thickness, this III-V based absorber layer itself is still regarded as thin. The III-V components are the elements with three valence electrons, such as indium (In), gallium (Ga), or aluminum (Al), and elements having five valence electrons like arsenic (As) or phosphorus (P). Their combination into compounds creates the most interesting high efficiency semiconductor materials to explore, such as gallium arsenide (GaAs), indium phosphide (InP), indium arsenide (InAs), gallium phosphide (GaP), and more complex alloys like GaInAs, GaInP, GaInAsP, AlGaAs, AlGaInAs, and AlGaInP... Under both AM1.5 normal test conditions and concentrated Sun conditions, they result in the best conversion efficiencies, making them primarily used in space applications and concentrator photovoltaic systems (CPV) (A. HM Smets et al., 2016)

The basic concept of MJSCs is to combine multiple III-V materials with unique band gaps. Its architecture consists of the most elevated bandgap junction first, and last is the lowest bandgap material as photons with energy below the bandgap are distributed without loss (as shown in figure 45). The light is absorbed in the top cell at the start, then the remaining light goes into other cells below respectively, and finally enters the bottom cell. Since the photons must travel through the cell to enter the right layer to be

absorbed, it is critical to utilize transparent conductors to capture the electrons emitted at each layer (G. C. Righini et al., 2019).

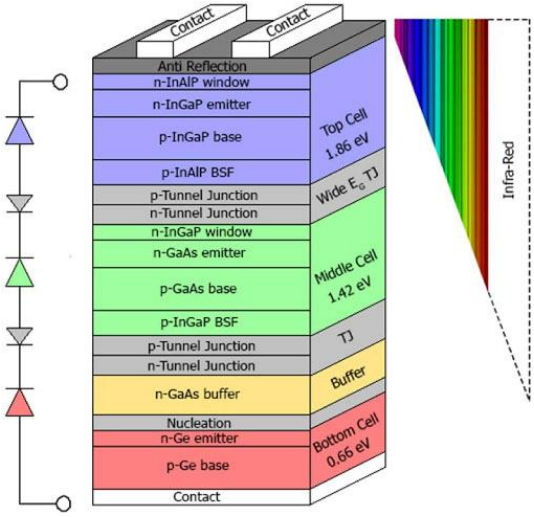

Figure 45: The structure of a common three-junction solar cell and solar spectrum penetration depth illustrated (J. Pritchard et al., 2016)

The two popular manufacturing techniques for growing III-V SCs on a substance substrate like silicon wafers are direct-epitaxial growth and wafer bonding-based layer transition (W. Yang et al., 2011). In the epitaxy deposition process, crystalline overlayers are set to take on the substrate's crystal lattice structure by depositing them on a crystalline substrate. Besides using silicon wafer, germanium (Ge), InP or engineered InP substrate such as InP-sapphire, InP-SiO2 have also been demonstrated to deliver high III-V semiconductors quality (A. HM Smets et al., 2016), (R. Krause et al., 2014), (C. Besancon et al., 2019). Firstly, the precursor atoms coming from diverse elemental sources are introduced to grow the layers. For instance, in the deposition of GaAs, Ga and As atoms are oriented to a growth surface in ultra-high vacuum conditions, and the substrate can be germanium (Ge). On Ge, the GaAs crystalline lattice is grown gradually layer-by-layer and adopts the crystalline substrate form. As this growth process is very long, it deposes consistent materials without any vacancy defects. Moreover, manufacturing under high vacuum conditions avoids impurities absorption. As a result, the III-V semiconductors made by this method has an extremely high degree of purity. Dopants such as DMZn, CBr_4 , SiH_4, DETe and DTSe can also be added to make the subcell layers n-or p-type (A. HM Smets et al., 2016) (T. N. D. Tibbits et al., 2014). However, the fact that this process is time-consuming and expensive may cause MTJCs unfavorable in commercial competition. Thus, one alternative solution could be the metal organic vapor phase epitaxy (MOVPE). This method promotes the epitaxial crystalline growth by alluring precursor gases such as $Ga(CH_3)_3$, $In(CH_3)_3$, AsH_3, PH_3 to have surface reaction with hydrides (A. HM Smets et al., 2016).

Direct wafer bonding is an effectual technique that stacks lattice-mismatched materials without inducing dislocations. Two crystal structures are carried in forming covalent bonds together at the interface (Q.-Y. Tong, U. Gösele, 1998). The main challenges of this process are the highly-demanded specifications for surface quality and material preparation (may include epitaxial process). The two wafer faces must be cautiously polished (chemical mechanical polishing) to have a very low surface roughness and be free of pollutants, native oxides, and surface states must be well conserved for high conductivity. If careful preparation is not done in advance, it would be tough to combine due to lattice or thermal expansion mismatch (T. N. D. Tibbits et al., 2014). Anyhow, this technique provides the ability to incorporate optimal and non-defect materials in an MTJC device. Wafer bonding technique can be used to combine epitaxial grown GaAs/GaInP two-junction solar cell on silicon wafers to utilize the benefits of high PCE of III-V SCs with the low-cost fabrication of silicon platform (Frank Dimroth et al., 2014). Rainer Krause et al. have successfully combined GaInP/GaAs as the top tandem cell and GaInAsP/GaInAs as the bottom tandem cell on an engineered InP-sapphire substrate, giving a four-junction solar cell with ideal bandgap cooperation and superior material quality for all junctions. The surface roughness measured was below 5 nm, and defect densities was smaller than 20-200 particles for 30μm-0.3μm particles (R. Krause et al., 2014).

Since the MJSC layers are linked electrically and mechanically in a monolithic cell. Like this, the selection of materials for each layer must conform with precise prerequisites, not only based on the appropriate distribution of the spectral interval of solar radiation but also identified with their mechanical and electrical properties. In detail, the crystal lattice constant of the subcells should be firmly coordinated for maximum growth and subsequent crystal consistency, inducing lattice-matched devices. Therefore, to acquire the best efficiency, lattice matching and current matching are essential (G. C. Righini et al., 2019). As seen in Figure 46 below, a significant challenge of depositing III-V semiconductor materials is that the materials' lattice constants are different. There is a special bandgap-lattice constant combination of any III-V semiconductor. Interfaces between various III-V components, thus, reveal a lattice mismatch, as shown in Figure 47. Not every valence electron can bond with a neighbor because of this mismatch. An extraordinary mismatch level or other flaws in the growth process can prompt crystal deformities, leading to electronic property degradation but by lattice matching, this problem can be solved. For example, GaAs has the same lattice constant as Ge, as we can see in Figure 46. Hence, GaAs and Ge interfaces can be made without any alignment defects due to mismatched lattices (A. HM Smets et al., 2016).

There is always the same current flowing through every junction since each sub cell is associated electrically in sequence. Thus, to ensure current matching, correct bandgaps must be also selected so that in each of the sub cells, the architecture spectrum can adjust the current generation (G. C. Righini et al., 2019).

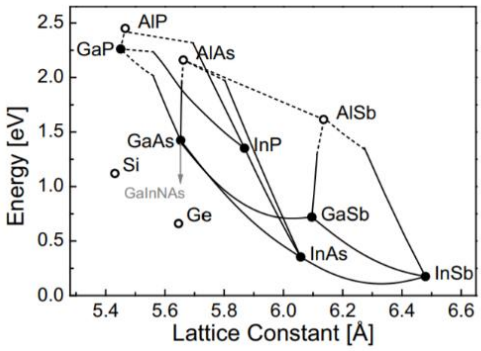

Figure 46: The bandgap is plotted as a lattice constant function. The black/white circles represent indirect/direct semiconductors. The solid/dashed lines represent the according indirect/ direct ternaries (D. Lackner et al., 2017).

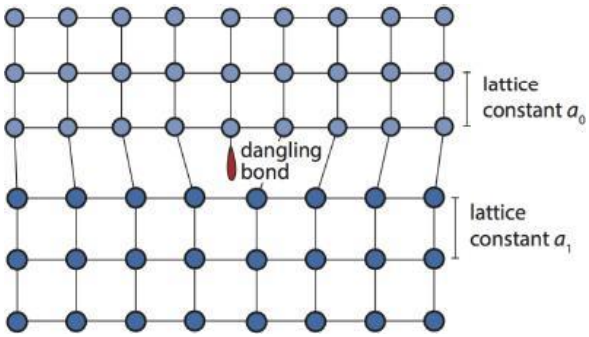

Figure 47: Illustration of the lattice mismatch at an interface of two different III-V materials. (A. HM Smets et al., 2016)

In addition, large coefficients of absorption, long lifetimes of the minority carrier, high portability are necessary factors for high performance, giving reasons for the materials usually chosen in MJSCs. A mentioned-above example of popular 4-junction configuration with an excellent efficiency of 44,7 is 1.88 eV gallium indium phosphide (GaInP or InGaP) for the top subcell, 1.44 eV gallium arsenide (GaAs) and 1.11 eV gallium indium arsenide phosphide (GaInAsP) for the middle subcells, and 0.7 eV indium gallium arsenide (GaInAs) for the bottom subcell. Its wafer was engineered with a thin transferred film InP material (in of few hundred nm of thickness for the aim of cost competitiveness) on a sapphire support substrate, following is the Smart Cut™ technology. This development was collaborated by Fraunhofer ISE, Soitec and CEA-Leti. (R. Krause et al., 2014).

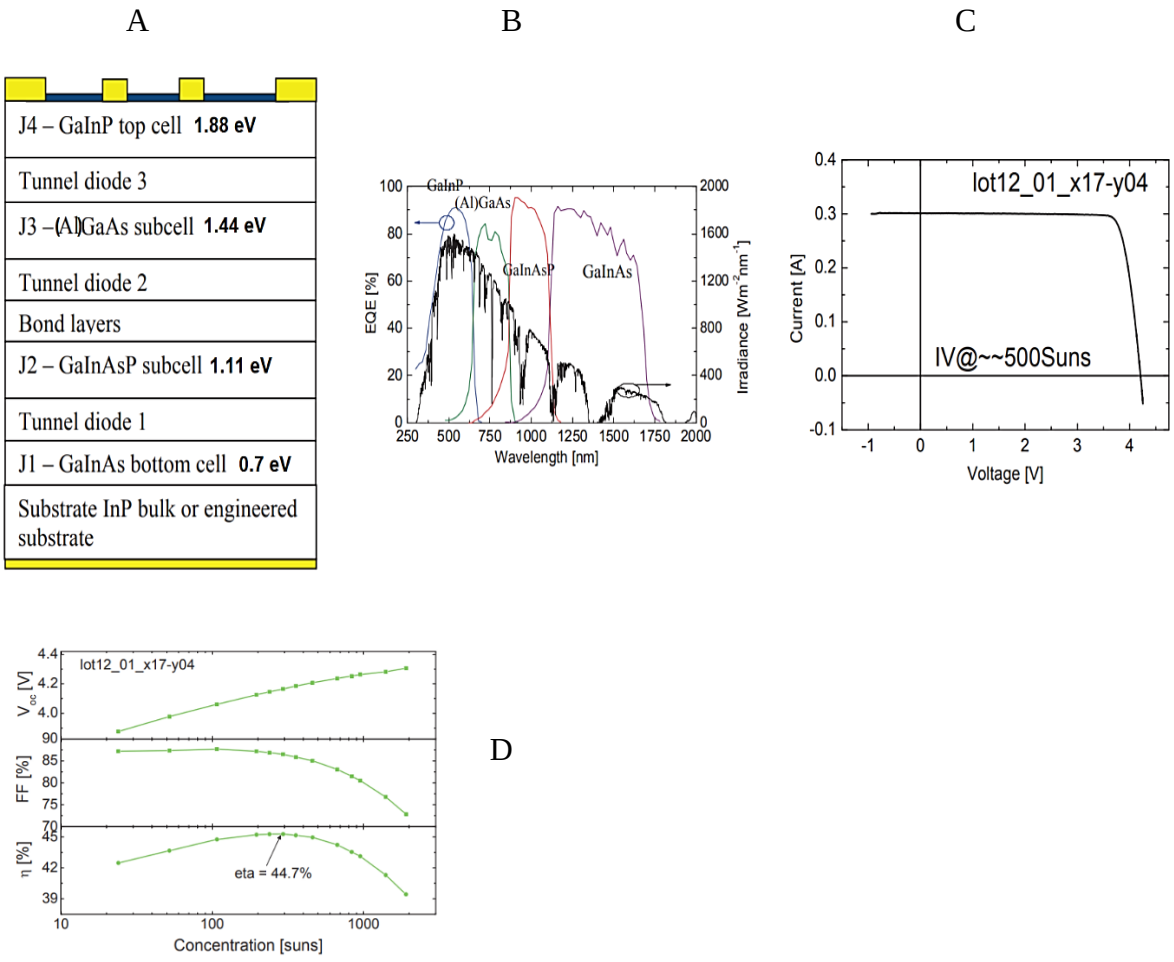

Figure 48: (A) The schematic structure of a wafer bonded four-junction GaInP/GaAs/GaInAsP/GaInAs solar cell.
(B) Its external quantum efficiency (EQE).
(C) Its I-V characteristics at appx. 500x concentration of the AM1.5d spectrum.
(D) Its I-V characteristic under concentration with a surface area of about 5mm^2 each (R. Krause et al., 2014).

As a function of concentration, the IV characteristics of the best solar concentrator cell of GaInP/GaAs/GaInAsP/GaInAs have been calculated (figure 48). Figure C shows IV curves of a wafer bonded 4-junction solar cell under concentration measurement. Under concentration, the fill factor gradually rises (Figure D) and peaks at about 100 suns before decreasing with raising concentration due to increased serial resistance. At around 300 sun concentrations, the maximum conversion efficiency is achieved with a 44.7 ± 3.1% value. With a calculated value of over 39 ± 3.0% at 1300 suns, the performance remains high in a wide concentration range from 100 to 1300 suns (R. Krause et al., 2014).

In recent years, there have been many studies in building concentrator six-junction solar cell devices that can reach and exceed 50% efficiency under high direct normal irradiance (DNI) regions, opening a pathway for low-cost utility-scale solar

technology systems. A potential strategy is the inverted metamorphic multi-junction (IMM), or lattice-mismatched multi-junction, a single-growth, single-substrate platform that has obtained almost 46% efficiency with four-junctions, which is possibly applied to 6-junction system (R. M. France, 2016). J. F. Geisz et al has developed 6J IMM concentrator solar cells and addressed remaining challenges to achieve 50% efficiency.

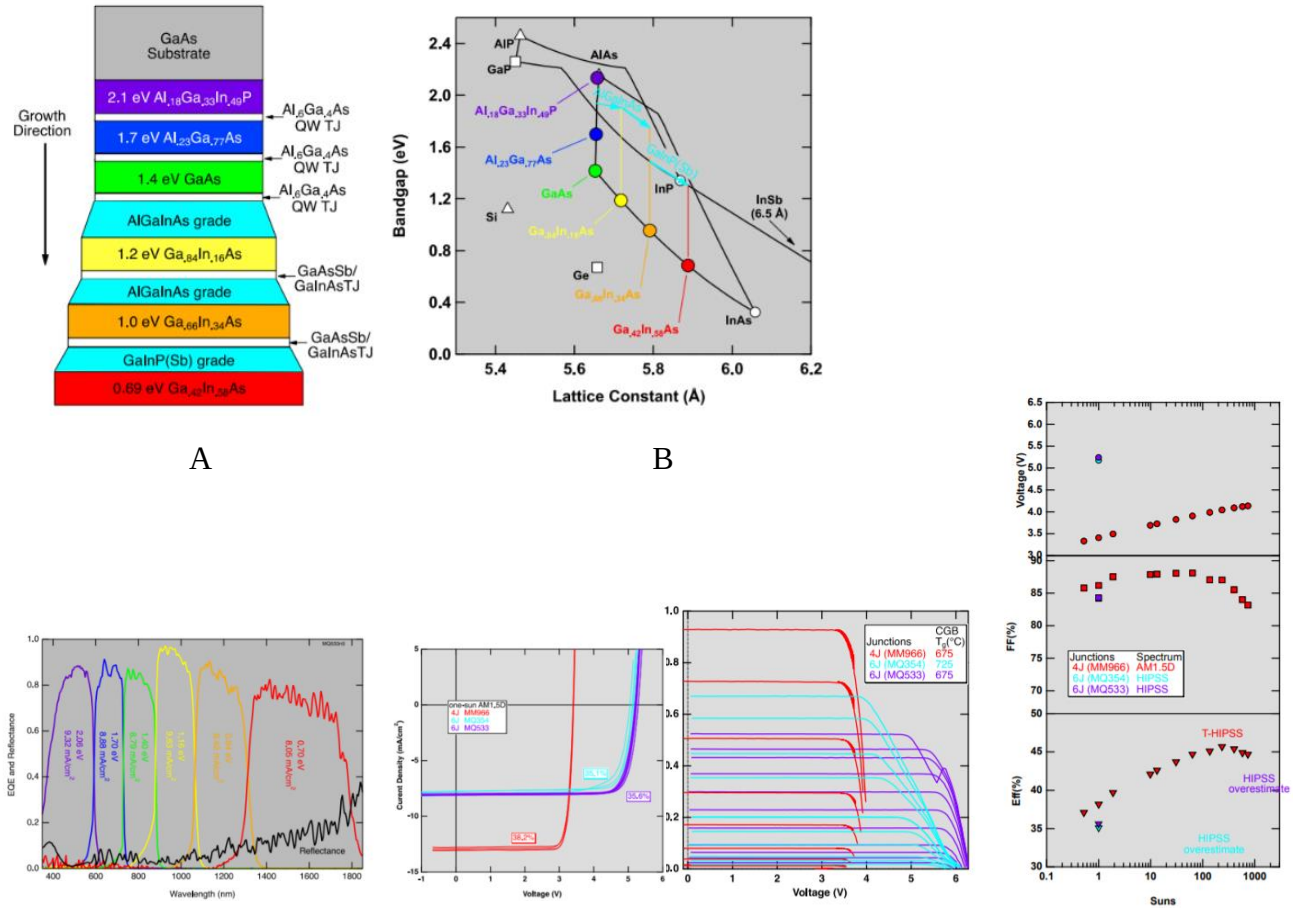

Figure 49: A) Schematic of a six-junction inverted metamorphic solar cell.

B) Diagram of bandgaps vs. lattice constant.

C) Its external quantum efficiency and reflectance.

D) Comparison of one-sun AM1.5D JV curves of 4J and 6J devices.

E) Comparison of JV curves of 4J and 6J devices under high intensity illumination.

F) Voltage, fill factor, and nominal efficiency as a function of concentration.

(J. F. Geisz et al., 2018)

Figure showed 6J IMM concentrator solar cell with 35.8% efficiency, V_{OC} = 5.301 V, J_{sc} = 8.05 mA/cm^2, FF = 83.9% at one-sun. However, in figure F, the lighter blue

markers for the 6J HIPSS indicate a systematic error from the uncontrolled spectrum that the high-concentration performance of 6J IMM measurement under the AM1.5D spectrum cannot be obtained. The study has demonstrated this is because of limiting resistance of internal resistive barrier caused by Zn diffusion during the thermal heat load of subsequent growth (three GaInAs metamorphic junctions in this 6J IMM device use Zn-doped GaInP BSF). Using C-doped arsenide BSFs instead of Zn-doped phosphide BSFs and lowering CGB growth temperatures can reduce this problem. After the change, the calculated result was approximately 43% efficiency at 200 sun concentration (J. F. Geisz et al., 2018). There is also suggested that to achieve 50 percent efficiency with the same junction quality shown in this 6J IMM concentrator solar cell, more reduction in series resistance, photocurrent improvement, and optimization are needed. (J. F. Geisz et al., 2018).

4.6 Quantum dot solar cells

In current years, quantum dot solar cells (QDSCs) have experienced continuous development, presenting a 16.6% efficiency now (N. R. E. Laboratory, 2020). Quantum dots (QDs) are a unique class of semiconductors consisting of II-VI, III-V, or IV-VI periodic group elements that are nanocrystals (approximately 2–10 nanometer in diameter) and can confine electrons (quantum confinement) (US National Renewable Energy Laboratory, 2013). Their strong advantage can solve a big challenge in the conventional bulk microstructures of single junction solar cells. In a regular device, photons with energies smaller than semiconductor bandgap are not collected. In contrast, those with energies much greater than it produce hot-carries, and the excess energy is lost as heat upon cooling down. QDs with tunable bandgap in various sizes and intermediate band formation ability to match the board solar spectrum distribution becomes a solution against the excess energy leakage of photons. QDs can be molded into different forms in two-dimensional or three-dimensional arrays, unlike conventional crystalline or amorphous semiconductors. They are easily manufactured to create junctions on cheap substrates like plastics, metal sheets, or glass. They also match very well with organic polymers and dyes (Jasim, 2015). There are different configurations of QDSCs: quantum dot sensitized SCs, colloidal nanocrystal quantum dot SCs, quantum dot organic bulk hetero-junction SCs, quantum dot bulk nano-hetero-junction SCs, metal oxide/quantum dot bilayer hetero-junction SCs (J. Ajayan et al., 2020).

Methods to manufacture or synthesize quantum dots are classified as bottom-up (assembling atoms to make into the desired nanostructures) or top-down (carving large substance pieces into the desired nanostructures) techniques. Some of them are suitable for solar cell production, such as electron-beam lithography, self-assembly growth, organometallic or colloidal (wet chemistry) synthesis. Electron-beam lithography is a top-down method. The electron beam device is set up to etch well-defined patterns on a bulk semiconductor and or superlattice. Then a semiconductor layer is cultivated in micro-technology following a planned protocol (Jasim, 2015).

Self-assembly growth techniques (bottom-up strategy) include molecular beam epitaxy (MBE) and metal organic chemical vapor deposition (MOCVD) are commonly used in

growing superlattices with various materials with distinct lattice constants. A semiconducting compound with a lower lattice constant is deposited atoms on a larger lattice constant compound surface (for example, InAs quantum dots on GaAs/ InGaP materials are always done by MBE system) (David M Tex et al., 2014). Relaxation of the cultivated layer after certain growth thickness caused by lattice mismatch leads to the nucleation of quantum well islands of random shape and controllable size. High vacuum and temperature are needed in this approach. Despite being an expensive, sophisticated, and long process, the MBE can control strictly and precisely the growth of quantum dots and their layers. In contrast to MBE, MOCVD is used in the mass fabrication of sample wafers, and the crystal growth is made by chemical reactions, not by physical deposition (Jasim, 2015).

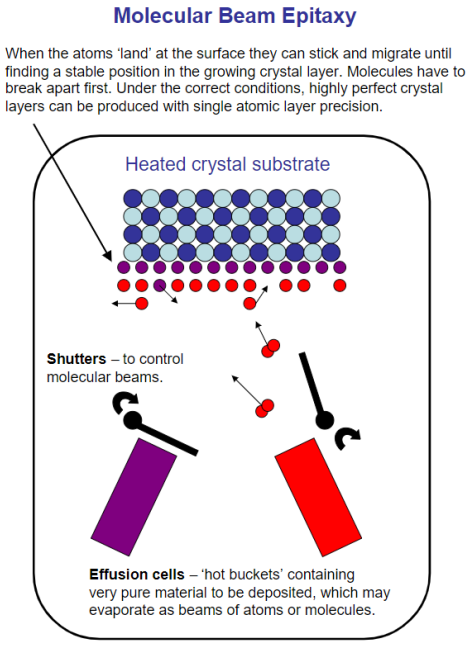

Figure 50: Illustration of a Molecular Beam Epitaxy system (Bell, n.d.).

Using the same bottom-up technique as self-assembly growth, but organometallic or colloidal (wet chemistry) synthesis is a cost-saving and fast-growing method to synthesize quantum dots in large quantities once. At proper laboratory and non-harsh conditions, wet-chemical synthesis routes deal with chemical reactions in the solution phase using precursors. There is no general rule for these types of synthesis approaches since each method of wet-chemical synthesis varies from the others (Y. B. Pottathara, 2019). For example, to synthesize colloidal lead sulfide PbS nanoparticles, 220g PbO, 0.25ml oleic acid $C_{18}H_{34}O_2$, and 9.75ml 1-octadecene (ODE) are heated together in a flask at about 150°C for 1 hour under N_2 flow to form lead oleate, and by-product evaporated water. Then cool to 90-100 °C, quickly inject 0.5 mmol $(TMS)_2S$ dissolved in ODE into the reaction flask. After being formed and cooled again with an ice bath. Synthesized PbS quantum dots can be encased colloids in a shell for protection, alter the charge, manipulate functionality, enhance stability, and surface reactivity. The precipitate (for ex. the mixture of methanol/butanol), resuspend, and centrifuge are in nonpolar solvents (for ex. tetrachloroethylene, toluene, or hexanes) (Jasim, 2015).

$$PbO + 2C_{18}H_{34}O_2 \xrightarrow{N_2, ODE, 150°C} Pb_{oleate} + H_2O \uparrow$$

$$Pb_{oleate} + (TMS)_2S \xrightarrow{N_2, ODE, 90-100°C} PbS_{nanoparticles}$$

There are some disadvantages in QDSCS. Heavy metal (like Pb, Ca) based quantum dot solar cells are extremely toxic by nature and require a very stable polymer shell. Lead can cause serious brain and kidney damage and eventually death (Mikhail Boldyrev et al., 2018). Cadmium and selenium ions used in the core of quantum dots are considered cytotoxic. Quantum dot metabolism and decay within the human body are still largely unexplained, and experiments have shown that quantum dots can accumulate in the spleen, liver, and kidney (Calderone, 2018). Thus recently, the concept of 'greener' QDSCs is gaining a lot of attention. CZTS (Cu_2ZnSnS_4) nanoparticle QDSCs have been developed to be promising low-cost processed, non-toxic and environment friendly devices (Sonali Das et al., 2020). The study of Los Alamos researchers in 2020 has shown that the Zn:$CuInSe_2$ QDs devices acquired a prominent defect tolerance, highly reproducible PCE of 10% and are free of any toxic elements. The team used a copper, indium, and selenium reaction to produce zinc-doped quantum dots with zinc. The dots were then integrated into the voids of an extremely porous titanium film that acted as a charge collecting electrode (Victor I. Klimov et al., 2020).

One major factor limiting the performance of TiO2/PbS colloidal quantum dot (QD) heterojunction solar cells is the energy loss due to carrier recombination. Zhenhua Sun et al. have proved that the charge recombination of these QDSCs can be decreased, and carrier lifetime can be increased by adopting non-toxic Zn-doped $CuInS_2$ (Zn-CIS) QDs into the PbS QD matrix. Enhancement in carrier lifetime also leads to the improvement of the charge transport properties, which results in boosting PCE (Zhenhua Sun et al., 2015).

Currently the performance of quantum dot sensitized solar cells (DSSCs) has been over 13%, which is in the same range of DSSCs (Zhenxiao Pan et al., 2019), (Huashang Rao et al., 2020). There are two challenges QDSSCs facing, which are QD loading, long term stability. In DSSCs, a part of the dye is replaced by QD materials to become QDSSCs, causing the experimental possibility distortion. Colloidal QDs (made from PbSe, PbS, CdS or CdSe) can constrain the QD loading with long molecular capping present same sizes as regular nanostructured electrode pores, hence light harvesting can carry out (Mora-Seró, 2020). On the other side, most QDs are unstable in iodine/iodine electrolytes, and new redox systems are necessary, requiring a new suitable counted electrode at the same time. In short, concerning DSSCs, the structure of QDSSCs should be reexamined to improve efficiency and stability (I. M.-Seró, J. Bisquert, 2010). Previous studies have demonstrated that polysulfide redox offers longer stability for semiconductors in liquid electrolytes (G. Hodes et al., 1981) and has recently become the most common redox mechanism used in QDSSCs (W. Wang et el., 2020). Nevertheless, the widely used colloidal lead sulfide PbS QDs suffer from difficult synthesis consisting of high-temperature, toxic organic solvents, and a protective environment (X. Mao et al., 2020). Using 1T-MoS_2 as composite counter electrode material also significantly improves the charge transfer, electron lifetime, charge separation and thus the CdS/CdSe/ZnSe QDSSCs efficiency (Z. Tian et al., 2020).

Another potential alternative is all-solid-state QDSSCs due to their ability to solve package problems and low stability in the long term. However, in this situation, the PCE is limited because only electrodes with thickness less than 2μm can prevent hole transport losses in the solid HTM, which is too thin compared with mesoporous photoanodes of a thickness of approximately 30 μm used in liquid QDSSCs (W. Wang et el., 2020). All-solid nanoscale $MAPbI_xBr_{3-x}$ perovskite QDSSCs using spiro-OMeTAD as HTM could present both advantages of relatively high PCE and good stability (Dr. So-Min Yoo et al., 2020).

Besides, the addition of methanol, accounting for 30% of polysulfide electrolyte, can enhance the stability of PbS QDSSCs (J. Tian et al., 2016). In figure A It is obvious that the loading of PbS QDs boosts both the absorbance and the absorption spectrum of the TiO2 film. Moreover, film absorption increases with a rise in concentration and peaks at a concentration of 0.06 M, then decreases. Figure B showed that Jsc, Voc is noticeably enhanced by the addition of methanol to the electrolyte, which is the critical source of improved conversion efficiency. The extraordinary rise from Jsc can be due to the improvement of the stability of PbS, the transfer, and the electron's lifetime. Therefore, the methanol added solar cell's PCE is 66% significantly higher than the one generated without methanol (2.41 %). Also, methanol in the electrolyte has increased the QDSSC stability as in Figure C (J. Tian et al., 2016).

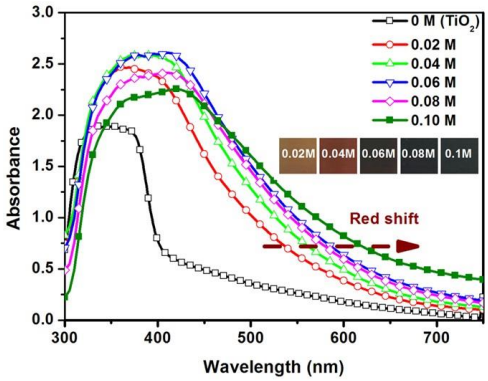

A

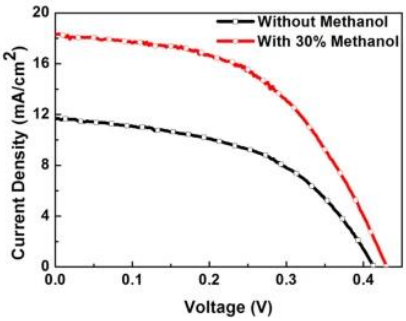

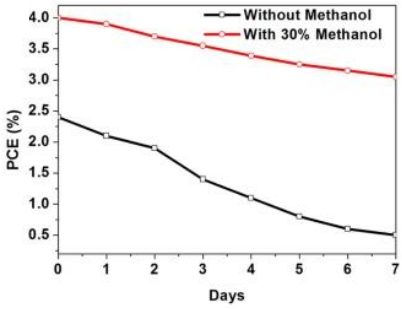

B C

Figure 51: A) UV-visible spectra curves of TiO2 film/TiO2 film filled with PbS QDs from precursor solutions with different concentrations; inset indicates the hue of the film.

B) J-V curves of QDSCs with/without methol measured under AM 1.5 G, at 1 sun.

C) Power conversion efficiency (PCE) of the QDSCs with/without methol after several days when the enclosed cells were exposed to air at 24 °C (J. Tian et al., 2016).

In another study, Taylor Moot et al. found out that the degradation mechanism of CsPbI3 nanocrystal (NC) films is unique from, and 2 orders of magnitude slower than, their polycrystalline thin-film counterparts. Under specific conditions, CsPbI3 NC films show a compositional instability instead of the phase instability seen in large grain CsPbI3. They indicated that controlling $CsPbI_3$ nanocrystal films' surface chemistry is the key factor to improve stability against ambient reactive oxygen species. Their controlling strategies, including minimizing the number of surface defects, encapsulation with an oxygen scavenging layer, using an alkylammonium bromide ligand surface treatment, are proven to increase the longevity of nanocrystalline film, and inhibit various steps in the photo-oxidation degradation reaction (T. Moot et al., 2020).

5. Photovoltaic solar cells and modules growth sustainability challenges

5.1 Materials availability

One clear point is that if the future of PV solar cell is primarily based on glass encapsulated silicon solar cells, there will be no shortage of silicon as it is the world's second most abundant material in the crust of the Earth. The only problem is that to refine it to the high purity and crystallinity sufficient for a solar cell requires a tremendous energy amount. Originally, this technology was powered by hydroelectric power. Unfortunately, there is not enough hydroelectricity to sustain the development we are seeing, so instead, unclean fuel energy is now being used more and more in the silicon filtration process. However, the returned energy produced from the PV plan is 10-30 times greater than the energy expended in the processing of Si PV (V. M. Fthenakis et al., 2018), meaning the process is sustainable in terms of energy. Logistics and financing are the remaining concerns; while raw materials are plentiful, all-silicon and glass factories need to be prepared in advance as it takes at least three years to complete such massive plants. Global flat glass demand is forecast to grow 4.1% annually to 11.9 billion square meters by 2023 (Freedonia, 2020).

There are concerns that the scarcity of certain materials could limit PV thin films' growth. Gallium, indium, tellurium, and cadmium (Ga, In, Te, Ca), used in CIGS and CdTe solar cells, were identified in EU as crucial in terms of the extent of supply risk and economic value (European Commission, 2014). These materials have limited supply because they are minor by-products of zinc (Zn), copper (Cu), aluminum (Al), and lead (Pb) processing (Te from Cu or Pb, In and Cd and Ga from Zn, Ga from Al); thus, their production is inherently related to base metals production and not to mention the energy to extract these components can cause an extra constraint. Their usage is now expanding as the widespread growth rate of the entire PV industry is observed.

Therefore, it is essential to verify the pace at which such base metals are manufactured. According to many global market studies, demand for copper is expected to increase by as much as 50% over the next 20 years (Alliance, 2020). The total supply of zinc is forecasted to reaches a maximum in 2050 and lead in 2030 (H. U. Sverdrup et al., 2019). Afterward, these resources demand is projected to gradually go down or remain steady throughout the rest of the 21st century, as the recycling part will become more critical than ever.

Tellurium (Te), with an excess of around 1 μg/kg, it is one of the rarest stable solid elements, equivalent to that of platinum (Robert U. Ayres, Leslie Ayres, 2002). The supply of Te could be a restricting step to upgrade the CdTe solar cell technology to potential terawatt sizes due to its shortage. Primary sources of tellurium are from the anode slimes of smelted copper's electrolytic refinement, and their recovery rate on average is around 40%, which is just as half as copper recovery rate from its ores (V. M. Fthenakis et al., 2018) and not sufficient to meet tellurium increased demand. New copper recovery processes, rather than traditional electrolytic refining, are being investigated, but until now, these methods attempt fail to recover tellurium. Consequently, it is critical to consider alternate sources for this aspect. Solar cell recycling may help; end-of-life CdTe modules comprise up to 500 ppm Te (V. M. Fthenakis et al., 2018). At Brookhaven National Laboratory (BNL), laboratory and pilot-scale studies of Fthenakis and Wang obtained 99.99% separation of tellurium and cadmium from end-of-life devices with an estimated cost is US $ 0.02/Wp. First Solar has reported an overall recovery rate of 90% on an industrial scale. In case economic incentives or handling laws are provided, it can be expected that the collection of used modules will be 100% from vast utility installations and 80% from residential installations (V. M. Fthenakis et al., 2018). However, tellurium-rich modules have long lifetimes and have not been broadly reused to date nowadays, but optimistically before the middle of this century the role of recycling can turn into a massive source of secondary tellurium.

Indium (In) is a by-product of zinc extraction. The volume of indium depends on the zinc mining size and certainly remains tied in the future. Globally, only less than 5% of indium is used in thin-film CIGS PVs, and 65% accounts for fabricating indium tin oxide (ITO) used as LCD transparent conductive layers (Grand view research, 2017). Nowadays, the growing use of smart devices has led to higher demand for LCDs, resulting in intense competition in sourcing indium supply. This competing situation may result in scarcity of high-purity indium, creating challenges in manufacturing to the thin-film solar cell industry. European Commission 2016 study on resistance to material supply bottlenecks in low-carbon energy and transport concluded that indium's significant supply threats can actualize by 2030 without mitigating steps (D. T. Blagoeva et al., 2016). Therefore, as same as tellurium, the critical future solution could be recycling indium from LCD screen-containing electrical and electronic equipment waste and used CIGS devices. Besides, in recent years, there have been other substitution alternatives for indium tin oxide (ITO) researched such as graphene, silver nanowire, carbon nanotubes, PEDOT, metal mesh (Ghaffarzadeh, 2018). Although these materials still need to be improved in performance and remain subscale in the market, their substitution potential promises to give room for CIGS technology to have an adequate supply of indium in the future.

Gallium (Ga) is found in trace amounts in the ores of other metals. It is mostly the by-product of bauxite ore processing to extract aluminum, and minor is from zinc purification residues. As a result, its output is relied on the production of these primary metals. Although the world's bauxite reserve base is so huge (estimated to be over 1 million tons), only around 10% of the gallium in bauxite and zinc resources can be economically extracted (U.S. Geological Survey, 2021). It is forecasted that the gallium in the reserve base will be scarce in the short term (U.S. Geological Survey, 2021). The production of gallium in 2019 was 351 tons and estimated to be 300 ton in 2020 (U.S. Geological Survey, 2021). Gallium is mostly used in the forms of gallium arsenide (GaAs) and gallium nitride (GaN). In 2020, global consumption volume of GaAs wafer was raised by 14%, of which dominating markets were Asian countries and the Pacific. GaAs wafer is principally used in integrated circuits or ICs and optoelectronic devices such as solar cells, light-emitting diodes (LEDs), radio frequency (RF), photodetectors, laser diodes. However, the GaAs based photonics applications share smaller portion (approximately 20%) in the market than LED and RF devices (accounting for 48%, 32% respectively) of which usages all show upward trends. To solve the problem of high resource demands in which photovoltaic devices production is also affected, substitutes are necessary. In certain specific-wavelength applications, helium-neon lasers can replace GaAs in visible laser diode applications, and indium phosphide components have the potential to compete GaAs-based infrared laser diodes. In visual displays, organic liquid crystals are used to substitute LEDs. In heterojunction bipolar transistors of some RF technology applications, silicon-germanium competes with GaAs. (U.S. Geological Survey, 2021).

For better insights and to assess future PV materials demand between now and 2050, the Joint Research Centre of the European Commission (JRC) has provided an overview of current material intensities, highlighting the significant variability that some materials exhibit in prospects (table 1). These include primary structural materials used in the PV power plants like glass, aluminum, steel, concrete, copper, and plastic. Specific materials to produce solar cells listed are silicon, cadmium, tellurium, gallium, indium, silver, copper, selenium, and germanium. It should be noted that the current materials intensities vary in a range of values due to the diverse solar panel composition among manufacturers, especially for CIGS and CdTe; thus, the intensities data by JRC are aggregated in general. Besides, the materials intensities have three different values correspond to optimistic (low demand scenario - LDS), neutral (medium demand scenario -MDS), and pessimistic (high demand scenario - HDS) intensity assumptions, respectively. All materials are expected to undergo substantial technical progress, leading to breakthroughs in conversion efficiency or the manufacturing process. As a result, the material intensity through the years will decrease dramatically (table 1).

Table 3: Material intensity estimates in 2018, 2030, 2050 for solar PV panels.

(S. Carrara et al. from JRC, 2020).

Technology	Material	Scenario	Unit	2018	2030	2050
All	Concrete	LDS	t/MW	60.7	56.2	48.6
All	Concrete	MDS	t/MW	60.7	58.4	54.6
All	Concrete	HDS	t/MW	60.7	60.7	60.7
All	Steel	LDS	t/MW	67.9	62.8	54.3
All	Steel	MDS	t/MW	67.9	65.3	61.1
All	Steel	HDS	t/MW	67.9	67.9	67.9
All	Plastic	LDS	t/MW	8.6	7.9	6.9
All	Plastic	MDS	t/MW	8.6	8.3	7.7
All	Plastic	HDS	t/MW	8.6	8.6	8.6
All	Glass	LDS	t/MW	46.4	42.9	37.1
All	Glass	MDS	t/MW	46.4	44.7	41.8
All	Glass	HDS	t/MW	46.4	46.4	46.4
All	Al	LDS	t/MW	7.5	6.9	6.0
All	Al	MDS	t/MW	7.5	7.2	6.8
All	Al	HDS	t/MW	7.5	7.5	7.5
All	Cu	LDS	t/MW	4.6	4.3	3.7
All	Cu	MDS	t/MW	4.6	4.5	4.2
All	Cu	HDS	t/MW	4.6	4.6	4.6
c-Si	Si	LDS	t/MW	4.0	2.0	1.0
c-Si	Si	MDS	t/MW	4.0	2.75	2.0
c-Si	Si	HDS	t/MW	4.0	3.5	3.0
c-Si	Ag	LDS	t/GW	20.0	4.0	1.0
c-Si	Ag	MDS	t/GW	20.0	6.0	2.0
c-Si	Ag	HDS	t/GW	20.0	11.0	5.0
CdTe	Cd	LDS	t/GW	35.0	20.0	10.0
CdTe	Cd	MDS	t/GW	50.0	27.0	12.0
CdTe	Cd	HDS	t/GW	85.0	60.0	35.0
CdTe	Te	LDS	t/GW	35.0	20.0	11.0
CdTe	Te	MDS	t/GW	52.0	27.0	15.0
CdTe	Te	HDS	t/GW	95.0	70.0	40.0
CIGS	Cu	LDS	t/GW	20.0	12.5	6.0
CIGS	Cu	MDS	t/GW	22.0	15.0	10.5
CIGS	Cu	HDS	t/GW	24.0	17.5	15.0
CIGS	In	LDS	t/GW	10.0	8.0	5.0
CIGS	In	MDS	t/GW	15.0	10.0	6.0
CIGS	In	HDS	t/GW	27.0	17.0	10.0
CIGS	Ga	LDS	t/GW	3.0	2.0	1.0
CIGS	Ga	MDS	t/GW	4.0	2.5	1.5
CIGS	Ga	HDS	t/GW	7.0	4.5	2.5
CIGS	Se	LDS	t/GW	22.0	17.0	9.0
CIGS	Se	MDS	t/GW	35.0	20.0	12.0
CIGS	Se	HDS	t/GW	60.0	40.0	20.0
a-Si	Si	LDS	t/GW	150.0	75.0	40.0
a-Si	Si	MDS	t/GW	150.0	100.0	75.0
a-Si	Si	HDS	t/GW	150.0	130.0	110.0
a-Si	Ge	LDS	t/GW	48.0	22.0	10.0
a-Si	Ge	MDS	t/GW	48.0	27.0	15.0
a-Si	Ge	HDS	t/GW	48.0	32.0	20.0

Based on data of material intensity together with capacity, lifetime, market share analysis, JRC has presented future solar PV material demand scenarios (figure 6). Data for 2030 and 2050 are indicated as a scale factor of current demand. There are significant differences in the demand for specific materials between various scenarios in the fabrication of PV cells. In the LDS, material intensities may improve, resulting in a

net decrease in material demand. In the MDS, the balance between the material intensities and capacity deployment will result in a modest rise in demand ranging from 1.1 to 2.8 times for structural materials; for specific materials, demand will increase 3 times for germanium, 2.5 to 2.6 times for gallium and indium, 2.1 for selenium, and 1.5 for cadmium, silicon, and tellurium. Silver is seeing a minor decline in demand. In the HDS, the expected most demand in 2050 will be germanium, which might rise to 28 times compared to 2018 values. For indium, gallium, tellurium, cadmium, and selenium, the change in the demand will also be remarkable, increasing 11.9 to 13 times in 2050. An insignificant decrease is forecasted for silicon, which will be steady demand like in 2030. The desire for silver is continued to decline by half of the value in 2030 (figure 6).

Table 4: Annual global solar PV material demand in 2018 in t/year (left) and relative demand of global solar PV materials in 2030 and 2050 as a ratio of current demand (right) (S. Carrara et al. from JRC, 2020).

Concrete		6 071 429
Steel		6 785 714
Plastic		857 143
Glass		4 642 857
Ag		1 908
Al		750 000
Cd	LDS	83
Cd	MDS	118
Cd	HDS	201
Cu		464 329
Ga	LDS	6
Ga	MDS	8
Ga	HDS	14
Ge		15
In	LDS	19
In	MDS	29
In	HDS	53
Se	LDS	43
Se	MDS	68
Se	HDS	117
Si		381 585
Te	LDS	83
Te	MDS	123
Te	HDS	224

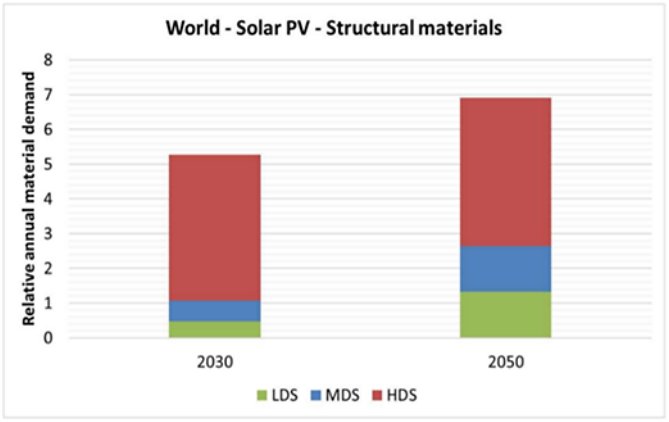

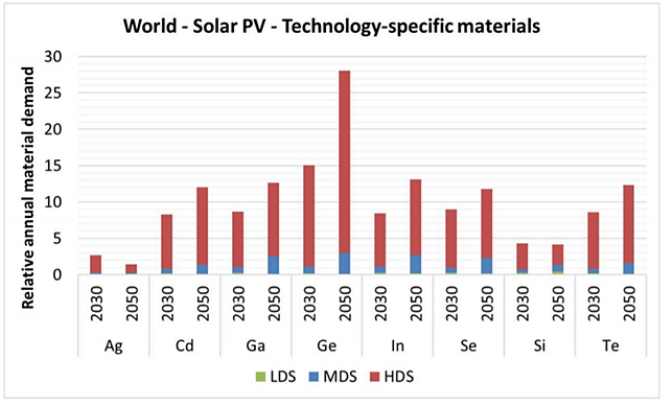

The predicted demands were also plotted as a proportion of the current worldwide supply (100% in figure 52) to assess the supply risks. In the comparison of solar PV demands with the overall supplies, the availability threshold is only exceeded by tellurium by 580% and germanium by 200% in the High Demand Scenario (HDS) in 2050, which indeed will limit the manufacture of CdTe, CIGS and MJSCs solar cells. Less severe risk but potentially threatening the supply chain are silicon, indium, and

selenium also in HDS (figure 52). The annual need for all structural materials is estimated to be in a safe zone in 2023 and 2050 as it is below the current availability (S. Carrara et al. from JRC, 2020).

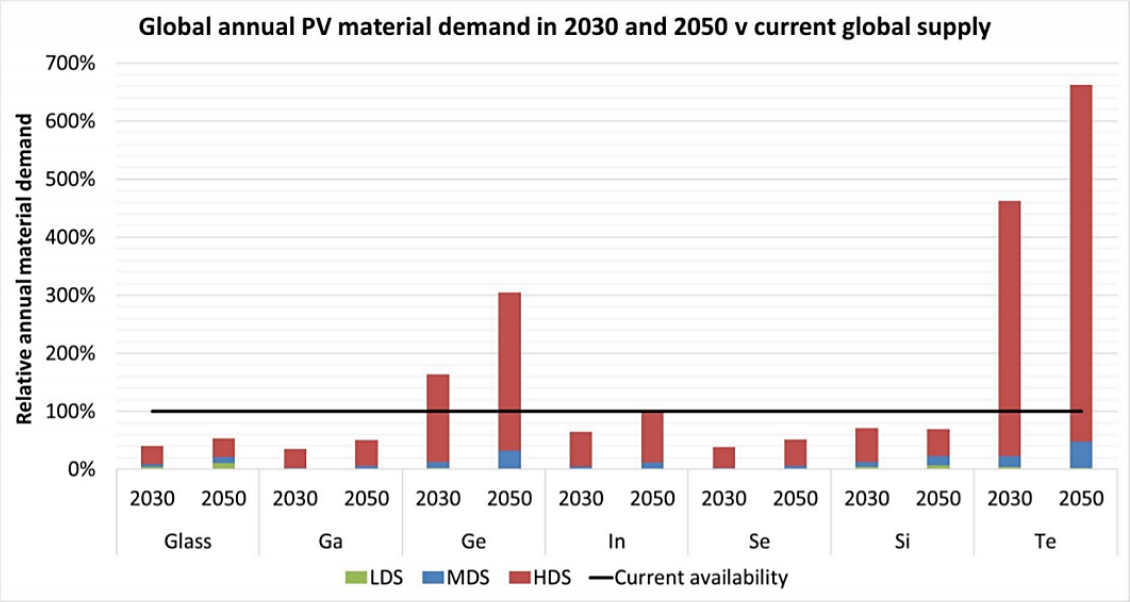

Figure 52: Global PV demand-to-global supply ratio in 2030 and 2050 – levels of demand close to current availability (S. Carrara et al. from JRC, 2020).

The vulnerabilities in future supply security for numerous elements might endanger the global transition to green energy technology. With the growth of PV deployment, it is again affirmed that recycling end-of-life PVs and recovering the valuable materials is becoming more crucial. It reduces material prices by providing considerable secondary resources at a lower cost than primary feedstocks. It replaces energy from material manufacture and alleviates worries about potential environmental contamination from uncontrolled PV disposal (V. M. Fthenakis et al., 2018).

5.2 PV Manufacturing's Environmental Health and Safety

PV technologies provide marked environmental advantages over traditional technologies in generating power: no noise, hazardous gas emissions, or greenhouse gas emissions. However, the production of solar cells still has environmental health and safety risks (EHS) like any other energy source, such as using toxic and flammable chemicals. Although the usage of those substances is less than many other industrial sectors in quantities, it still can pose environmental risks and occupational health (V. M. Fthenakis et al., 2018). Referred to the study of V. M. Fthenakis, EHS problems related

to the production of currently commercialized available solar cells are summarized in the following table:

Table 5: Occupation health, public health, and environment risks of different solar cells (V. M. Fthenakis et al., 2018).

Solar cell type	Occupational health risks	Public health and environmental risks
Crystalline Silicon (c-Si) Solar Cell	• Potential chemical burns and fumes inhalation from hydrofluoric acid (HF), alkalis (NaOH), and nitric acid (HNO_3) utilized in wafer cleaning, reactor cleaning, and removing dopant oxides. • Hazardous dopant gases and vapors (e.g., $POCl_3$) if inhaled. • Toxic P_2O_5 and Cl_2 gaseous effluents created by $POCl_3$ in a deposition chamber. Nowadays, inhalation dangers are minimized in the process stations thanks to well-designed ventilation systems.	• The c-Si PV technology has not been linked to any public health concerns up to now. • Environmental concerns about the formation of liquid and solid wastes during wafer slicing, cleaning, etching, and during solar cell manufacturing and assembly. • Concerns about the leaching of lead (Pb) in the used PV modules in the landfill. Industry-scale programs in minimizing caustic waste in etching and using environment-friendly alternatives for solvents, slurries, and solders have been achieved. Recycling stainless steel cutting wires, recovering SiC in the slurry, and in-house neutralization of alkali and acid solutions are also applied effectively. Pb-free soldering technology has now been widely implemented in more than 60% of manufacturers in 2016.
Amorphous Silicon (α-Si) Solar Cells	• The use of extremely pyrophoric SiH_4 gas is hazardous without proper handling. Depending on the carrier gas, the lower limit for SiH_4 spontaneous ignition in air ranges of 2 - 3 %. At the concentration of $SiH_4 < 2\%$, a pyrophoric concentration may also occur locally if mixing is insufficient. The mixtures can be metastable and ignited after a specific delay at silane concentrations $\geq 4.5\%$. The venting will be ineffective in protecting in this situation. • Hydrogen used in a-Si fabrication is combustible and explosive. • Toxic doping gases (such as PH_3, AsH_3) are adopted in insignificant quantities, so there is no sign of endangered public health or the environment. However, it should still be noted that leakage of these gases can pose an occupational risk. PV manufacturers have utilized complicated gas handling systems with enough safety features to reduce the risk of fire and explosion. Moreover, to avoid regular gas cylinders replacement, hydrogen and silane are stored in bulk from the tube trailers. Using a skid	• Without suitable separation zones , silane utilized in bulk amounts in a-Si producing factories may constitute a risk to the local community. Therefore, guideline for minimum distances to public places is compulsory; for example, the range is from 80 to 450 ft depending on the quantity and pressure of silane in containers in the USA.

	installed single cylinder of 450 l that can hold up to 150 kg (mini-bulk) of silane is another possibility. Bulk storage reduces the accident risk since trailer swaps are rare, well-planned special occasions in a precise and controlled management, under the supervision of different departments. However, the repercussions can be far more severe than those associated with gas cylinders if an accident occurs.	
Copper Indium Gallium Selenide (CIGS) Solar Cells	• The toxicity of Cu, In, Ga, and Se is mild. • Hydrogen selenide (H_2Se) gas used in the CIGS producing process is highly toxic. To avoid risks from H_2Se, the deposition system should be encompassed under negative pressure and discharged through an emergency control scrubber. The same preparation also applies to the H_2Se cylinder gas cabinets (V.M. Fthenakis, P.D. Moskowitz et al., 1995). Caution and various levels of control (engineering controls, personal protection equipment, and work procedures) must be applied to prevent employee exposure.	• The employment of hydrogen selenide as the primary feedstock in facilities may pose public health risks. These hazards can be reduced by adopting safer alternatives, reducing inventories, utilize flow restricting valves. Wet or dry scrubbing is used to conduct H2Se emissions from process tools. Emergency scrubbers should be installed to control unintentional leaks of this gas.
Cadmium Telluride (CdTe) Solar Cells	• The main concerns are related to the toxicity of the feedstock materials (such as CdS, CdTe, CdCl2). The occupational health risks posed by Cd and Te compounds in various processing stages vary depending on the compound's toxicity, physical state, and type of exposure. Cadmium, one of the CdTe precursors, is a very toxic substance. Cancer and targets to the body's cardiovascular, reproductive, gastrointestinal, neurological, renal, respiratory systems, and mortality are among the acute health impacts of Cd inhalation (United States Department of Labor, n.d.). Processes that consume or fabricate Cd compounds into fine particles or fumes pose greater health risks. Workers may be exposed to hazards during feedstock preparation, fume/vapor leaks, etching of surplus materials from panels, maintenance activities, and trash handling. Caution and various levels of control must be applied to prevent employee exposure.	• There are no public health risks detected. • Environmental concerns arise from the disposal of production waste and end-of-life CdTe modules, which are described further in the recycling section.
GaAs	• Arsenic is particularly toxic. • GaAs are widely suspected to be carcinogenic to humans (N. K. Foley et al., December 2017).	• Normal operating conditions in industrial facilities show no pose to human health or the environment.

	• MOCVD process to produce III/V PV cells uses the highly toxic hydride gases, phosphine, and arsine, as feedstocks. Safety hydride handling also necessitates multiple levels of engineering and administrative safeguards. Alternatives are necessary since the use of the hydrides in MOCVD is highly ineffective nowadays. Tertiary butyl arsine (TBAs) and tertiary butyl phosphine (TBP) can be potential substitutions to test.	

5.3 Production cost

The current PV situation still shows the market dominance of silicon-based solar cells due to their efficiencies and costs. III-V solar cells have obtained the best efficiency among other solar cells, which made them widely employed in space applications, unmanned area vehicle. However, III-V solar cells are two to three orders of magnitude more expensive than other technologies, and lack a low-cost, high-quality production procedure, relegating them from mainstream terrestrial PV markets. Depending on the cell type, production volume, and process assumptions, present III-V manufacturing costs range from \$40/ W_{DC} to more than \$100/ W_{DC}, with minimum sustainable prices ranging from \$70/ W_{DC} to more than \$170/ W_{DC}. III-V solar module costs frequently approach \$150/W, which is about 400 times more than the current prices for mainstream c-Si and CdTe modules (\$0.30–\$0.50/W) (K. A. W. Horowitz et al., 2018). A study of the US National Renewable Energy Laboratory has indicated a pathway to decrease III-V solar cell manufacturing costs from levels of above \$50/W to below \$0.50/W. Attaining such that cost savings would need substantial R&D as well as a production scaleup.

A cost of \$2/W may be possible in the near term if enhanced substrate reuse can be implemented with high productivity and low polishing or reclamation costs, and commercial dynamic hydride vapor phase epitaxy (D-HVPE) can be shown and scaled up. D-HVPE is a variant on HVPE, previously utilized for growing semiconductor III-V materials, where the reaction chambers are spatially separated, allowing the production of high epitaxial growth quality at high throughput (K. A. W. Horowitz et al., 2018). D-HVPE technique allows for the formation of atomically and chemically abrupt heterointerfaces at a steady state while maintaining very high deposition rates (54µm/hour for GaInP and 195µm/hour for GaAs and —for two-junction solar cells in a laboratory scaled pseudo-in-line reactor) (J. Simon et al., 2019), (K. L. Schulte et al., 2017), (J. Simon et al., 2016). It also takes advantage of the low-cost source materials (elemental metals such as Ga, In) instead of highly engineered trimethyl precursors (K. A. W. Horowitz et al., 2018). Moreover, D-HVPE's design of in-line deposition method opens the pathway to throughput enhancement and corresponding cost reductions, comparable to how in-line deposition techniques currently enable low-cost production

of thin-film PV devices (figure 8) (J. Simon et al., 2019). Even though a cost of $2/W is still higher than the costs of mainstream PV solar cells, it may be adequate for specialty markets, such as outdoor recreation applications, portable power for military, electric vehicles, and some portable small solar systems in developing countries. This would also result in a considerable cost decrease for III-V technologies in markets where they are now deployed (K. A. W. Horowitz et al., 2018).

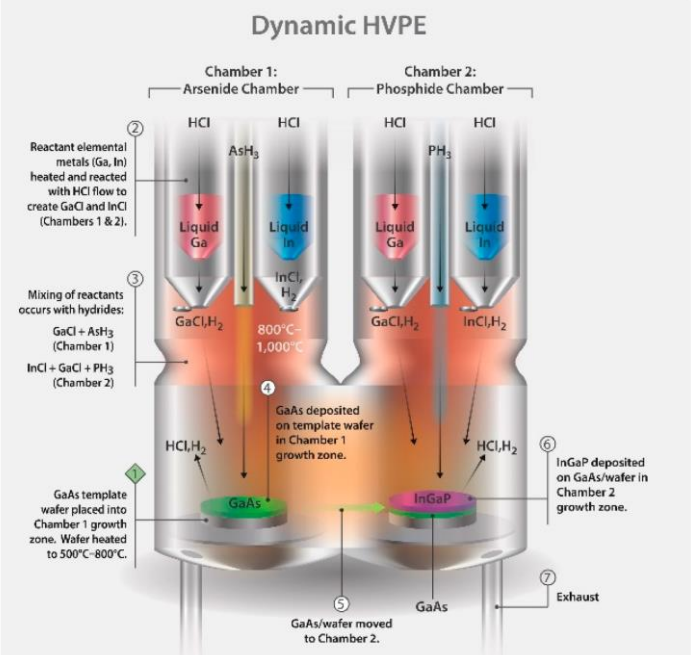

Figure 53: The schematical two-chamber D-HVPE reactor at NREL with parallel steady-state processes for GaAs and GaInP (J. Simon et al., 2019).

To reach costs less than $0.50/W, either a considerable increase in the substrate reuses quantity over the existing state-of-the-art is required, or the adoption of a low-cost alternative substrate is necessary. Additional increases in manufacturing volume are also required. Costs of $0.40/W may be attainable if 8-inch (244cm^2 when cropped to a pseudo-square) substrates are employed. This scenario might allow III-Vs to compete in mainstream terrestrial PV industries due to the superior characteristics of III-V materials despite that $0.40/W is still higher than c-Si cell production costs ($0.15/W - $0.25/W). There are more pathways for further cost reduction that need additional research, such as flattening the cell layers, boosting manufacturing yield, boosting efficiency, and reducing metal consumption or utilizing alternative, cheaper metals. Besides, optimizing the D-HVPE equipment and process like belt speed and number of wafers in parallel might yield additional cost savings (K. A. W. Horowitz et al., 2018).

5.4 PV waste treatment - recycling end-of-life PV modules

As already mentioned, recycling end-of-life PV modules will be indispensable within 30 years when a significant amount of spent PV waste (from 45,000 tons in 2016) will be discharged at about 60 million tons by 2050 (P. Danz et al., 2019). The improper disposal of c-Si PV waste might result in environmental problems, one of which is the leaching of lead found within soldering paste and the ribbon coating to connect the cells. At about 576 mg per 1 kg of a panel, the lead level is below the disposal limits for a landfill but still exceeds the leaching limitations for inert waste disposal (Latunussa C. et al. , 2016). That will result in the economic loss of many valuable and reusable materials such as glass, aluminum, silver, silicon metal (BioIntelligence, 2011). The same scenario can also happen with CdTe and CGIS, as most commercialized PV cells are disposed of in municipal landfills. Without a control plan, Cd and Te may seep out of landfills and pollute soils, groundwater, and surface water, representing a major threat to terrestrial and aquatic ecosystems (A. M. Curtin et al., 2020). As a result, the deployment of recycling is vital to prevent these risks of environmental pollution and recover hazardous and valuable sources. It not only cuts down waste and waste-generated emissions but also helps reduce energy usage and emissions linked to the manufacture of virgin materials. It could be essential for high-impurity raw materials (such as semiconductor precursor materials), which frequently necessitate an energy-intensive pretreatment to obtain the appropriate purity levels. In addition, when materials are separated for recycling, hazardous and non-recyclable components need to be disposed of in controlled hazardous waste landfills rather than municipal landfills (A. M. Curtin et al., 2020).

Nowadays, crystalline silicon (c-Si) and thin-film modules (CdTe and CIGS) are the only two types of PV modules having commercialized recycling technologies with the two main objectives of removing the encapsulant from the laminated structure and recovering metals and other materials. However, each recycling process has different characteristics depending on the module structure, and the substances contained insides. In thin-film modules, the aim is to recover the cover and substrate glasses containing semiconductor layers by removing the encapsulant from their laminated structure. Whereas separating and recovering Si cells, glass, and other metals are the goals for c-Si modules (K. Komoto et al., 2018).

Recently, various research and development (R&D) efforts in c-Si PV modules recycling technologies have been suggested and implemented to meet current and future requirements, such as better recycling/recovering rates and limiting the environmental impacts. They are shown in figure 54 as different processes to recycle c-Si PV modules by thermal, mechanical, chemical, and combination approaches. The most difficult but critical step in the PV modules recycling process is eliminating the encapsulant from laminated structure to separate glass and other components and recover metals from electrodes and Si cells. For this reason, an effective way to remove the encapsulant easier, which is already widely used as the first step of PV recycling, is disassembling the metal frame and terminal box. The two next steps are to remove encapsulant from laminated structures and recover metals from the Si cell where thermal approaches,

mechanical approaches, chemical approaches can be applied (schematical diagram in figure 54) (K. Komoto et al., 2018).

The thermal approach can recover Si cells, glass, and electrode ribbons by the combustion process. One of the advantages of this technique is that it can retrieve glass and Si cells with no breakage under certain conditions and improved recovered value for recycling. The Si cell recovery rates without breakage are affected by cells or wafers thicknesses and burning circumstances. If the cells are thin, their recovery yield is indeed low. Furthermore, the cells will most likely be assigned as Si raw materials if they contain defects like micro-cracks or edge chipping rather than being recycled into a complete wafer. Another challenge of the thermal approach is the mass-treatment requirement to improve its efficiency and economy. Moreover, higher energy consumption is also a huge concern; thus, it is necessary to apply low-energy technologies, such as during the heat recovery stage (K. Komoto et al., 2018). In the other hand, it is vital to consider toxic gas generation countermeasures from burning the parts containing toxic materials. For instance, when burning a c-Si cell's back-sheet layer, typically hydrofluorocarbon polymers such as polyvinyl fluoride (PVF) or polyvinylidene fluoride (PVDF), generated fluorine gas and potential dioxins formation will represent a health danger if leaching into the atmosphere and contaminating soil and waterbodies. Moreover, the thermal treatment of fluoropolymers is challenging since they are hard to thermally degrade (carbon–fluorine bond at 490 kJ/mol) (R. Dams, K. Hintze, 2017). Thus, study about the fluorine release behavior from PVDF and PVF during the thermal decomposition is critical for developing a technically feasible end-of-life PV back-sheets treatment (P. Danz et al., 2019).

A mechanical process includes scribing glass, scribing non-glass layers, cutting the encapsulating layer, and crushing or grinding. Although this process cannot recycle Si cells into Si wafers, glass recovering without breakage can be done with the encapsulation layer cutting or non-glass layers scribing. Besides, the other two techniques can perform broken glass recovery. Those methods that do not have breakage are advanced for better-quality and high recovery-rate glass, which is possible for other materials also (K. Komoto et al., 2018).

Following the mechanical technologies are the chemical treatment steps to segregate Si chips and metal compounds from the remaining mixture. Chemical techniques such as etching with alkali hydroxide or acid can be used to recover metals from Si cells, and suitable waste treatment (such as hydrofluoric acid) is required. In addition, solvent treatments that remove the encapsulant from lamination structures, technically, can allow Si cells to recover. Such methods, on the other hand, necessitate extended treatment time as well as liquid waste treatment stages. Even if environmental issues are remedied, they may not be suited for mass treatment but only for small-scale one-site treatment. On the commercial scale, combinations between different recycling technologies are increasingly operated nowadays despite some disadvantages of each method. The combination of mechanical and chemical processes may need to speed up processing time and waste chemical treatment, whereas a mechanical process combining with a thermal technique consumes a lot of energy. (K. Komoto et al., 2018). Joint Research Centre (European Commission) has shown in their study that 1 ton of c-Si PV panel waste recovery approximately yields 686 kg of low iron scrap glass, 0.5 kg

of silver, 182.64 kg of aluminum scrap. The recovery rate of silicon metal is estimated to be 95%, copper is 96.5% (Latunussa C. et al. , 2016).

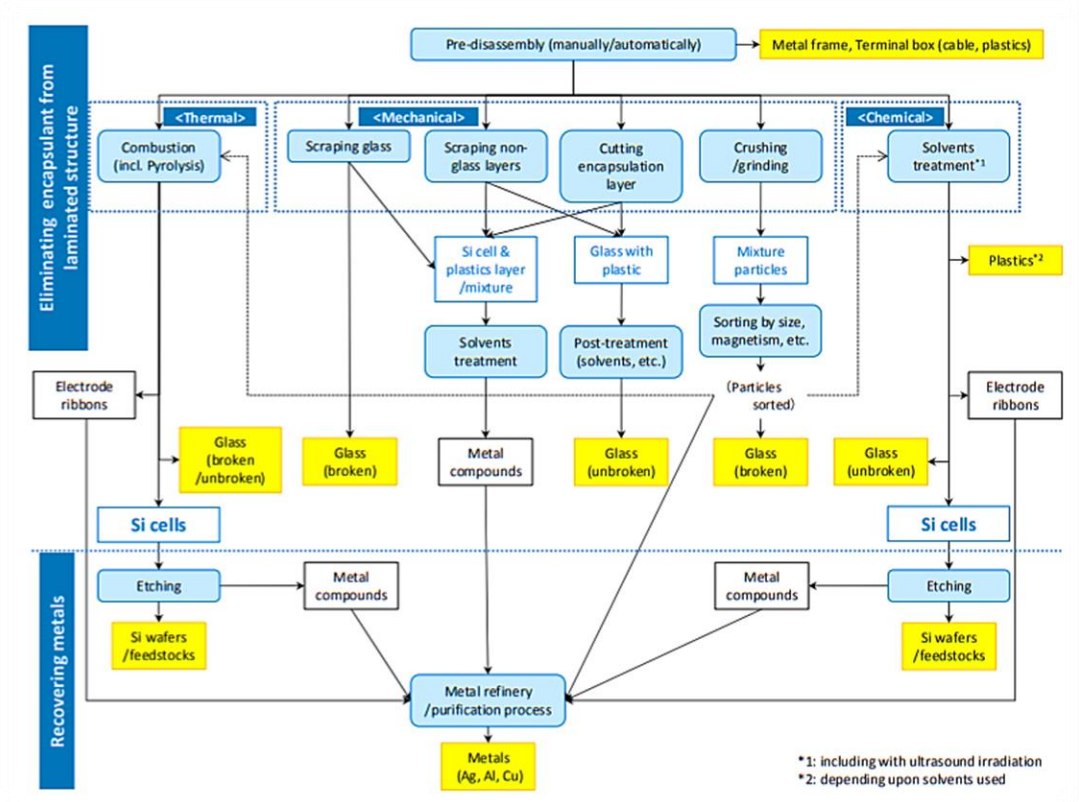

Figure 54: Different processes to recycle c-Si PV modules by thermal approach, mechanical approach, chemical approach and combination (K. Komoto et al., 2018).

Recycling thin-film PV modules can involve combustion as a thermal approach, crushing/grinding and cutting the encapsulation layer as mechanical approaches, and optical laser treatment (figure 55). The advantage of this combination is that the double-glass structures separation and cover glass recovery are without any contamination and damage. Substrate glass with compounds may be restored under certain circumstances while preserving its form. Crushing the substrate will also be an effective strategy when considering the treatment rate and yield during the metals recovery stage from substrates. Nevertheless, non-damaged glass and glass cullet components with a bigger particle size are preferred for their quality and potential to boost recovery/recycling rates. Chemical approaches may also be effective in recovering metals from substrates; however, waste liquids and exhaust gases generated by them are getting more concerns than their attraction if there is no thorough treating solution. Alternatively, mechanical scribing can be applied in the case of unbroken substrates during the recovery stage. Lastly, the existing technology scenario will only be able to meet the obligation for efficient end-of-life management if the amount of waste PVs is not excessive. PV recycling technologies, on the other hand, should be ready for mass-treatment of decommissioning PV modules (K. Komoto et al., 2018).

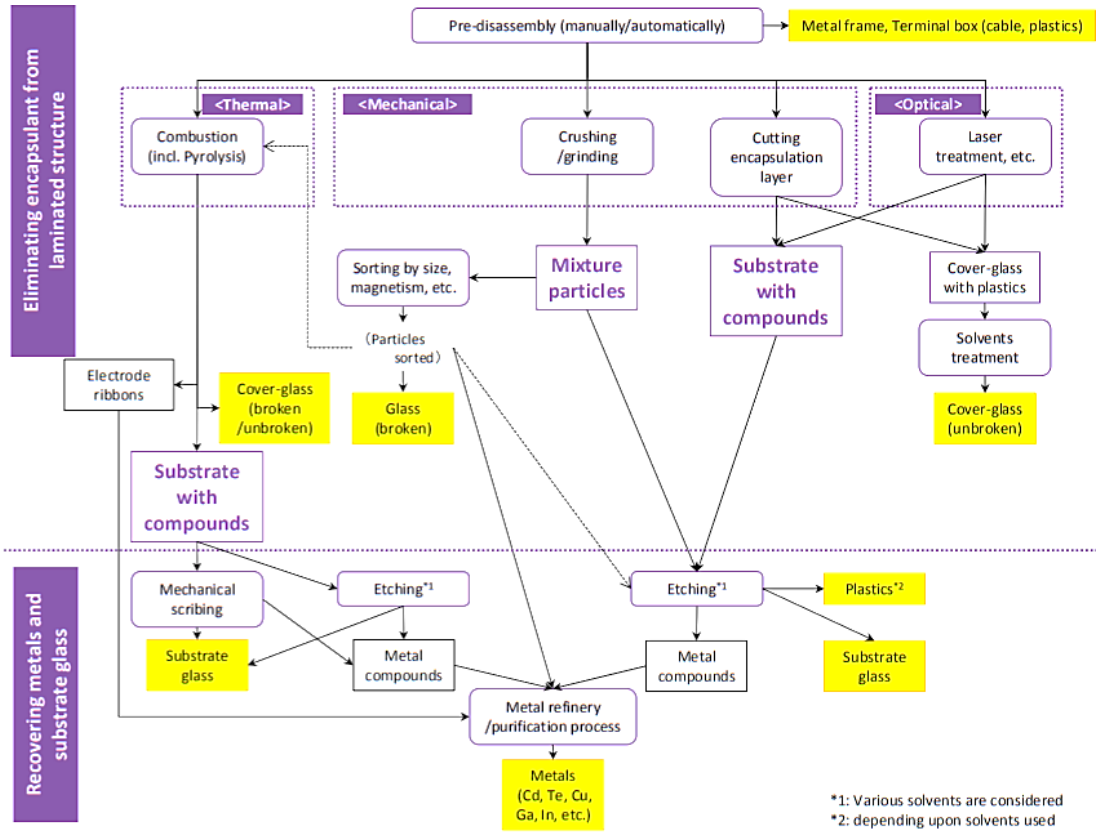

Figure 55: Different processes to recycle thin-film PV modules by thermal approach, mechanical approach, and optical approach (K. Komoto et al., 2018).

6. RESULTS

The thesis has provided a detailed overview of various concepts, materials, production, challenges, and possible solutions for the three generations of PV solar cells. The first generation - conventional crystalline silicon solar cells (mono- and multi-crystalline silicon), is the most dominant type in the global PV market nowadays thanks to its matured and well-established manufacturing technologies, low prices, and high efficiencies. C-Si solar cells have an elaborate fabrication process, especially in the making of silicon wafers. First, silica is heated in an arc furnace to become the metallurgical-grade state. It is then transformed into ultra-pure electronic-grade polycrystalline silicon by the Siemens or fluidized bed reactor method. In the next step, different widely used methods to grow wafer ingot from polycrystalline silicon can be applied such as Zochralski silicon (CZ-Si) (for mono-Si), Float-zone silicon (FZ-Si), Multi-crystalline silicon (mc-Si). The grown ingot typically has cylindrical or rectangular shaped and is add with dopants to become p-type or n-type. There are some challenges in these techniques necessitate further research for solutions. In CZ-Si, crystal growth is slow and energy-intensive, resulting in a high manufacturing cost (V. M. Fthenakis et al., 2018). Moreover, impurities might penetrate during the contact between the crucible and the melt. The obstacle in FZ-Si is the ingot's small diameter allowed to grow and the higher cost than CZ-Si method, limiting this method only common in the laboratory (A. HM Smets et al., 2016). While mc-Si block grown in its own method is more cost saving than mono-Si, the most evident blemish of mc-Si the

grain boundaries. The grain boundaries shorten the module material's minority carrier lifetime, decrease the performance of a solar cell. Mc-Si also contains brittle fracture, a higher measure of crystal imperfection and impurities, micro defects, and the possibility of cross-contamination for the crucible (V. M. Fthenakis et al., 2018). The silicon ingot is then sliced up into wafers and they will undergo a processing series of chemical, plasma, thermal, and laser treatment to become finished solar cells ready for the module installation. Even though silicon solar cells are reaching their intrinsic efficiency limits (32.33%) (W. Shockley, H. J. Queisser, 1961), there are still margins for improvement that will be utilized both in the lab and in industrial processes.

State-of-art c-Si PV cell structures are classified into PERC, Al-BSF, TOPCon, SHJ, and IBC. Leading the PV industry, the essential challenge of PERC cell is to continuously improve its efficiency and lower costs. Growing the tools throughput and automation are the key avenue for production cost reduction. In the aspect of performance enhancement, as output efficiency has hit 23.3% and the functional efficiency limit of this structure is about 24.5%, there are still rooms to improve the high ratio of minority carrier lifetime and wafer resistivity, rear contacts, contact tolerance for light-doped phosphorus emitters, boosting bifaciality - the ratio between the rear and front efficiency, and minimizing metal coverage (G. M Wilson et al., 2020).

Bifacial modules are the nowadays standard technology for ground-mounted systems. By lessening metal covering on the rear side, n-type TOPCon solar cells can become 80%-95% bifacial modules, p-type PERC can have 65–75% bifaciality. It is especially essential to prevent any module backside shading (J. S. Stein, 2019). Modeling the energy yield of bifacial PV modules is still under experimentation and improving PERC solar cells' bifaciality (G. M Wilson et al., 2020).

IBC solar cells have long been known to offer the best performance potential due to their ability to minimize shading losses. Their complex structure with contacts and doping of two polarities on one side requires at least three accurately aligned levels, resulting in high cost. For that reason, to compete with PERC solar cells in the market, IBC cells need to have a much higher efficiency than them. Applying passivating heterojunction contacts or polysilicon-based passivating contacts are excellent examples for improving cell performance (26.7%, 26.1%) (K. Yoshikawa et al., 2017), (F. Haase, 2018). Another pathway aiming at simplifying process complexity is also viable, for example, the usage of tunnel systems (A. Tomasi, 2017).

SHJ or HIT cells use passivating contacts based on an intrinsic layer stack and doped amorphous silicon, allowing them to have superior open-circuit voltage. Parasitic absorption of the front layer stack is the main issue of the amorphous silicon and can be solved by employing IBC or SHJ cell structures. Processes with a temperature higher than 200°C, except fired screen-printed metal contacts after the amorphous silicon substrate deposition are incapable in the SHJ cell. This challenge requires replacement routes by plated contacts or low-temperature pastes. Moreover, to obtain cost reduction, costly production tools, indium and silver use reduction should be considered carefully (G. M Wilson et al., 2020).

TOPCon solar cell is a young technology but has kept pace with the development of conventional silicon PV cells. With the advantages of being easily compatible with existing production lines, it only needs to follow an industry-standard procedure sequence for cost-cutting direction (G. M Wilson et al., 2020).

The second photovoltaics generation includes conventional thin-film PV cells such as thin-film silicon solar cells (thin-film amorphous silicon, thin-film microcrystalline silicon), Cadmium Telluride (CdTe), and Copper Indium Gallium Selenide (CIGS). They are the world's second most popular photovoltaic (PV) group. Their low cost of production appeals to manufacturers as they do not need semiconductor wafer substrates and their processing equipment requires lower process temperatures. Different types of thin-film PV technologies share many similar features: the ability to grown on foreign substrates (glass, polymers, metal), the use of TCO layer as front contact, fabrication in a “superstrate” / “substrate” (V. Avrutin et al., 2014).

Thin-film amorphous silicon (a-Si:H) solar cell has a network of silicon atoms distributed in random distances and angles. Its structure is a p-i-n junction to prevent poor carrier transport and limited minority carrier lifetime caused by dangling bonds and bond angle distortions. Currently, the recorded efficiency of single-junction a-Si solar cells has been 14% (N. R. E. Laboratory, 2020). Preventing its performance from being diminished by light-induced degradation effect after a short usage period is the biggest challenge of a-Si technology. A possible solution can be reducing the amorphous layer thickness and using optical confinement methods to exert front and back reflectors (V. Avrutin et al., 2014). However, single-junction (a-Si:H) cells have progressed to a mature stage where very little room is left to increase their efficiency further, instead, nowadays a-Si is more preferred used in tandem or multi-junction structure such as HIT (S. Sundaram et al., 2018).

Microcrystalline silicon (μc-Si:H) or nanocrystalline silicon (nc-Si:H) is a mixed-phase material composed of interconnected microcrystalline grains embedded in an amorphous matrix (F. Meillaud et al., 2015) that is easy to tune with a bandgap of 1.12eV close to that of crystalline silicon (Arno Smets et al., 2016). (μc-Si:H) solar cells are plasma-deposited by PECVD techniques in extremely thin layers (1μm) on different substrates. Nevertheless, these cells are susceptible to growth conditions, if (μc-Si:H) is deposited on an improper surface texture, unwanted 2-D defective (nanoporous) zones would appear, reducing the initial electrical performance of the cells and their stability over time (Simon Hänni et al., 2013), (J. Bailat et al., 2006). This can be avoided by depositing nc-Si:H layer on a flat superstrate called flat scattering back reflector (FSBR) (Lourens v. Dijk et al., 2016). Another major challenge of μc-Si is that its absorption coefficient is smaller than that of amorphous material, so that effective light absorption requires thicker layers of μc-Si (1-2 μm) (V. Avrutin et al., 2014). Using gas precursors for example SiF4 turning μc-Si:H to μc-Si:F:H has formed high crystallinity and large grain size in the layers, thus increasing absorption in the near-infrared region (F. Meillaud et al., 2015).

CdTe solar cell is the most productive PV among thin-film technologies. It has fewer processing stages, and more cost-saving than standard silicon-based technologies (V. M. Fthenakis et al., 2018). CdTe thin-film is usually fabricated by vapor-transport

deposition. Standard CdTe solar cell uses superstrate configuration: a glass substrate, TCO, the n-type layer (CdS), the p-type CdTe absorber layer, and the metal back contact (W. K. Metzger et al., 2019). It has a good optical absorption, an ideal bandgap of 1.5 eV well matched with the solar spectrum, insignificant efficiency loss, and superb stability (S. Sundaram et al., 2018). The biggest challenge of the cell is to increase photovoltage, which includes solving the core content problems such as recombination, low carrier density, and poor open-circuit voltage (G. M Wilson et al., 2020). Recent studies have shown that the employment of a CdSeTe alloy layer between the emitter and the CdTe can intensify carrier lifetime, passivate grain boundaries, densify short-circuit current, and increase efficiency (X. Zheng et al., 2019). The research of Cu removal as a dopant in CdTe deposition and doping polycrystalline CdSeTe/CdTe films with group-V dopants (As, P, Sb) has also been reported to gain a rise of absorber majority-carrier density, a higher photocurrent, stability, and efficiency, and lower dopant diffusivity (W. K. Metzger et al., 2019).

CIGS is also an outstanding absorber material with a large absorption coefficient. It can be fabricated by co-evaporation or metal selenization/ sulfurization methods. CIGS solar cell is deposited from the bottom up, called "substrate" with a substrate made from glass, metal, or plastic, Mo as the back contact, CIGS p-type absorber, thin CdS buffer layer, and the i-ZnO/ZnO:Al acting as a transparent front contact (K. H. Ong et al., 2018). The challenges of performance- and cost-effective scaling in both module size and production volume have limited CIGS. For this problem, monolithic integration may be a solution that enables patterning films deposited on a single insulating/insulated metal substrate with multiple cells in a sequence. Besides, improving the design of production tools and in situ metrology of control, cadmium-free buffer deposition, accelerating diffusion-limited metal selenization/sulfurization processes, and increasing the utilization of the materials of high-rate co-evaporation tools will be auxiliary to monolithic integration (G. M Wilson et al., 2020).

The third generation of PV technologies consists of emerging thin films such as organic (OSC), dye-sensitized (DSSC), perovskite (PSC), quantum dot solar cells (QDSC), and multi-junction solar cells (MJSC). Organic solar cells (OSC) based on semiconducting polymers have many significant benefits: cost-saving and low-temperature preparation processes, mechanical flexibility, the prospect of deposition on flexible substrates, and color adjusting. The organic compounds used in OSC are polymers or oligomers formed by carbon and hydrogen atoms or added nitrogen, sulfur, and oxygen. They are doped, or photoexcited to be semiconducting (V. M. Fthenakis et al., 2018). OSCs use polymer as electron-donor material along with fullerenes as the electron-acceptor material. OSCs are produced by low-cost processes like spin coating, roll-to-roll processing, printing methods or vacuum evaporation (Taylor, 2015). Two critical challenges in producing OSCs are weak optical absorption coefficient and low transport mobility. The use of metallic nanostructures to scatter incident sunlight and plasmonic nanostructures in the absorbing layer can improve the cell's optical absorption efficiency. Exploiting light trapping methods and anti-reflection are also good methods to intensify the power conversion efficiency of OSCs ((J. Ajayan et al., 2020). Recently, non-fullerene acceptor, all polymer, and double-cable polymer solar cells have gained attention from researchers for their potential in replacing fullerene derivatives that have weak stability, restricted tunable energy level, and low absorption in the visible area.

Dye-sensitized solar cell (DSSC) is an affordable, and environment-friendly hybrid organic-inorganic technology. It utilizes organic dyes (typically ruthenium-based) coating on an electron-accepting material (e.g., TiO_2), surrounded by organic electrolyte to regenerate the dye. The dyes have the advantage of wide solar spectrum absorbing, and the TiO_2 nanoparticles improve the surface area of the adsorbed dye coating, resulting in light absorption efficiency. Its transparency, various shapes, and ability to perform in low light conditions and high temperatures make DSSC suitable for building integration. With the maximum efficiency of only 14.3%, there are many studies seeking solutions to improve DSSC nowadays (K. Kakiage et al., 2015). Co-sensitization method of combining different dyes is a promising approach to improve cell efficiency, preventing dye aggregation. Copper complexes and cobalt-based redox mediators can be potential alternations of unstable triiodide/iodide redox couple. Besides, liquid redox electrolyte used in DSSCs is another concern. The electrolyte will freeze at low temperatures that stops power output, and will expand at high temperatures, react with sealant, and cause a risk of leakage. Acrylate-based and epoxy-based sealants can prevent this leakage due to the resistance to liquid electrolytes in their low polarity compounds and the use of photopolymerizable functional group in their compounds (ThreeBond Inc., n.d.).

Perovskites solar cell (PSC) is the fastest-growing high technology in PV history. PSC contains a perovskite structured compound, which typically is a hybrid organic-inorganic lead or tin halide-based material. High absorbing coefficients, less-sensitive to structure defects, tunable bandgaps for single-junction gadgets and Si-based tandem cells, long diffusion lengths, low excitonic binding energy, long-lasting carrier transport, and facile solution process are all the outstanding advantages of PSCs. Low-temperature mass manufacturing techniques such as ink-jet printing, blade coating, and roll-to-roll printing can be used to fabricate PSC (F. Huang et al., 2019). Three main challenges that need to be addressed before perovskite PV technology can become commercialized are exhibiting long-term module working stability, scaling up to wide areas, and preventing or minimizing the risks of lead contamination (V. M. Fthenakis et al., 2018). In the aspect of instability, double or triple cationic preparations for balancing the molecular packing density can provide the functional trends for perovskite molecular stabilization. Ultrathin ALD Al_2O_3 are proved to hinder the iodide migration very effectively on the perovskite surface without causing any drastic changes to the perovskite absorber properties, thus prevent degradation in PSC (C. Das et al., 2020). Besides, proper encapsulation and work in modifying the device layers can address stability issues related to moisture exposure. Less toxic Pb-free (e.g., Ge-, Bi-, Sb-based) perovskites have shown promise to replace Pb. In the other hand, their much poorer efficiencies and worse stability than Pb-based cells require further research to understand the structural properties as well as the crystallization of these lead-free perovskites.

Multi-junction solar cell (MJSC) is the most efficient photovoltaics at present (47.1%), making them suitable in space applications and concentrator photovoltaic systems (N. R. E. Laboratory, 2020) (A. HM Smets et al., 2016). The basic concept of MJSCs is to combine multiple III-V materials with unique band gaps. Its architecture consists of the most elevated bandgap junction first, and last is the lowest bandgap material as photons with energy below the bandgap are distributed without a loss (Giancarlo C. Righini, and

Francesco Enrichi, 2019). The two popular methods for growing III-V SCs on a substance substrate (e.g., silicon, Ge, InP wafers) are direct-epitaxial growth and wafer bonding-based layer transition (W. Yang et al., 2011). Since the MJSC layers are linked electrically and mechanically in a monolithic cell, the selection of materials for each layer must conform with precise prerequisites, not only based on the appropriate distribution of the spectral interval of solar radiation but also identified with their mechanical and electrical properties. In detail, the crystal lattice constant of the subcells should be firmly coordinated for maximum growth and subsequent crystal consistency, inducing lattice-matched devices. Therefore, to acquire the best efficiency, lattice matching, and current matching are essential (G. C. Righini et al., 2019). Also, the materials chosen in MJSCs need to have large coefficients of absorption, long lifetimes of the minority carrier, and high portability to ensure the device's high performance. Recently, there have been many studies in building concentrator six-junction solar cell devices that can obtain and exceed 50% efficiency, opening a pathway for low-cost utility-scale solar technology systems.

Quantum dot solar cell (QDSC) contains a unique class of semiconductors consisting of II-VI, III-V, or IV-VI periodic group elements that are nanocrystals and can confine electrons (quantum confinement). QDs with a tunable bandgap in various sizes and intermediate band formation ability to match the board solar spectrum distribution have become a solution against the excess energy leakage of photons. Methods to manufacture DQSCs can be electron-beam lithography, self-assembly growth, organometallic or colloidal (wet chemistry) synthesis. Like perovskite solar cells, heavy metals (like Pb, Ca, Se) used in QDSCs raise huge concerns about their extreme toxicity that requires a very stable polymer shell or replacement by other non-toxic alternatives (Mikhail Boldyrev et al., 2018). There are different configurations of QDSCs: quantum dot sensitized SCs, colloidal nanocrystal quantum dot SCs, quantum dot organic bulk hetero-junction SCs, quantum dot bulk nano-hetero-junction SCs, metal oxide/quantum dot bilayer hetero-junction SCs (J. Ajayan et al., 2020). In general, their main challenges are to increase efficiency and stability. Enhancing carrier lifetime and charge transport properties to boost the cell performance have become the goal of colloidal nanocrystal QDSC (Zhenhua Sun et al., 2015). Polysulfide redox in offers longer stability for semiconductors in liquid electrolytes has recently become the most common redox mechanism used in quantum dot sensitized SC (QDSSC) (J. Tian et al., 2016). All-solid-state QDSSC using spiro-OMeTAD as HTM is a promising solution that can improve stability and performance in the long term (Dr. So-Min Yoo et al., 2020).

Besides delving into the challenges of manufacturing technology of different PV solar cells, the thesis has also discussed the challenges in the sustainable growth of current commercialized solar cells, which focuses on the materials availability, safety and health in manufacturing and public environment, production cost, waste treatment - recycling end-of-life PV modules. The materials-availability section has provided current materials production and assessed future PV materials demands by different scenarios: optimistic (low demand scenario), neutral (medium demand scenario), and pessimistic (high demand scenario), thereby indicated that the vulnerabilities in future supply security for numerous elements would threaten the global transition to green energy technology. With the expansion of PV deployment, recycling end-of-life PVs

and recovering valuable materials will become compulsory. While PV solar cells are considered green and renewable technologies, their fabrication still has environmental health and safety risks. The thesis has listed possible hazards for occupation and public health, also suggested precautions, and emphasized the important role of the multiple-level controlling plan (engineering and administrative controls, personal protection equipment, and work procedures). The production cost section focuses on the roadmap with opportunities to reduce cost on III-V materials-based solar cells, in which improvement in technologies, methods, and tools is necessary. Recycling end-of-life PV modules prevents the leaching of the toxic chemical into landfills and recovers valuable sources. The last section has reviewed different processes with various approaches to recycle c-Si and thin-film PV modules, ensuring the effectiveness of the PV recycling process that solves all the issues concerned before.

7. DISCUSSION AND CONCLUSION

Solar cell technology is a promising industry toward the worldwide trend of carbon neutrality as its module emits no emissions during generation and has less carbon footprint than fossil fuels. Gaining huge attention from R&D, the development of solar cells is progressive and rapid. There is no doubt that in the near future, the obstacles solar cell technology is facing now will be completely solved or greatly improved. Solar energy will take the step of fossil energy, meet the global demand, minimizing the cost, and replace old power infrastructure.

8. REFERENCES

U.S. Department of Energy's Office of Energy Efficiency and Renewable Energy, u.d. *Perovskite Solar Cells.* [Online]
Available at: https://www.energy.gov/eere/solar/perovskite-solar-cells
[Använd November 2020].

A. Babayigit et al., 2016. Toxicity of organometal halide perovskite solar cells. *Nature Materials* , Volym 15, p. 247–251.

A. Babayigit et al., 2018. Environment versus sustainable energy: The case of lead halide perovskite-based solar cells. *MRS Energy & Sustainability,* Volym 5, E1.

A. Feltrin, A. Freundlich, 2008. Material considerations for terawatt level deployment of photovoltaics. *Renewable Energy,* 33(2), pp. 180-185.

A. HM Smets et al., 2016. Chapter III: PV technology. i: *Solar Energy: The physics and engineering of photovoltaic conversion, technologies, and systems* . u.o.:UIT Cambridge, p. 290.

A. HM Smets et al., 2016. Crystalline silicon solar cells. i: A. H. S. e. al., red. *Solar Energy: The physics and engineering of photovoltaic conversion, technologies and systems.* u.o.:UIT Cambridge, pp. 298-344.

A. HM Smets et al., 2016. *Solar Energy: The physics and engineering of photovoltaic conversion, technologies, and systems.* u.o.:UIT Cambridge.

A. HM Smets et al., 2016. The III-V PV technology. i: *Solar Energy: The physics and engineering of photovoltaic conversion, technologies and systems.* u.o.:UIT Cambridge, England, p. 367.

A. K. Choudhary et al., 2020. A Systematic Study of the Novel Materials used in Solar Cell Technologies, Opportunities and Challenges. *Energy Research Journal,* 11(1), pp. 28-35.

A. K. K. Kyaw et al., 2013. Intensity dependence of current-voltage characteristics and recombination in high-efficiency solution-processed small-molecule solar cells. *ACS Nano,* 7(5), p. 4569–4577.

A. Lennon, E.R. Rhett, 2017. Manufacturing of Various PV Technologies. i: P. V. W. S. A. F. A. Reinders, red. *Photovoltaic Solar Energy from Fundamentals to Applications.* Chichester: John Wiley & Sons, pp. 463-477.

A. Louwen et al., 2016. Re-assessment of net energy production and greenhouse gas emissions avoidance after 40 years of photovoltaics development. *Nature Communications,* Volym 7, p. 13728.

A. M. Curtin et al., 2020. CdTe in thin film photovoltaic cells: Interventions to protect drinking water in production and end-of-life. *Water-Energy Nexus,* Volym 3, pp. 15-28.

A. M. Ganose et al., 2017. Beyond methylammonium lead iodide: prospects for the emergent field of ns2 containing solar absorbers. *Chemical Communications,* 53(1), pp. 20-44.

A. Ramar and F. M. Wang, 2018. Polymer Solar Cells – An Energy Technology for the Future. i: R. R. A. Pandikumar, red. *Rational Design of Solar Cells for Efficient Solar Energy Conversion.* u.o.:John Wiley & Sons, pp. 283-306.

A. Tomasi, 2017. Simple processing of back-contacted silicon heterojunction solar cells using selective-area crystalline growth. *Nature Energy ,* Volym 2, p. 17062.

Alliance, C., 2020. *Meeting Future Copper Demand.* [Online]
Available at: https://sustainablecopper.org/meeting-future-copper-demand/
[Använd November 2020].

Ana Kanevce et al., 2014. The role of drift, diffusion, and recombination in time-resolved photoluminescence of CdTe solar cells determined through numerical simulation. *Progress in Photovoltaics Research and Applications,* 22(11), pp. 1138-1146.

Annick Anctil, Vasilis Fthenakis, 2012. Life Cycle Assessment of Organic Photovoltaics. i: V. Fthenakis, red. *Third Generation Photovoltaics.* u.o.:InTech .

Antonino Bartolotta, and Giuseppe Calogero, 2019. Dye-sensitized solar cells: from synthetic dyes to natural pigments. i: G. C. R. Francesco Enrichi, red. *Solar Cells and Light Management: Materials, Strategies and Sustainability.* u.o.:Elsevier Science, p. 227.

Arno Smets et al., 2016. Thin-film silicon technology. i: *Solar Energy: The physics and engineering of photovoltaic conversion, technologies and systems.* u.o.:UIT Cambridge, p. 372.

Arvind Shah, Horst Schade, 2017. Tandem and Multijunction Solar Cells. i: *McEvoy's Handbook of hotovoltaics Fundamentals and Applications.* u.o.:Academic Press, p. 541.

B. Conings et al., 2015. Intrinsic Thermal Instability of Methylammonium Lead Trihalide Perovskite. *Advanced Energy Materials,* 5(15).

B. Jo Kim et al., 2016. Selective dissolution of halide perovskites as a step towards recycling solar cells. *Nature Communications,* Volym 7, p. 11735.

Barron, A. R., 2014. Semiconductor Grade Silicon. i: A. R. B. Carissa Smith, red. *Derived from Synthesis and Purification of Bulk Semiconductors by.*
u.o.:https://cnx.org/contents/bGvrPT9L@3/Semiconductor-Grade-Silicon.

Basore, P. A., 1994. Defining terms for crystalline silicon solar cells. *Progress in Photovoltaics,* 2(2), pp. 177-179.

Bell, D. G., u.d. *Molecular Beam Epitaxy.* [Online]
Available at: https://studylib.net/doc/12963427/molecular-beam-epitaxy
[Använd December 2020].

Benda, V., 2018. Crystalline Silicon Solar Cell and Module Technology. i: V. M. F. T. M. Letcher, red. *A Comprehensive Guide to Solar Energy Systems: With Special Focus on Photovoltaic Systems.*
u.o.:Academic Press, pp. 377-439.

Benda, V., 2018. Crystalline Silicon Solar Cell and Module Technology. i: V. M. F. T. M. Letcher, red. *A Comprehensive Guide to Solar Energy Systems.* u.o.:Academic Press, pp. 377-439.

Benjah, M., 2007. *Gallium arsenide unit cell 3D balls.* [Online]
Available at: https://commons.wikimedia.org/wiki/File:Gallium-arsenide-unit-cell-3D-balls.png
[Använd November 2020].

Bernreuter, J., 2020. *Polysilicon Production Processes.* [Online]
Available at: https://www.bernreuter.com/polysilicon/production-processes/#eternal-contender-

fluidized-bed-reactor-technology
[Använd October 2020].

BioIntelligence, 2011. *Study on Photovoltaic Panels Supplementing the impact assessment for a recast of the WEEE directive . Final report,* Paris: Publications Office of the European Commission.

Bosan, H. A., 2021. *Czochralski Process – To Manufacture Monocrystalline Silicon.* [Online]
Available at: https://solarsena.com/czochralski-process-silicon-monocrystal/

Boschloo, G., 2019. Improving the Performance of Dye-Sensitized Solar Cells. *Front. Chem.,* Volym 7:77.

Byrnes, S., 2011. *Shockley–Queisser limit.* [Online]
Available at:
https://en.wikipedia.org/wiki/Shockley%E2%80%93Queisser_limit#:~:text=In%20physics%2C%20the%20Shockley%E2%80%93Queisser,cell%20where%20the%20only%20loss
[Använd November 2020].

C. A. Miller et al., 2020. *Thin Film CdTe Photovoltaics and the U.S..* [Online]
Available at: http://www.firstsolar.com/-/media/First-Solar/Sustainability-Documents/Sustainability-Peer-Reviews/QESST-Thin-Film-PV-Report-2020.ashx
[Använd December 2020].

C. B. Honsberg, S. G. Bowden, 2019. *Float Zone Silicon.* [Online]
Available at: www.pveducation.org
[Använd November 2020].

C. Besancon et al., 2019. Epitaxial Growth of High-Quality AlGaInAs-Based Active Structures on a Directly Bonded InP-SiO2/Si Substrate. *Phys. Status Solidi A,* 217(3).

C. D. Smith et al., 2017. Organic Solar Cells. i: S. A. Kalogirou, red. *McEvoy's Handbook of Photovoltaics: Fundamentals and Applications.* u.o.:Academic Press, p. 1041.

C. Das et al., 2020. Atomic Layer-Deposited Aluminum Oxide Hinders Iodide Migration and Stabilizes Perovskite Solar Cells. *Cell Reports Physical Science,* 1(7), p. 100112.

C. Huang, 2018. Deposition Technologies of High-Efficiency CIGS Solar Cells: Development of Two-Step and Co-Evaporation Processes. *Crystals,* 8(7), p. 296.

C. Liang et al., 2019. Simultaneously boost diffusion length and stability of perovskite for high performance solar cells. *Nano Energy,* Volym 59, pp. 721-729.

C. P. Lee et al., 2017. Use of organic materials in dye-sensitized solar cells. *Materials Today,* 20(5), pp. 267-283.

Cain, F., 2015. *How does the sun produce energy?.* [Online]
Available at: https://phys.org/news/2015-12-sun-energy.html

Cain, F., 2015. *How does the sun produce energy?.* [Online]
Available at: https://phys.org/news/2015-12-sun-energy.html

Calderone, L., 2018. *Quantum Dot Solar Cells are coming.* [Online]
Available at: https://www.altenergymag.com/article/2018/05/quantum-dot-solar-cells-are-

coming/28547
[Använd December 2020].

Cdang et al., 2015. *Amorphous silicon.* [Online]
Available at:
https://en.wikipedia.org/wiki/File:Schematic_of_allotropic_forms_of_silcon_horizontal_plain.svg
[Använd September 2020].

Chen, L. X., 2019. Organic Solar Cells: Recent Progress and Challenges. *ACS Energy Letters,* 4(10), p. 2537–2539.

Chin-Yi Tsai et al., 2014. Development of Tandem Amorphous/Microcrystalline Silicon Thin-Film Large-Area See-Through Color Solar Panels with Reflective Layer and 4-Step Laser Scribing for Building-Integrated Photovoltaic Applications. *Journal of Nanomaterials,* Volym 2014, p. 9.

D. Chen, 2020. 24.58% total area efficiency of screen-printed, large area industrial silicon solar cells with the tunnel oxide passivated contacts (i-TOPCon) design. *Solar Energy Materials and Solar Cells,* Volym 206, p. 110258.

D. H. Kim et al., 2018. Outlook and Challenges of Perovskite Solar Cells toward Terawatt-Scale Photovoltaic Module Technology. *Joule,* 2(8), pp. 1437-1451.

D. Lackner et al., 2017. *Status of Four-junction cell development at Fraunhofer Ise.* u.o., E3S Web of Conferences.

D. T. Blagoeva et al., 2016. *Assessment of potential bottlenecks along the materials supply chain for the future deployment of low-carbon energy and transport technologies in the EU: Wind power, photovoltaic and electric vehicles technologies, time frame: 2015-2030,* u.o.: Joint Research Centre (JRC), the European Commission's science and knowledge service.

D.L.Batzner et al., 2004. Stability aspects in CdTeyCdS solar cells. *Thin Solid Films,* 451–452(22), pp. 536-543.

David M Tex et al., 2014. Control of hot-carrier relaxation for realizing ideal quantum-dot intermediate-band solar cells. *Scientific Reports,* Issue 4.

Dr. So-Min Yoo et al., 2020. Nanoscale Perovskite-Sensitized Solar Cell Revisited: Dye-Cell or Perovskite-Cell ?. *ChemSusChem.,* 13(10), p. 2571–2576..

Dyenamo, u.d. *Organic sensitizing dyes.* [Online]
Available at: https://dyenamo.se/dyenamo_dyes.php#top
[Använd November 2020].

Energy, U. D. o. E. O. o. E. E. a. R., u.d. *The history of solar.* [Online]
Available at: https://www1.eere.energy.gov/solar/pdfs/solar_timeline.pdf
[Använd 2020].

European Commission, 2014. *Report on Critical Raw Materials for the EU: Report of the Ad-Hoc Working Group on Defining Raw Materials,* Brussels, Belgium: European Commission.

F. Haase, 2018. Laser contact openings for local poly-Si-metal contacts enabling 26.1%-efficient POLO-IBC solar cells. *Solar Energy Materials and Solar Cells,* Volym 186, p. 184.

F. Huang et al., 2019. From scalable solution fabrication of perovskite films towards commercialization of solar cells. *Energy and Environmental Science,* Volym 12, pp. 518-549.

F. Meillaud et al., 2015. Recent advances and remaining challenges in thin-film silicon photovoltaic technology. *Materials today,* 18(7), pp. 378-384.

Ferrazza, F., 2017. Crystalline Silicon Solar Cells. i: S. A. Kalogirou, red. *McEvoy's Handbook of Photovoltaics Fundamentals and Applications.* u.o.:Academic Press, p. 183.

First Solar, 2018. Photovoltaic Manufacturing. i: P. A. L. Vasilis M. Fthenakis, red. *publisher logoElectricity from Sunlight.* u.o.:Wiley.

First Solar, 2020. *First Solar Series 6 Plus™ Advanced Thin Film Solar Technology.* [Online]
Available at: http://www.firstsolar.com/-/media/First-Solar/Technical-Documents/Series-6-Plus/Series-6-Plus-Datasheet.ashx?la=en-Emea
[Använd November 2020].

Forrest, S. R., 2005. The Limits to Organic Photovoltaic Cell Efficiency. *MRS Bulletin volume,* Volym 30, p. 28–32.

Frank Dimroth et al., 2014. Comparison of Direct Growth and Wafer Bonding for the Fabrication of GaInP/GaAs Dual-Junction Solar Cells on Silicon. *IEEE Journal of Photovoltaics,* 4(2), pp. 620 - 625.

Freedonia, G., 2020. *Market research.* [Online]
Available at: https://www.marketresearch.com/Freedonia-Group-Inc-v1247/Global-Flat-Glass-13154855/
[Använd November 2020].

G. Birant et al. , 2019. Dielectric-Based Rear Surface Passivation Approaches for Cu(In,Ga)Se2 Solar Cells—A Review. *Applied Science,* 9(4), p. 677.

G. C. Righini et al., 2019. Solar cells' evolution and perspectives: a short review. i: *Solar Cells and Light Management: Materials, Strategies and Sustainability.* u.o.:Elsevier Science.

G. Hodes et al., 1981. Factors influencing output stability of Cd-chalcogenide/polysulfide photoelectrochemical cells. *Solar Energy Materials,* 4(4), pp. 373-381.

G. Kieslich et al., 2015. An extended Tolerance Factor approach for organic–inorganic perovskites. *Chemical Science,* Volym 6, pp. 3430-3433.

G. Lush, 2009. B-coefficient in n-type GaAs. *Solar Energy Materials and Solar Cells,* 93(8), pp. 1225-1229.

G. M Wilson et al., 2020. The 2020 photovoltaic technologies roadmap. *Journal of Physics D: Applied Physics,* 53(49), p. 493001.

George, M. W., 2004. Mineral of the month: indium. *Geotimes,* 2004(November).

Ghaffarzadeh, D. K., 2018. *ITO alternatives 2018-2028: progress review of technology options.* [Online]
Available at: https://www.linkedin.com/pulse/ito-alternatives-2018-2028-progress-review-technology-ghaffarzadeh
[Använd November 2020].

Graham Fisher et al., 2012. Silicon Crystal Growth andWafer Technologies. *Proceedings of the IEEE,* 100(Special Centennial Issue), pp. 1454 - 1474.

Grand view research, 2017. *Indium Market Size, Share & Trends Analysis Report By Product (Primary, Secondary, Type III), By Application (Indium Tin Oxide (ITO), Semiconductors, Solders & Alloys), By Region, And Segment Forecasts, 2018 - 2025,* u.o.: Grand view research.

H. Ellis et al., 2016. Development of high efficiency 100% aqueous cobalt electrolyte dye-sensitised solar cells. *Physical Chemistry Chemical Physics,* 18(12), pp. 8419-8427.

H. Kronmüller et al., 2007. *Handbook of Magnetism and Advanced Magnetic Materials: Spintronics and magnetoelectronics.* u.o.:John Wiley & Sons.

H. U. Sverdrup et al., 2019. Resources, Conservation & Recycling: X. *On the long-term sustainability of copper, zinc and lead supply, using a system dynamics model,* 4(2590-289X).

H.-S. Kim et al., 2012. Lead Iodide Perovskite Sensitized All-Solid-State Submicron Thin Film Mesoscopic Solar Cell with Efficiency Exceeding 9%. *Scientific Reports,* Volym 2, p. 591.

Haoran Zhou et al., 2019. Molecular design and synthesis of D–π–A structured porphyrin dyes with various acceptor units for dye-sensitized solar cells. *Journal od Materials Chemistry C,* 7(10), pp. 2843-2852.

Hatton, R. A., 2018. Organic Photovoltaics. i: V. M. F. Trevor M. Letcher, red. *A Comprehensive Guide to Solar Energy Systems: With Special Focus on Photovoltaic Systems.* u.o.:Academic Press, p. 531.

Huashang Rao et al., 2020. Quantum dot materials engineering boosting the quantum dot sensitized solar cell efficiency over 13%. *Journal of Materials Chemistry A,* 8(20), pp. 10233-10241.

I. Benesperi et al., 2018. The researcher's guide to solid-state dye-sensitized solar cells. *Journal of Materials Chemistry C,* Issue 44, pp. 11759 - 12106.

I. Ghosekar, G. C. Patil, 2019. Thermal stability analysis of buffered layer P3HT/P3HT:PCBM organic solar cells. *IET Optoelectronics,* Volym 13(5).

I. M.-Seró, J. Bisquert, 2010. Breakthroughs in the Development of Semiconductor-Sensitized Solar Cells. *The Journal of Physical Chemistry Letters,* 20(1), p. 3046–3052.

J. Ajayan et al., 2020. A review of photovoltaic performance of organic/inorganic solar. *Superlattices and Microstructures ,* Volym 143.

J. Bailat et al., 2002. Influence of substrate on the microstructure of microcrystalline silicon layers and cells. *Journal of Non-Crystalline Solids,* Volym 299–302, Part 2, pp. 1219-1223.

J. Bailat et al., 2006. *High-Efficiency P-I-N Microcrystalline and Micromorph Thin Film Silicon Solar Cells Deposited on LPCVD Zno Coated Glass Substrates.* Waikoloa, 2006 IEEE 4th World Conference on Photovoltaic Energy Conference.

J. F. Geisz et al., 2018. *Six-Junction Concentrator Solar Cells.* Colorado, USA National Renewable Energy Laboratory.

J. Haschke et al., 2018. Silicon heterojunction solar cells: Recent technological development and practical aspects - from lab to industry. *Solar Energy Materials and Solar Cells,* Volym 187, pp. 140-153.

J. M. Burst et al., 2016. CdTe solar cells with open-circuit voltage breaking the 1 V barrier. *Nature Energy,* 1(5), p. 16015 .

J. M. Kephart et al., 2018. Sputter-Deposited Oxides for Interface Passivation of CdTe Photovoltaics. *IEEE Journal of Photovoltaics,* 8(2), pp. 587 - 593.

J. Park et al., 2018. High Efficiency Inorganic/Inorganic Amorphous Silicon/Heterojunction Silicon Tandem Solar Cells. *Scientific Reports,* 15386(8).

J. Pradhan et al., 2020. Encapsulation of CsPbBr3 Nanocrystals by a Tripodal Amine Markedly Improves Photoluminescence and Stability Concomitantly via Anion Defect Elimination. *Chemistry of Materials,* 32(17), p. 7159–7171.

J. Pritchard et al., 2016. Solar Power Concentrators for Space Applications. *PAM Review Energy Science & Technology,* Volym 3, pp. 2-26.

J. Ramanujam et al., 2017. Copper indium gallium selenide based solar cells – a review. *Energy Environ. Sci.,* 10(6), pp. 1306-1319.

J. S. Stein, 2019. *Performance of Bifacial Photovoltaic Modules and Systems.* Chicago, Proc. of the 46th IEEE Photovoltaic Specialists Conf..

J. Simon et al., 2016. GaAs Solar Cells Grown by Hydride Vapor-Phase Epitaxy and the Development of GaInP Cladding Layers. *IEEE Journal of Photovoltaics,* 6(1), pp. 191 - 195.

J. Simon et al., 2019. III-V-Based Optoelectronics with Low-Cost Dynamic Hydride Vapor Phase Epitaxy. *Crystals,* 9(1), p. 3.

J. Tian et al., 2016. Enhanced Performance of PbS-quantum-dot-sensitized Solar Cells via Optimizing Precursor Solution and Electrolytes. *Scientific Reports,* Volym 6.

J. Werner et al., 2005. Efficiency limitations of polycrystalline thin film solar cells: case of Cu(In,Ga)Se2. *Thin Solid Films,* Volym 480-481, pp. 399-409.

J. Zhang et al., 2017. Solid-State Dye-Sensitized Solar Cells. i: G. B. A. H. Haining Tian, red. *Molecular Devices for Solar Energy Conversion and Storage.* Singapore: Springer, pp. 151-185.

J.D.Major et al., 2017. P3HT as a pinhole blocking back contact for CdTe thin film solar cells. *Solar Energy Materials and Solar Cells,* Volym 172, pp. 1-10.

Jasim, K. E., 2015. Quantum Dots Solar Cells. i: L. A. Kosyachenko, red. *Solar Cells - New Approaches and Reviews.* u.o.:InTech, pp. 303-331.

Jason A.Peck et al., 2017. High deposition rate nanocrystalline and amorphous silicon thin film production via surface wave plasma source. *Surface and Coatings Technology,* Volym 325, pp. 370-376.

Jeffrey Yang et al., 2003. Amorphous silicon based photovoltaics—from earth to the “final frontier”. *Solar Energy Materials and Solar Cells,* 78(1-4), pp. 597-612.

Jones, M. R., 2009. *Schematic illustration of a generic dye-sensitized solar cell.* [Online] Available at: https://commons.wikimedia.org/w/index.php?curid=6881622

Jung-Min Ji et al., 2020. 14.2% Efficiency Dye-Sensitized Solar Cells by Co-sensitizing Novel Thieno[3,2-b]indole-Based Organic Dyes with a Promising Porphyrin Sensitizer. *Advanced Energy Materials,* 10(15).

K. A. W. Horowitz et al., 2018. *A Techno-Economic Analysis and Cost Reduction Roadmap for III-V Solar Cells,* Golden, CO: National Renewable Energy Laboratory (NREL).

K. Fujiwara et al., 2012. Effect of silicon/crucible interfacial energy on orientation of multicrystalline silicon ingot in unidirectional growth. *Journal of Applied Physics,* 112(11).

K. H. Ong et al., 2018. Review on Substrate and Molybdenum Back Contact in CIGS Thin Film Solar Cell. *International Journal of Photoenergy,* Volym 2018, p. 14.

K. Kakiage et al., 2015. Highly-efficient dye-sensitized solar cells with collaborative sensitization by silyl-anchor and carboxy-anchor dyes. *Chemical Communications,* 51(88), pp. 15894-15897.

K. Kakiage et al., 2015. Highly-efficient dye-sensitized solar cells with collaborative sensitization by silyl-anchor and carboxy-anchor dyes. *Chemicals Communications,* Issue 51, pp. 15894-15897.

K. Komoto et al., 2018. *End-of-Life Management of Photovoltaic Panels: Trends in PV Module Recycling Technologies,* Golden, CO (United States): National Renewable Energy Lab (NREL).

K. L. Schulte et al., 2017. Development of GaInP Solar Cells Grown by Hydride Vapor Phase Epitaxy. *IEEE Journal of Photovoltaics,* 7(4), pp. 1153 - 1158.

K. Sharma et al., 2018. Dye-Sensitized Solar Cells: Fundamentals and Current Status. *Nanoscale Research Letters,* Volym 13, p. 381.

K. Yoshikawa et al., 2017. Silicon heterojunction solar cell with interdigitated back contacts for a photoconversion efficiency over 26%. *Nature Energy volume,* Volym 2, p. 17032.

Klein, C., 2020. *Silicates.* [Online]
Available at: https://www.britannica.com/science/mineral-chemical-compound/Silicates

Kretzer, M., 2013. *Dye-sensitized solar cells, a low-cost, highly efficient alternative to silicon based solar cells.* [Online]
Available at: http://materiability.com/portfolio/dye-sensitized-solar-cells/

L. V. Mercaldo, P. D. Veneri , 2019. Silicon solar cells: materials, technologies, architectures. i: G. C. R. Francesco Enrichi, red. *Solar Cells and Light Management.* u.o.:Elsevier Science, p. 100.

Latunussa C. et al. , 2016. *Analysis of Material Recovery from Silicon Photovoltaic Panels,* Luxembourg: Publications Office of the European Union.

Latunussa C. et al., 2016. *Analysis of material recovery from photovoltaic panels,* Luxembourg: Joint Research Centre (European Commission).

Laura Cozzi et al., 2021. *Global Energy Review 2021. Assessing the effects of economic recoveries on global energy demand and CO2 emissions in 2021.,* u.o.: International Energy Agency.

Lourens v. Dijk et al., 2016. Plasmonic Scattering Back Reflector for Light Trapping in Flat Nano-Crystalline Silicon Solar Cells. *ACS Photonics,* 4(3), p. 685–691.

M. A. Green et al., 2014. Solar cell efficiency tables (Version 45). *Progress in Photovoltaics,* 23(1), pp. 1-9.

M. Freitag et al., 2015. High-efficiency dye-sensitized solar cells with molecular copper phenanthroline as solid hole conductor. *Energy & Environment Science,* Issue 9, pp. 2527 - 2798.

M. Freitag et al., 2016. Copper Phenanthroline as a Fast and High-Performance Redox Mediator for Dye-Sensitized Solar Cells. *The Journal of Physical Chemistry C,* Volym 120, p. 9595–9603.

M. J. Griffith et al., 2016. Combining Printing, Coating, and Vacuum Deposition on the Roll-to-Roll Scale: A Hybrid Organic Photovoltaics Fabrication. *IEEE Journal of Selected Topics in Quantum Electronics,* 22(1).

M. Lumb, 2015. Incorporating photon recycling into the analytical drift-diffusion model of high efficiency solar cells. *Journal of Applied Physics,* Volym 116, p. 194504.

M. Nakamura et al., 2019. Cd-Free Cu(In,Ga)(Se,S)2 Thin-Film Solar Cell With Record Efficiency of 23.35%. *IEEE Journal of Photovoltaics,* 9(6), pp. 1863 - 1867.

M. Ochoa et al., 2020. Challenges and opportunities for an efficiency boost of next generation Cu(In,Ga)Se2 solar cells: prospects for a paradigm shift. *Energy & Environmental Science,* Volym 13, pp. 2047-2055.

M. Powalla et al., 2017. Advances in Cost-Efficient Thin-Film Photovoltaics Based on Cu(In,Ga)Se2. *Engineer,* 3(4), pp. 445-451.

M. R. Filip, F. Giustino, 2018. The geometric blueprint of perovskites. *PNAS ,* 115(21), pp. 5397-5402.

M. Späth et al., 2003. Reproducible manufacturing of dye-sensitized solar cells on a semi-automated baseline. *Progress in Photovoltaics,* 11(3), pp. 207-220.

Madelung, O., 2004. III-V compounds. i: *Semiconductors: Data Handbook.* Berlin: Springer, pp. 71-172.

Manda Xiao et al., 2014. A Fast Deposition-Crystallization Procedure for Highly Efficient Lead Iodide Perovskite Thin-Film Solar Cells. *Angewandte Chemie,* 53(37), pp. 9898-9903.

Markus Fischer et al., 2020. *International technology roadmap for photovoltaic (ITRPV) - 2019 results,* Frankfurt: VDMA Photovoltaic Equipment.

Markus Fischer et al., 2021. *International technology roadmap for photovoltaic (ITRPV) - results 2020,* Frankfurt: VDMA e. V..

Martineau, D., 2012. *Dye solar cells for real - The Assembly Guide for Making Your Own Solar Cells.* [Online]
Available at: https://www.solaronix.com/documents/dye_solar_cells_for_real.pdf
[Använd November 2020].

Mathew S. et al., 2014. Dye-sensitized solar cells with 13% efficiency achieved through the molecular engineering of porphyrin sensitizers. *Nature Chemistry,* Volym 6, p. 242–247.

Mikhail Boldyrev et al., 2018. Lead: properties, history, and applications. *WikiJournal of Science,* 2(1), p. 7.

Montemayor, K., u.d. *The rise of organic photovoltaics.* [Online]
Available at: https://solenergy.com.ph/the-rise-of-organic-photovoltaics/
[Använd 2020].

Mora-Seró, I., 2020. Current Challenges in the Development of Quantum Dot Sensitized Solar Cells. *Advanced Energy Materials,* 10(33).

Muzzillo, C. P., 2017. Review of grain interior, grain boundary, and interface effects of K in CIGS solar cells: Mechanisms for performance enhancement. *Solar Energy Materials and Solar Cells 172:18-24,* Volym 172, pp. 18-24.

N. K. Foley et al., December 2017. Gallium. i: J. H. D. J. R. R. S. I. a. D. C. B. Klaus J. Schulz, red. *Critical Mineral Resources of the United States—Economic and Environmental Geology and Prospects for Future Supply.* u.o.:U.S. Geological Survey Professional Paper 1802, p. Chapter H.

N. K. Kumawat, 2015. Band Gap Tuning of CH3NH3Pb(Br1–xClx)3 Hybrid Perovskite for Blue Electroluminescence. *ACS Applied Materials & Interfaces,* 7(24), p. 13119–13124.

N. Milenkovic et al., 2017. 20% efficient solar cells fabricated from epitaxially grown and freestanding n-type wafers. *Solar Energy Materials and Solar Cells,* Volym 159, pp. 570-575.

N. R. E. Laboratory, 2020. *Best Research-Cell Efficiency Chart,* Golden, CO: The National Renewable Energy Laboratory.

N. R. Paudel et al., 2011. *Improvements in ultra-thin CdS/CdTe solar cells.* Seattle, 37th IEEE Photovoltaic Specialists Conference.

N. Y. Nia et al., 2019. Perovskite solar cells. i: G. C. R. F. Enrichi, red. *Solar Cells and Light Management Materials Strategies and Sustainability.* u.o.:Elsevier Science, p. 314.

N. Y. Nia et al., 2019. Perovskite solar cells. i: G. C. R. F. Enrichi, red. *Solar Cells and Light Management: Materials, Strategies and Sustainability.* u.o.:Elsevier Science, p. 314.

N. Y. Nia et al., 2019. *Solar Cells and Light Management: Materials, Strategies and Sustainability.* first red. u.o.:Elsevier Science.

Neha Arora et al., 2017. Perovskite solar cells with CuSCN hole extraction layers yield stabilized efficiencies greater than 20%. *Science,* 358(6364), pp. 768-771.

Nelson, J., 2003. *The Physics of Solar Cells.* 1st red. u.o.:Imperial College Press.

Office of Energy Efficiency & Renewable Energy, u.d. *Cadmium telluride.* [Online]
Available at: https://www.energy.gov/eere/solar/cadmium-telluride
[Använd October 2020].

O'Kane, M., u.d. *Perovskite Solar Cells: Causes of Degradation.* [Online]
Available at: https://www.ossila.com/pages/perovskite-solar-cell-degradation-causes
[Använd 2021].

P. Danz et al., 2019. Experimental Study on Fluorine Release from Photovoltaic Backsheet Materials Containing PVF and PVDF during Pyrolysis and Incineration in a Technical Lab-Scale Reactor at Various Temperatures. *Toxics,* 7(3), p. 47.

P. Kumaresan et al., 2014. Fused-Thiophene Based Materials for Organic Photovoltaics and Dye-Sensitized Solar Cells. *Polymers ,* 6(10), pp. 2645-2669.

Petersen, K., 1982. Silicon as a mechanical material. *IEEE,* 70(5), pp. 420 - 457.

Q.-Y. Tong, U. Gösele, 1998. *SemiConductor Wafer Bonding: Science and Technology.* 1st red. u.o.:Wiley-Interscience.

Qi Chen et al., 2015. Under the spotlight: The organic–inorganic hybrid halide perovskite for optoelectronic applications. *Nanotoday,* 10(3), pp. 355-396.

Qi Zhang et al., 2018. Perovskite solar cells: must lead be replaced – and can it be done?. *Sci Technol Adv Mater.,* 19(1), p. 425–442.

R. Dagan et al., 2016. Minority carrier recombination of ordered Ga0.51In0.49P at high temperatures. *Applied Physics Letters,* Volym 109, p. 222106 .

R. Dams, K. Hintze, 2017. Chapter 1: Industrial Aspects of Fluorinated Oligomers and Polymers. i: H. S. B. Ameduri, red. *Fluorinated Polymers: Volume 2: Applications.* Cambridge, UK: Royal Society of Chemistry, pp. 1-31.

R. Krause et al., 2014. *Wafer Bonded 4-Junction GaInP/GaAs//GaInAsP/GaInAs concentrator solar cells.* u.o., AIP Conference Proceedings 1616, 45.

R. M. France, 2016. Design Flexibility of Ultrahigh Efficiency Four-Junction Inverted Metamorphic Solar Cells. *IEEE Journal of Photovoltaics,* 6(2), pp. 578 - 583.

R. M. Geisthardt, 2015. Status and Potential of CdTe Solar-Cell Efficiency. *IEEE Journal of Photovoltaics,* 5(4), pp. 1217 - 1221.

Robert U. Ayres, Leslie Ayres, 2002. i: L. A. Robert U. Ayres, red. *A handbook of industrial ecology.* u.o.:Edward Elgar Publishing, p. 396.

Rosario Vidal et al., 2020. Assessing health and environmental impacts of solvents for producing perovskite solar cells. *Nature Sustainability .*

Rühle, S., 2016. Tabulated values of the Shockley–Queisser limit for single junction solar cells. *Solar Energy,* Volym 130, pp. 139-147.

S. Albrecht et al., 2014. Quantifying Charge Extraction in Organic Solar Cells: The Case of Fluorinated PCPDTBT. *The Journal of Physical Chemistry Letters,* 5(7), p. 1131–1138.

S. Ananthakumar et al., 2019. Role of co-sensitization in dye-sensitized and quantum dot-sensitized solar cells. *SN Applied Sciences,* 1(186).

S. Carrara et al. from JRC, 2020. *Raw materials demand for wind and solar PV technologies in the transition towards a decarbonised energy system,* Luxembourg: Publications Office of the European Union.

S. Sundaram et al., 2018. Thin Film Photovoltaics. i: V. M. F. Trevor M. Letcher, red. *A Comprehensive Guide to Solar Energy Systems: With Special Focus on Photovoltaic Systems.* u.o.:Academic Press, p. 764.

S. W. Glunz, 2018. SiO2 surface passivation layers – a key technology for silicon solar cells. *Solar Energy Materials and Solar Cells,* Volym 185, pp. 260-269.

Simon Hänni et al., 2013. On the Interplay Between Microstructure and Interfaces in High-Efficiency Microcrystalline Silicon Solar Cells. *IEEE,* 3(1), pp. 11 - 16.

Simon Philipps et al., 2020. *Photovoltaics report September 2020,* Freiburg: Fraunhofer Institute for Solar Energy Systems, ISE with support of PSE Projects GmbH.

Simon, H., 2014. *Microcrystalline Silicon for High-Efficiency Thin-Film Photovoltaic Devices,* u.o.: EPFL scientific publications.

Solar Frontier, u.d. *Solar Frontier CIS Modules.* [Online]
Available at: https://static.webshopapp.com/shops/078108/files/030967508/solar-frontier-solarsolutions1-1-2.pdf
[Använd November 2020].

Solar Market, u.d. *Different Types of Solar Panels.* [Online]
Available at: https://www.solarmarket.com.au/residential-solar/different-types-of-panels/
[Använd November 2020].

Sonali Das et al., 2020. *Beyond 4% photo conversion efficiency achieved by low temperature phase selective solvothermally synthesized CZTS quantum dot solar cell.* u.o., AIP Conference Proceedings .

Streefkerk, R., 2019. *Qualitative vs. quantitative research.* [Online]
Available at: https://www.scribbr.com/methodology/qualitative-quantitative-research/

Swanson, R. M., 1985. *Point contact solar cells - Theory and modeling.* Las Vegas, 18th IEEE Photovoltaic Specialists Conf. .

T. Wang et al., 2019. Facile Synthesis of Methylammonium Lead Iodide Perovskite with Controllable Morphologies with Enhanced Luminescence Performance. *Nanomaterials (Basel),* 9(12), p. 1660.

T. Baines et al., 2018. CdTe Solar Cells. i: V. M. F. Trevor M. Letcher, red. *A Comprehensive Guide to Solar Energy Systems: With Special Focus on Photovoltaic Systems.* u.o.:Academic Press, p. 451.

T. Feurer et al., 2019. RbF post deposition treatment for narrow bandgap Cu(In,Ga)Se2 solar cells. *Thin Solid Films,* Volym 670, pp. 34-40.

T. Jia et al., 2020. 14.4% Efficiency All-Polymer Solar Cell with Broad Absorption and Low Energy Loss Enabled by a Novel Polymer Acceptor. *Nano Energy,* Volym 72.

T. Kirchartz et al., 2012. Understanding the Thickness-Dependent Performance of Organic Bulk Heterojunction Solar Cells: The Influence of Mobility, Lifetime, and Space Charge. *The Journal of Physical Chemistry Letters,* 3(23), p. 3470–3475.

T. Liu et al., 2017, . High-Performance Formamidinium-Based Perovskite Solar Cells via Microstructure-Mediated δ-to-α Phase Transformation. *Chemistry of Materials,* 29(7), p. 3246–3250.

T. Moot et al., 2020. Beyond Strain: Controlling the Surface Chemistry of CsPbI3 Nanocrystal Films for Improved Stability against Ambient Reactive Oxygen Species. *Chemistry of Materials,* 32(18), p. 7850–7860.

T. N. D. Tibbits et al., 2014. *New Efficiency Frontiers With Wafer-bonded Multi-Junction Solar Cells.* u.o., European PV Solar Energy Conference.

Taylor, D. M., 2015. Vacuum-thermal-evaporation: the route for roll-to-roll production of large-area organic electronic circuits. *Semiconductor Science and Technology,* Volym 30.

ThreeBond Inc., u.d. *General Catalog/Products Guide.* [Online]
Available at: https://threebond.com/wp-content/uploads/Products-Guide_ver6-LOCAL.pdf
[Använd November 2020].

Tuladhar et al., 2016. Low Open-Circuit Voltage Loss in Solution-Processed Small-Molecule Organic Solar Cells. *ACS Energy Letters ,* 1(1).

U.S. Geological Survey, 2021. *Mineral Commodity Summaries 2021,* Reston, Virginia: U.S. Geological Survey.

United States Department of Labor, u.d. *Occupational Safety and Health Administration.* [Online]
Available at: https://www.osha.gov/cadmium
[Använd May 2021].

US National Renewable Energy Laboratory, 2013. *Quantum Dots Promise to Significantly Boost.* [Online]
Available at: https://www.nrel.gov/docs/fy13osti/59015.pdf
[Använd December 2020].

Uwe Rau et al., 2017. Efficiency Potential of Photovoltaic Materials and Devices Unveiled by Detailed-Balance Analysis. *Phisical Review Applied,* 7(4).

V. Avrutin et al., 2014. Amorphous and micromorph Si solar cells: current status and outlook. *Turkish Journal of Physics,* 38(3), pp. 526-542.

V. D'Innocenzo, 2014. Excitons versus free charges in organo-lead tri-halide perovskites. *Nature Communications ,* Volym 5.

V. M. Fthenakis et al., 2018. *Electricity from Sunlight.* 2nd red. u.o.:whiley.

V.M. Fthenakis, P.D. Moskowitz et al., 1995. Thin-film photovoltaic cells: health and environmental issues in their manufacture, use and disposal. Progress in Photovoltaics: Research and Applications,. *Progress in Photovoltaics,* 3(5), p. 295–306.

Victor I. Klimov et al., 2020. Spectroscopic insights into high defect tolerance of Zn:CuInSe2 quantum-dot-sensitized solar cells. *Nature Energy,* Volym 5, p. 409–417.

W. Abdelaziz et al., 2019. Possible efficiency boosting of non-fullerene acceptor solar cell using device simulation. *Optical Materials,* Volym 91, pp. 239-245.

W. G. Adams, R. E. Day, 1877. V. The action of light on selenium. *Proceedings of the Royal Society of London,* Volym 25, pp. 171-178.

W. K. Metzger et al., 2019. Exceeding 20% efficiency with in situ group V doping in polycrystalline CdTe solar cells. *Nature Energy,* 4(10), p. 837–845.

W. K. Metzger, 2005. Analysis of charge separation dynamics in a semiconductor junction. *Physical Review B,* 71(3), p. 035301.

W. Shockley and H. Queisser, 1961. Detailed Balance Limit of Efficiency of pn Junction Solar Cells. *Journal of Applied Physics,* 32(3), p. 510.

W. Shockley, H. J. Queisser, 1961. Detailed balance limit of efficiency of p-n junction solar cells. *Journal of Applied Physics,* 32(3), pp. 510-519.

W. Wang et el., 2020. Facile Secondary Deposition for Improving Quantum Dot Loading in Fabricating Quantum Dot Solar Cells. *Journal of the American Chemical Society,* 141(10), p. 4300–4307.

W. Yang et al., 2011. Cell-Temperature Determination in InGaP–(In)GaAs–Ge Triple-Junction Solar Cells. *IEEE Electron Device Letters,* 32(10), pp. 1412 - 1414.

W. Zhao et al., 2016. Fullerene-Free Polymer Solar Cells with over 11% Efficiency and Excellent Thermal Stability. *Advanced Materials,* 28(23).

Weiwei Z. et al, 2018. Comprehensive control of voltage loss enables 11.7% efficient solid-state dye-sensitized solar cells. *Energy & Environemtal Science,* Issue 7, pp. 1643-1912.

wikipedia, u.d. *Solar energy.* [Online]
Available at: https://en.wikipedia.org/wiki/Solar_energy#cite_ref-5
[Använd 2020].

X. Jiang et al., 2020. Miscibility-Controlled Phase Separation in Double-Cable Conjugated Polymers for Single-Component Organic Solar Cells with Efficiencies over 8 %. *Angewandte Chemie,* 59(48), pp. 21683-21692.

X. Mao et al., 2020. Enhanced performance of all solid-state quantum dot-sensitized solar cells via synchronous deposition of PbS and CdS quantum dots. *New Journal of Chemistry,* 44(2), pp. 505-512.

X. Zheng et al., 2019. Recombination and bandgap engineering in CdSeTe/CdTe solar cells. *APL Materials,* 7(7), p. 071112.

Y. B. Pottathara, 2019. Chapter 1 - Synthesis and Processing of Emerging Two-Dimensional Nanomaterials. i: Elsevier, red. *Nanomaterials Synthesis: Design, Fabrication and Applications.* u.o.:u.n., pp. 1-25.

Y. Cui et al., 2019. Over 16% efficiency organic photovoltaic cells enabled by a chlorinated acceptor with increased open-circuit voltages. *Nature Communications ,* Volym 10.

Y. Fu et al., 2015. Solution Growth of Single Crystal Methylammonium Lead Halide Perovskite Nanostructures for Optoelectronic and Photovoltaic Applications. *Journal of the American Chemical Society,* 137(17), p. 5810–5818.

Y. Hao et al., 2016. Novel Blue Organic Dye for Dye-Sensitized Solar Cells Achieving High Efficiency in Cobalt-Based Electrolytes and by Co-Sensitization. *ACS Applied Materials & Interfaces,* 8(48).

Y. Hao et al., December 2016. A small electron donor in cobalt complex electrolyte significantly improves efficiency in dye-sensitized solar cells. *Nature Communications,* 13934 (2016)(7).

Y. J. Jang et al., 2019. Long-Term Stable Solid-State Dye-Sensitized Solar. *Crystals,* 9(9), p. 452.

Y. Ren et al., 2018. A Stable Blue Photosensitizer for Color Palette of Dye-Sensitized Solar Cells Reaching 12.6% Efficiency. *Journal of the American Chemical Society,* 140(7), p. 2405–2408.

Y. Wang, T. W. Hamann, Oct 2018. Improved performance induced by in situ ligand exchange reactions of copper bipyridyl redox couples in dye-sensitized solar cells. *Chemical communications,* Issue 54, pp. 12361-12364.

Yiming C. et al., 2018. Direct Contact of Selective Charge Extraction Layers Enables High-Efficiency Molecular Photovoltaics. *Joule,* 2(6), pp. 1108-1117.

Yun, J., 2017. Ultrathin Metal films for Transparent Electrodes of Flexible Optoelectronic Devices. *Advanced Functional Materials,* 27(18).

Z. Song et al., 2015. Impact of Processing Temperature and Composition on the Formation of Methylammonium Lead Iodide Perovskites. *Chemistry of Materials,* 27(13), p. 4612–4619.

Z. Tian et al., 2020. Honeycomb spherical 1T-MoS2 as efficient counter electrodes for quantum dot sensitized solar cells. *Materials Research Bulletin,* Volym 396.

Zeman, M., 2006. Advanced Amorphous Silicon Solar Cell Technologies. i: V. A. Jef Poortmans, red. *Thin Film Solar Cells: Fabrication, Characterization and Applications.* u.o.:John Wiley & Sons.

Zhenhua Sun et al., 2015. Reduced Carrier Recombination in PbS - CuInS2 Quantum Dot Solar Cells. *Scientific Reports,* Issue 5.

Zhenxiao Pan et al., 2019. Boosting the Performance of Environmentally Friendly Quantum Dot-Sensitized Solar Cells over 13% Efficiency by Dual Sensitizers with Cascade Energy Structure. *Advanced Materials,* 31(49).